Synthesis and characterization of zinc oxide nanowires and silver nanoparticles for perovskite solar cells application

January, 2016

MD. MIJANUR RAHMAN

Graduate School of Advanced Integration Science

CHIBA UNIVERSITY

（千葉大学審査学位論文）

Synthesis and characterization of zinc oxide nanowires and silver nanoparticles for perovskite solar cells application

January, 2016

MD. MIJANUR RAHMAN

Graduate School of Advanced Integration Science

CHIBA UNIVERSITY

DISSERTATION APPROVED AS TO THE STYLE AND CONTENT BY

I certify that I have read this dissertation and that, in my opinion,
it is fully adequate in scope and quality as a dissertation
for the degree of Doctor of Philosophy.

Associate Professor. Dr. Hideaki SHIROTA
(Chairman of Supervisory Committee)
Department of Nanomaterial Science
Graduate School of Advanced Integration Science
Chiba University, Japan

I certify that I have read this dissertation and that, in my opinion,
it is fully adequate in scope and quality as a dissertation
for the degree of Doctor of Philosophy.

Associate Professor. Dr. Takehisa KONISHI
(Supervisor)
Department of Nanomaterial Science
Graduate School of Advanced Integration Science
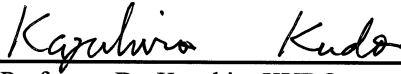Chiba University, Japan

I certify that I have read this dissertation and that, in my opinion,
it is fully adequate in scope and quality as a dissertation
for the degree of Doctor of Philosophy.

Associate Professor. Dr. Yasuo IZUMI
(Member of Supervisory Committee)
Department of Chemistry
Graduate School of Science
Chiba University, Japan

Approved by the Chiba University Committee of Graduate School of Advanced Integration Science.

DISSERTATION APPROVED AS TO THE STYLE AND CONTENT BY

I certify that I have read this dissertation and that, in my opinion,
it is fully adequate in scope and quality as a dissertation
for the degree of Doctor of Philosophy.

Professor. Dr. Kazuhiro KUDO
(Coo-supervisor and Member of Supervisory Committee)
Department of Electronics and Electrical Engineering
Graduate School of Engineering
Chiba University, Japan

I certify that I have read this dissertation and that, in my opinion,
it is fully adequate in scope and quality as a dissertation
for the degree of Doctor of Philosophy.

Professor. Dr. Peter Krüger
(Member of Supervisory Committee)
Department of Nanomaterial Science
Graduate School of Advanced Integration Science
Chiba University, Japan

Approved by the Chiba University Committee of Graduate School of Advanced Integration Science.

CERTIFICATE OF AUTHORSHIP / ORIGINALITY

I certify that the work in this dissertation has not previously been submitted for a degree nor has it been submitted as part of requirements for a degree or diploma or other qualification at this or any other university except as fully acknowledged within the text.

I also certify that the dissertation has been written by me. Any help that I have received in my research work and the preparation of the dissertation itself has been acknowledged. Any published (or unpublished) ideas and/or techniques from the work of others are fully acknowledged in accordance with the standard referencing practices.

Signature of Candidate

Md. Mijanur Rahman

Department of Nanomaterial Science

Graduate School of Advanced Integration Science

Chiba University, Japan

January, 2016.

DEDICATION

I would like to dedicate this Doctoral dissertation to the memory of Japanese people who have all passed away into the great void or whatever places you choose to believe by earthquake and tsunami disaster in March 11, 2011. They taught me perseverance and prepared me to face challenges with humility, strength and faith. They were a constant source of inspiration to my life. I want to say that without financial support provided through their taxes, I could not have completed this process. I am sure they would have been proud.

ABSTRACT

Zinc oxide (ZnO) nanostructures (NSs) were fabricated on fluorine-doped tin oxide (FTO) glass substrate through the reactive evaporation method which is very simple, easily controllable, non-catalytic, cost effective, rapid and relatively low temperature growth. Under the optimized growth conditions, the fabricated ZnO nanowires (NWs) exhibit high crystallinity and they also show preferential growth orientation along the *c*-axis that is crucial for solar cell application. As an electron transporting layer, the high crystalline NWs has been utilized to prepare the organic-inorganic perovskite solar cells. Synthesis of methylammonium iodide (CH_3NH_3I), methylammonium lead triiodide ($CH_3NH_3PbI_3$) layers and spin-coating of poly(3-hexylthiophene-2,5-diyl) (P3HT) were carried out under ambient condition because of low-cost and easy processing technique in which dry atmosphere was unnecessary for perovskite formation. Since the morphology of the $CH_3NH_3PbI_3$ film is one of the most important factors to influence the efficiency of the solar cells, many approaches have been evolved for its improvement. This study demonstrated that the filtration of lead iodide (PbI_2)-solution has a major effect on morphology of $CH_3NH_3PbI_3$ perovskite film. Filtration approach is, therefore, of crucial importance for uniform growth as well as higher surface coverage of the $CH_3NH_3PbI_3$ film, in order to obtain a higher PCE of perovskite solar cells. The perovskite solar cell fabricated by using filtrated PbI_2-solution showed a PCE of 4.8% which is significantly better than the device based on non-filtrated PbI_2-solution. Further boosting the PCE of the devices, plasmonic NPs have been integrated to the ZnO NWs based perovskite solar cells. The effect of Ag NPs on PCE was demonstrated and it was found that the PCE improved from 4.8% - 5.4% by adding Ag NPs on ZnO NWs.

ACKNOWLEDGEMENTS

Table of Contents

LIST OF TABLES

LIST OF FIGURES

List of Abbreviations and Symbols

1D	:	One dimensional
3D	:	Three dimensional
A	:	Absorption
Ag	:	Silver
Al	:	Aluminum
Au	:	Gold
Ca	:	Calcium
C_{abs}	:	Absorption cross section
$CaTiO_3$	:	Calcium titanate
C_B	:	Conduction Band
Ce	:	Cerium
$CH_3NH_3PbBr_3$	:	Methylammonium lead tri-bromide
$CH_3NH_3PbI_3$	:	Methylammonium lead tri-iodide
Cl	:	Chlorine
Cscat	:	Scattering cross section
Cu	:	Cupper
CVD	:	Chemical vapor deposition
DLE	:	Deep level emission
DSC	:	Dye-sensitized solar cells
E_{CB}	:	Conduction band energy
eV	:	Electronvolt, Energy
E_{VB}	:	Valence band energy
FE	:	Free exciton

FE-SEM	:	Field-emission scanning electron microscope
FF	:	Fill Factor
FTO	:	Fluorine-doped tin dioxide
Ga	:	Germanium
GaN	:	Gallium nitride
H_2O	:	Water
hcp	:	Hexagonal close packed
HMTA	:	Hexamethylenetetramine
HOMO	:	Highest occupied molecular orbital
HTMs	:	Hole transporting materials
I	:	Iodine
IPCE	:	incident-photon-to-electron conversion efficiency
IQE	:	Internal Quantum Efficiency
I_{SC}	:	Short-Circuit Current
ITO	:	Indium tin oxide
J_{SC}	:	Short-Circuit Current density
$J\text{-}V$	:	Current-Voltage Characteristics
K	:	Potassium
KOH	:	Potassium hydroxide
LD	:	hole diffusion length
LED	:	Light emitting diode
LUMO	:	lowest unoccupied molecular orbital
MBE	:	Molecular beam epitaxy
MOCVD	:	Metal-organic chemical vapor deposition
MOVPE	:	Metal-organic vapor phase epitaxy

Na	:	Sodium
NaCl	:	Sodium chloride
NaOH	:	Sodium hydroxide
NH_3	:	Ammonia
NIR	:	Near Infrared
NPs	:	Nanoparticles
NSs	:	Nanostructures
NWs	:	Nanowires
OLED	:	Organic light emitting diode
P3HT	:	poly(3-hexylthiophene)
Pb	:	Lead
PbI_2	:	Lead iodide
PCE	:	Power conversion efficiency
PL	:	Photoluminescence
PLD	:	Pulsed laser deposition
Pt	:	Platinum
Q_{abs}	:	Abssorption efficency
Q_{scat}	:	Scattering efficiency
R_p		Parallel resistance
R_s	:	Series resistance
R_{sh}	:	Shant resistance
RT	:	Room temperature
SEAD	:	Selected area electron diffraction
Si	:	Silicon

Spiro-MeOTAD	:	2,2′,7,7′-tetrakis-(N,N-di-p-methoxyphenyl-amine)-9,9′-spirobifluorene, Hole Transporter
Sr	:	Strontium
TCO	:	Transparent Conducting Oxide
TEM	:	transmission electron microscopy
TiO_2	:	Titanium (II) Dioxide
UV	:	Ultra-violet
VB	:	Valence Band
VLS	:	Vapor liquid solid
V_{OC}	:	Open-Circuit Voltage
VS	:	Vapor solid
XRD	:	X-ray diffraction
YAG	:	Yttrium Aluminium Garnet
$Zn(NO_3)_2$	:	Zinc nitrate
$Zn(OH)_2$	:	Zinc hydroxide
$Zn_4CO_3(OH)_6 \cdot H_2O$	:	Zinc carbonate hydroxide hydrate
ZnO	:	Zinc oxide
ZnO NSs	:	Zinc oxide nanostructures
ZnO NWs	:	Zinc oxide nanowires

CHAPTER ONE

Introduction

The perception of nanotechnology was made known firstly by the Nobel Prize Winner Richard Feynman in his speech "There's plenty of room at the bottom" at Caltech on December 29, 1959.[1] Though Feynman never decidedly quoted "nanotechnology", he expressed a method and proposed that it will be attainable to exactly manipulate the single atom and molecule. About 20 years later, Feynman's forecast that came real with the creation of the scanning tunneling microscope (STM) and high resolution transmission microscope (HRTEM), which accelerate the finding of fullerenes and carbon nanotubes (CNT) in 1985 and 1991, respectively.[2,3] In addition, the growth and properties of nanostructure materials along with the quantum dots and nanowires (NWs) are extensively studied, and diverse accomplishments in nanoscience and nanotechnology have been made. In this chapter, an introduction and short background of the dissertation with respect to the zinc oxide (ZnO) nanostructures (NSs) and perovskites solar cells have been presented. The motivation and objectives of this dissertation have been summarized based on the synthesis of ZnO NWs and silver (Ag) nanoparticles (NPs) and their application to the perovskites solar cells. The whole pictures of this dissertation have been reported by using a section of thesis overview.

1.1 THESIS MOTIVATION

ZnO NWs have attracted considerable attention over the past few years for wide application in optical and electrical devices because of high transparency, wide-bandgap semiconductivity, high-surface to volume ratio, high carrier mobility and so on. The electron mobility of ZnO NWs is substantially higher than titanium dioxide (TiO_2), which makes it an ideal choice for faster electron transporting layer in solar cells. The aforementioned unique properties of ZnO NWs depend strongly on their morphology, dimension, structure and crystallinity of NWs.[4] Therefore, controlled synthesis of ZnO

NWs on a large scale under mild conditions is one of the most important issues nowadays. Motivated by this, the ZnO NSs were fabricated on fluorine-doped tin oxide (FTO) glass substrates by using reactive evaporation method which is very simple, easily controllable, non-catalytic, cost effective, rapid and relatively low temperature growth. Under the optimized growth conditions, ZnO NWs exhibit high crystallinity and smooth crystal planes as well as they also show preferential growth orientation along the *c*-axis that is crucial for solar cell application.[5-10]

The fabricated NWs were employed to prepare the perovskite solar cells. Solution-processed organic-inorganic perovskite solar cells are of tremendous interest due to their low-cost and huge potential for high efficiency. Although, ZnO NPs have been used to prepare the perovskite solar cells, the NPs exhibit slow electron transport because of grain boundaries resulting in a higher charge recombination at ZnO/perovskite interface which limit the efficiency of solar cells.[5,11-13] The high crystalline ZnO NWs with a high-quality surface plane would be favorable for charge transport because it provide long diffusion path, less collision with the boundaries, and high charge-collection efficiency.[11] Synthesis of methylammonium iodide (CH_3NH_3I), methylammonium lead triiodide ($CH_3NH_3PbI_3$) and spin-coating of poly(3-hexylthiophene-2,5-diyl) (P3HT) were carried out under ambient air conditions because of low-cost and easy processing technique in which the dry atmosphere was unnecessary for perovskite formation. Since the morphology of the $CH_3NH_3PbI_3$ film including surface coverage, roughness and thickness is one of the most important factors to influence the power conversion efficiency (PCE) of the solar cell, many other approaches have been emerged for its improvement. In this dissertation, I have demonstrated that the filtration of lead iodide (PbI_2)-solution has a major effect on morphology of $CH_3NH_3PbI_3$ perovskite film. Filtration approach is, therefore, of crucial important for uniform growth as well as higher surface coverage of $CH_3NH_3PbI_3$ film, in

order to obtain a higher PCE of perovskite solar cells. The perovskite solar cell fabricated by using filtered PbI_2-solution showed a PCE of 4.8% which is significantly better than the device based on non-filtered PbI_2-solution.

Further boosting the PCE of the solar cells, the implementation of plasmonic technologies may improve the efficiency of light harvesting, the short circuit current density (J_{sc}), and thus the solar cell performance. Therefore, the enhancement of light absorption should be a promising, because the absorption of perovskite solar cell drop-down around the band edge.[14] Motivated by the desire to enhance the light absorption of perovskite layer, I investigate the use of localized surface plasmon resonance (LSPR) of Ag NPs. Ag NPs were successfully prepared by using vacuum vapor evaporation method, and subsequent thermal annealing. It was observed that the particles morphology was intensely changed depending on both of the evaporated Ag film-thickness and annealing time, on which optical absorptions are strongly dependent. The effect of Ag NPs on PCE was demonstrated and it was found that the PCE significantly improved from 4.8% -5.4% by adding Ag NPs on ZnO NWs. However, optical measurements suggested that the increased PCE is not mainly due to the enhancement in optical absorption but other mechanisms, *e.g.* reduced exciton binding energy are responsible as reported recently.[15]

1.2 THESIS OBJECTIVES

The main objective of the dissertation is to synthesize, characterize and optimize the ZnO NWs, $CH_3NH_3PbI_3$ perovskite and metallic Ag NPs for organic-inorganic perovskite solar cell applications.

The primary objective of this study is to find out the effects of reaction conditions on morphology of as-synthesized ZnO NWs. A parametric investigation of the effect of substrate temperature, growth time on the morphology of ZnO NWs has been conducted.

The aim of this section of research is to decide the optimum reaction conditions for ZnO NWs synthesized *via* the reactive evaporation (RE) method. In addition, metal-seeded growth of ZnO NWs has also been investigated for comparison. The use of metal-seed can lead to higher size and better alignment of the ZnO NWs on the FTO substrates because of epitaxial relationship. Various characterization techniques, such as field-emission scanning electron microscopy (FE-SEM), transmission electron microscopy (TEM), energy dispersive X-ray (EDX) analysis and X-ray diffraction (XRD) have been employed for characterization of morphology and structure of the ZnO NWs.

A secondary objective is to demonstrate whether the organic-inorganic perovskite solar cells using ZnO NWs fabricated under ambient air condition can obtain PCE comparable to those prepared under moisture controlled conditions. In particular, an investigation of filtration effect of PbI_2-solution on surface morphology of the perovskite layer has been conducted. The solar cells were prepared using both of the filtered and non-filtered PbI_2-solution, and a significant photovoltaic effect was realized.

The third part of this study describes the integration of plasmonic NPs in the organic-inorganic perovskite solar cells with the aim of further improving the PCE. Particularly, due to enhancement of light harvesting and the short circuit current density (J_{sc}), the Ag NPs were incorporated in to the solar cell. The effect of Ag NPs on PCE was demonstrated and it was found that the PCE improved significantly by adding Ag NPs on ZnO NWs.

1.3 THESIS OVERVIEW

The dissertation is arranged in to five chapters. The general introduction starts with the diverse achievements in nanoscience and nanotechnology, short background of ZnO NSs, potential application of ZnO NWs to the perovskite solar cells and their further developments of performances through using Ag NPs are presented in chapter 1. Thesis

motivations, objectives and structures referred as thesis overview are summarized in this chapter.

Chapter 2 will provide an extensive literature review that will serve as a guide for understanding the subsequent chapters. This detailed review will be based on the basic properties, characteristics and fabrication methods of ZnO NSs, organic-inorganic hybrid perovskites and Ag NPs. A brief introduction on fundamentals of plasmonic effect and its application in the solar cell are provided. In addition, the general aspects of photovoltaic are studied in this review section.

Chapter 3 describes the fabrication of ZnO NSs through the main experimental technique used in this study as a reactive evaporation method. The morphological evolutions of ZnO NSs, in the case of without any catalyst and with Ag seeded layer have been investigated based on various reaction conditions. Characterizations and measurements of ZnO NSs along with some major characterization techniques have been discussed. From the experimental part, conclusions are given separately in this chapter.

Chapter 4 presents the detail experimental process of synthesis, characterizations of $CH_3NH_3PbI_3$ perovskites and their application to the ZnO NWs based perovskites solar cells. The filtration and non-filtration effects of PbI_2 solution on perovskite solar cell performances were demonstrated. The effects of atmosphere, humidity and UV irradiation on device stability are summarized. Finally, this chapter will conclude the major findings from the experimental part.

Chapter 5 contains the synthesis, characterizations of Ag NPs and their application to the ZnO NWs based perovskites solar cells. The effect of Ag NPs on PCE of ZnO NWs based organic-inorganic perovskites solar cell was demonstrated in this chapter.

Lastly, chapter 6 will then conclude the major findings of the whole work and possible future prospects.

References

[1]   E. Drexler, *There's Plenty of Room at the Bottom.*

[2]   H. W. Kroto, J. R. Heath, S. C. O'Brien, R. F. Curl and R. E. Smalley, Nature **318**, 162-163 (1985).

[3]   S. Iijima, Nature **354**, 56-58 (1991).

[4]   Y. Xia, P. Yang, Y. Sun, Y. Wu, B. Mayers, B. Gates, Y. Yin, F. Kim and H. Yan, Adv. Mater. **15**, 353 (2003).

[5]   M. Law, L. E. Greene and J. C. Johnson, Nat. Mater. **4**, 455 (2005).

[6]   L. Li, T. Zhai, Y. Bando and D. Golberg, Nano Energy **1**, 91 (2012).

[7]   A. I. Hochbaum and P. Yang, Chem. Rev. **110**, 527 (2010).

[8]   K. Mahmood, B. S. Swain and A. Amassian, Nanoscale **6**, 14674-14678 (2014).

[9]   J. Dong, Y. Zhao, J. Shi, H. Wei, J. Xiao, X. Xu, J. Luo, J. Xu, D. Li, Y. Luo and Q. Meng, Chem. Commun. **50**, 13381-13384 (2014).

[10] F. J. Ramos, M. C. Lopez-Santos, E. Guillen, M. K. Nazeeruddin, M. Gratzel, A. R. Gonzalez-Elipe and S. Ahmad, ChemPhysChem **15**, 1148-1153 (2014).

[11] M. Hosni, Y. Kusumawati, S. Farhat, N. Jouini and T. Pauporté, J. Phys. Chem. C **118**, 16791-16798 (2014).

[12] H. S. Kim, S. H. Im and N. G. Park, J. Phys. Chem. C **118**, 5615-5625 (2014).

[13] H. S. Kim, J. W. Lee, N. Yantara, P. P. Boix, S. A. Kulkarni, S. Mhaisalkar, M. Grätzel and N. G. Park, Nano Lett. **13**, 2412-2417 (2013).

[14] Z. Lu, X. Pan, Y. Ma, Y. Li, L. Zheng, D. Zhang, Q. Xu, Z. Chen, S. Wang, B. Qu, F. Liu, Y. Huang, L. Xiao and Q. Gong, RSC Adv. **5**, 11175-11179 (2015).

[15] W. Zhang, M. Saliba, S. D. Stranks, Y. Sun, X. Shi, U. Wiesner and H. J. Snaith, Nano Lett. **13**, 4505-4510 (2013).

CHAPTER TWO

Literature Review

ZnO can be considered as an 'old' semiconductor. ZnO is easy to prepare as NSs among all materials. They exhibit many interesting properties, such as optical, electrical, mechanical, and thermal and so on. The NSs could have huge potentials for various practical applications in optoelectronics, sensors, solar cells, and biomedical science because it is bio-safe. ZnO can be made highly conductive by doping. In this chapter, I aim to present an extensive literature review based on the basic properties, characteristics, and fabrication methods of ZnO NSs, $CH_3NH_3PbI_3$ perovskite structures and plasmonic Ag NPs. Moreover, the basics of photovoltaics, and the factors that limit the efficiency of perovskite solar cells are studied.

2.1 BASIC OF ZINC OXIDE

ZnO is believed as a result of oxidization of metallic zinc. Harley and Wehlte claimed the Zn was invented by Henkel in 1421.[1] After a long time the ZnO was recognized and the research on ZnO started gradually in the 1930s. ZnO occurs in nature in the form of a mineral named zincite. The natural color of ZnO was white which was found in zincite mineral. It has been used for a long time in enamel coatings, as a catalyst and photocatalyst for a series of chemical reactions as well as a pigment for paints.[2,3] However, the pure ZnO is colorless and transparent to the visible light due to its large band gap. ZnO can be considered as a ceramic, and as a semiconductor.[4,5] Both in the acid and base, ZnO can be fully dissolved, that means that it is amphoteric. Besides, ZnO is incapable to dissolve in the water and alcohol.[6] Probably, ZnO has the affluent family of NSs among all the materials with respect to structures and properties.[7] Moreover, ZnO is easy to prepare as NSs. Diversity in morphologies of the ZnO is one of its most attractive features for different practical applications.

2.2 PROPERTIES OF ZINC OXIDE

ZnO is an inorganic compound and a very special material. Depending on end-use, ZnO is considered as a bulk chemical or specialized semiconductor. The widely known concept is that the ZnO is a natural *n*-type semiconductor because of native defects, such as oxygen vacancies or Zn interstitial.[3,8,9] Although, the explanation of the real mechanism of *n*-type ZnO is still under debate, the effect of non-stoichiometry of oxygen,[10] might be one of the important reasons that depends on temperature and pressure. For examples, oxygen is degenerating out of the lattice at high temperature, and the ZnO color changes from white to yellow. Again, the color turns back to the white during cooling down because of oxidization of ZnO. Hence, the color change is a result of loosing of oxygen to form the non-stoichiometric ZnO. [11]

ZnO in its normal form almost exhibits *n*-type conductivity with the electrons in its valence band as charge carriers. This conductivity is thought to be due to the surplus stoichiometric of Zn ions, which occupy interstitial locations in the crystal lattice. By doping with other elements to replace either the zinc or the oxygen, the conductivity can be varied over a wide range. ZnO can be intrinsically doped *via* oxygen vacancies and/or zinc interstitials.[12,13] Extrinsically, ZnO can be doped both, *n* and *p*-type. For *n*-type doping, the materials in group III and VII for instance aluminum (Al), germanium (Ga), chlorine (Cl), and iodine (I) can be used.[14] In contrary, the materials in group I and V, for example Cu, Ag, and Au can be used for *p*-type doping. Meanwhile, various efforts are currently being directed for successful made of *p*-type ZnO which have appeared in the literature.[15-17] However, the reliability and reproducibility of *p*-type doping of ZnO are still questionable. Even with controlled doping, none of them are long-lasting. This may be due to low solubility of the *p*-type dopants and their compensations by large number of *n*-type impurities.

ZnO is a direct wide band gap material which has been demonstrated experimentally, and it has a band gap of 3.3 eV, which corresponds to the UV region emission that makes it promising for applications in the opto-electronics and many other fields of nano devices. It is very inexpensive compare to other wide band gap materials. The ease of fabrication, structural variety and broad range of its potential applications has made ZnO, one of the appealing research topics of the semiconductor fields recently. Many crucial properties of ZnO NSs, containing crystal structures, optical, electrical, mechanical, and thermal properties are reviewed in details in the sections below, and some basic physical parameters of the ZnO properties are summarized in the tabular form as shown in table 2.1.

Table 2.1: Some basic properties of wurtzite ZnO.

Property	Value	Reference
Lattice Parameters	$a = b = 3.25$ Å, $c = 5.21$ Å	[18-20]
Stable crystal structure	Wurtzite	[18-20]
Density	5.606 g/cm^3	[20, 21]
Melting point	1975 ^{o}C	[19, 20, 22]
Thermal conductivity	0.6, 1-1.2	[20]
Relative dielectric constant	8.66	[20]
Refractive index	2.008	[18, 20]
Exciton binding energy/ Energy gap	60 meV/ 3.3 eV	[19, 20, 22]
Effective mass (Electron/Hole)	0.24 m$_o$ / 0.59 m$_o$	[20]
Electron mobility	100-200 cm^2 V^{-1}s^{-1}	[21, 20]
Hole mobility	5-50 cm^2 V^{-1}s^{-1}	[20, 23]
Bulk Young modulus	111.2±4.7 GPa	[19]

2.2.1 Crystal structures of zinc oxide

Based on the conditions of thermodynamics, the ZnO crystal structure can be categorized into three forms such as hexagonal wurtzite, cubic zinc-blende, and the rarely observed cubic rocksalt, as schematically shown in Fig. 2.1. At relatively high pressures about 10 GPa, the rocksalt (NaCl) structure of ZnO may be obtained. Zinc blende structure can be stabilized by fabricating ZnO on the substrate with proper cubic lattice.[19] However, the wurtzite structure of ZnO is thermodynamically stable at ambient conditions and therefore, it is commonly observed in the semiconductor research. In hexagonal wurtzite structure, one Zn ion is encircled tetrahedrally by the four O ions and contrariwise. The tetrahedral coordination geometry of this compound is typical of sp^3 covalent bonding nature. However, the bonds also have a very strong ionic character and they are regarded as at the border of ionic and covalent compound.

Rocksalt   **Zinc-blende**   **Wurtzite**

(a)   (b)   (c)
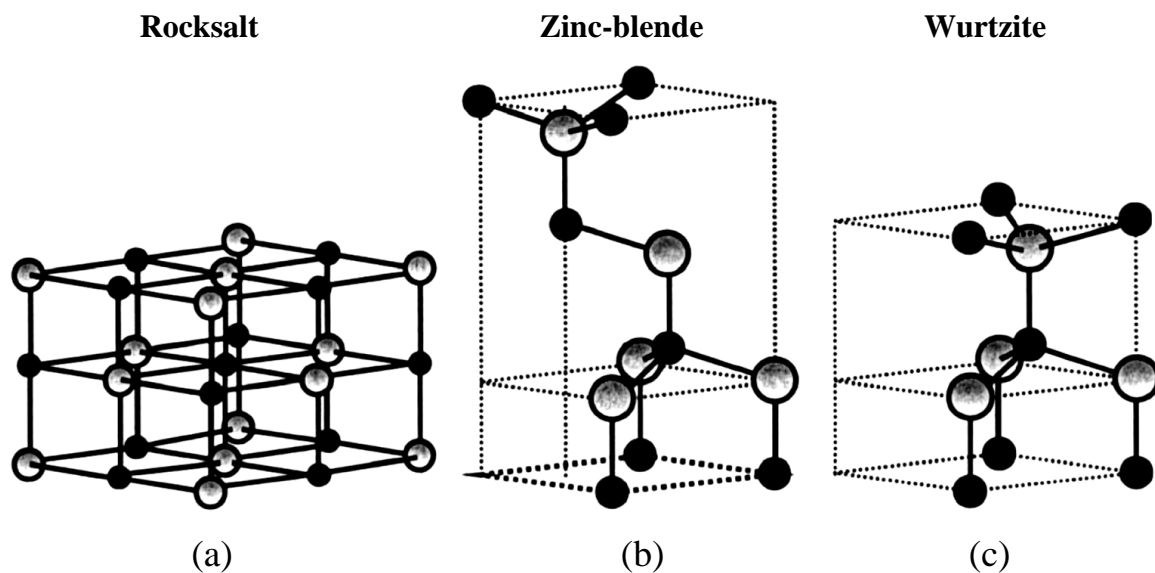
Figure 2.1: Crystal structures of ZnO: (a) cubic rocksalt, (b) cubic zinc-blende, and (c) hexagonal wurtzite. The Zn and O atoms are denoted by the shaded gray and black spheres, respectively. Reprint with permission from ref.[19] Copyright 2015, American Institute of Physics.

The wurtzite structure of ZnO has a hexagonally-close-packed unit cell with two lattice parameters, *a* and *c*. The ratio of the lattice parameters *c/a* is $(8/3)^{1/2} = 1.633$.[24] A schematic illustration of wurtzite structure of ZnO is shown in Fig. 2.2. The wurtzite structure is comprised of two interdependent hexagonally-close-packed sub-lattices, each of which composed of one kind of atom distributed one another on the threefold *c*-axis through an amount of $u = 3/8 = 0.375$ in fractional coordinate. The internal parameter, *u* is determined as the bonding length, *b* parallel to the *c*-axis (anion-cation bond length) divided by the *c* lattice parameter.
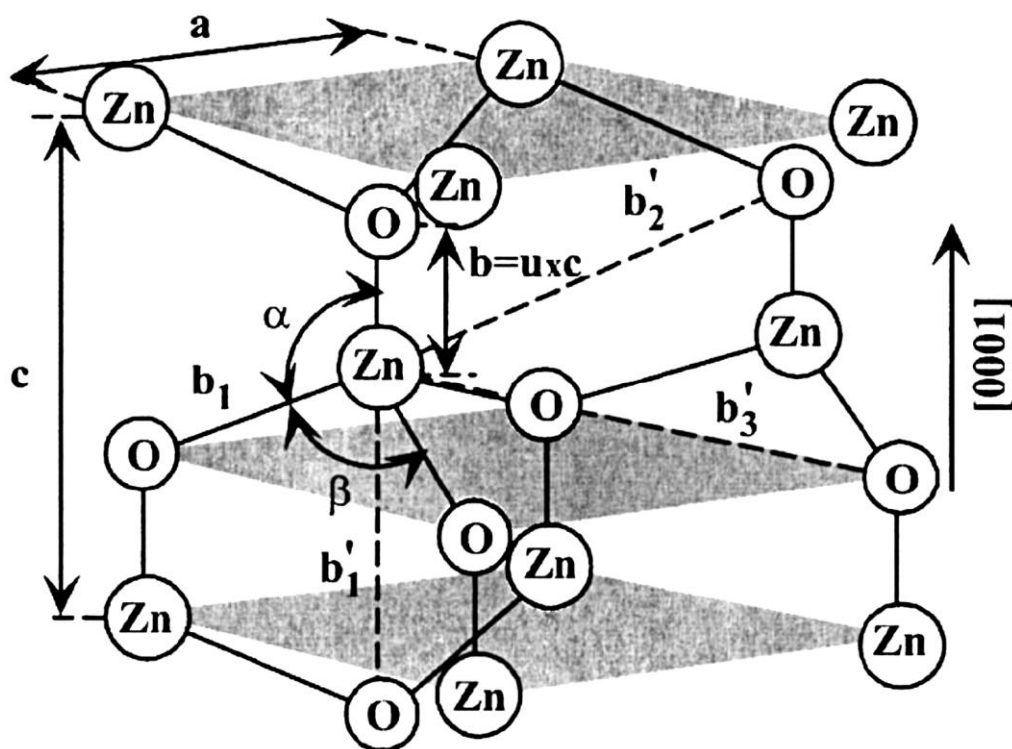
Figure 2.2: Schematic illustration of wurtzite structure of ZnO representing the lattice constants *a* and *c* in the basal plane and basal direction, respectively. The parameter, *u* determined as the bonding length, *b* divided by the *c*: *α* and *β* are the bonding angles (109.47° in case of ideal crystal). Reprint with permission from ref.[19] Copyright 2015, American Institute of Physics.

ZnO has two different polar surfaces along the *c*-axis: the positive charged Zn-(001) polar surface and negative charged O-(00ī) polar surface are the strongest polarity surfaces. The polar plane (001) and associated direction [001] are the most generally used surface and direction for growth of wurtzite ZnO. In addition, the polar surfaces help to bring the result of the variety of ZnO NSs by surface reconstruction to maintain a stable structure. Some other crucial properties of ZnO, for instance defect generation, spontaneous polarization, and piezoelectricity strongly depend also on its polarity.

2.2.2 Optical properties

The optical properties of wide band-gap semiconductor are dictated by their effects of intrinsic and extrinsic. The intrinsic optical-transitions occur within the free electrons and holes, in the conduction band and in the valence band, respectively, and this includes excitonic effect because of Coulomb interaction. There are commonly two types of excitonic effects such as free exciton, and bound exciton. The free exciton can also show excited states as well as their ground-state transition, in case of low-impurity concentrations or high quality samples. Besides, the extrinsic properties are associated with impurities/ dopants and or point defects which lead to create the electronic-states into the bandgap. Thus, the optical absorption as well as the emission process can be tuned.

ZnO is one of the most important semiconductor materials which have several optical properties investigated through various experimental techniques, for instance optical transmission, reflection and absorption, photo reflection, spectroscopic ellipsometry, photoluminescence (PL) and so on. At room temperature (RT) measurement, the PL spectra of ZnO typically consist of UV emission and broad emission band as shown in Fig. 2.3. The UV emission band is dominated by the free exciton (FE) emission. The UV emission band is related to a near band-edge transition of ZnO, namely, the recombination

of the free excitons. Besides, the broad emission band between 420 and 700 nm observed nearly in all samples because of deep level emission band (DLE). The DLE band has been attributed to several defects in the crystal structure,[12] such as O-vacancy (V_O), Zn-vacancy (V_{Zn}), O-interstitial (O_i), Zn-interstitial (Zn_i), and extrinsic impurities.[12,13] Umar *et al.*[25] reported that the crystal quality of the ZnO is an important factor in the appearance of a strong and sharp UV emission in the PL spectra.
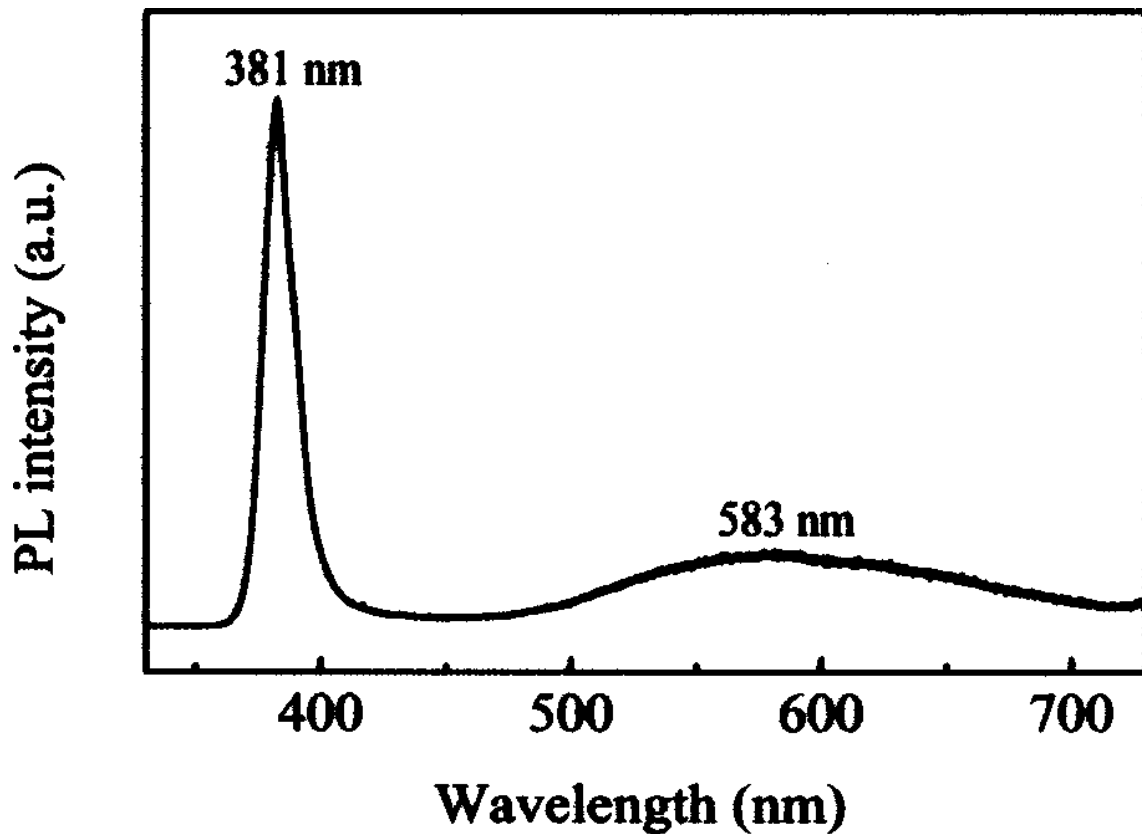
Figure 2.3: Room-temperature PL spectrum of the as-grown ZnO whiskers. Reprint with permission from ref. [26] Copyright 2015, American Institute of Physics.

ZnO is a direct and wide bandgap semiconductor which has a band gap, E_g of 3.37 eV (*i.e.* in the near-UV) at RT,[19] and 3.44 eV at low temperatures,[27] that makes it promising material for photonic applications in the UV or blue spectral range. For controlled applications, band gap engineering is technologically very important. The bandgap of ZnO can be tuned *via* divalent substitution on the cation site. Cd substitution

on the cation site leads to a reduction in the bandgap to ~ 3.0 eV.[28] By contrast, substituting Mg on the Zn site can increase the bandgap to approximately 4.0 eV,[29,30] similar to the effects of Al and In in GaN. In some respects, the semiconducting properties of ZnO compare favorably to those of the GaN. The ZnO has a high exciton binding-energy of 60 mV,[31] but on the other hand the binding-energy of GaN is around 25 meV,[32] which is much lower than that of ZnO. The high exciton binding-energy of ZnO can provide the efficient exciton emission under RT, at minimal excitation energy. In addition, a significant enhancement of the exciton binding energy of ZnO can be achieved by quantum size confinement.[33] Consequently, ZnO is treated as an auspicious material with great potential for a variety of practical applications, such as piezoelectric transducers, optical waveguides, surface acoustic wave devices, varistors, transparent conductive oxides, chemical and gas sensors, UV-light emitters and so forth.

2.2.3 Electrical properties

The studies of the electrical characteristics of ZnO NSs are crucial important for applications and developments of future nano devices. ZnO is *n*-type semiconductor, which means electrons are the main carrier charges. In order to keep the charge balance, one oxygen vacancy or zinc interstitial is always accompanied by two electrons.

$$O_o^x \leftrightarrow \frac{1}{2}O_2(g) + V_o^{\bullet\bullet} + 2e' \quad \text{and} \quad Zn_o^x \leftrightarrow Zn_i^{\bullet\bullet} + 2e' \qquad (2.1)$$
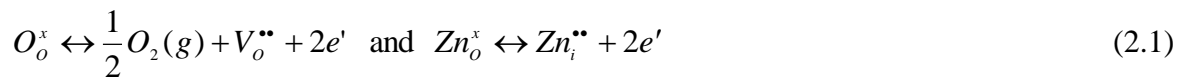
The levels of oxygen vacancies and zinc interstitials will depend on the different synthesis methods, which results in a variation of conductivity of ZnO NSs. Electrical properties can be modulated from the insulator through semiconductor to metal by adjusting doping levels, while controlling the high optical transparency.[19] The single crystalline ZnO NSs show the superior electrical property compared to polycrystalline thin-film. For instance,

the electron mobility of ZnO thin-film transistors is about 7 cm^2 V^{-1}s^{-1},[34] but on the other hand it is around 80 cm^2 V^{-1}s^{-1} for single crystalline ZnO NWs that is over ten times higher than that of ZnO polycrystalline thin-film transistors.[35] Furthermore, the electron mobility around 1000 cm^2 V^{-1}s^{-1} was observed after employing the polyimide coating on ZnO NWs due to minimize the electron trapping and scattering at the surface.[36] Electron mobility also differs from temperatures and at 80 K, a maximum electron mobility of ZnO has been reported around 2000 cm^2 V^{-1}s^{-1}.[37] By contrast, the data on hole mobility are rare and the reported values are in the range of 5 - 50 cm^2 V^{-1}s^{-1}.[20,23,38]

2.2.4 Mechanical properties

Mechanical properties of the materials comprised of several conditions for examples as stiffness, hardness, piezoelectric constants, Young's modulus, bulk modulus, and yield strength.[19] It is useful to classify crystal lattice defects because the lattice defect often leads to the mechanical failure. Materials are often stronger when they have defects. Relatively, ZnO is a soft material and its hardness is approximately 4.5 Mohs.[39] In order to elucidate the mechanical properties of ZnO NWs, the direct measurements have attracted lots of attention because the traditional measurement methods are quite challenging to apply in NSs. Bai *et al.*[40] developed a direct measurement approach based on electric-field-induced resonant excitation by using in situ TEM. From the classical elasticity theory, the fundamental resonance frequency of ZnO NWs can be calculated as

$v = \dfrac{\beta_i^2 T}{4\pi L^2} \sqrt{\dfrac{E}{3\rho}}$, where β_i is a constant for the *i* th harmonic, $\beta_1 = 1.875$ and $\beta_2 = 4.694$. *E* is the

bending modulus for the vibration along the longitudinal direction. The length of NW, *L* and ρ is mass density. The calculated bending modulus of the ZnO NW is ~52 GPa. By using Brillouin light scattering techniques, the measured elastic constants of ZnO at C11,

C12, C33, C13, and C44 are 206, 118, 211, 118, and 44 GPa, respectively.[41] However, elastic constants of ZnO are smaller than the III-V semiconductors, for instance GaN. ZnO is beneficial for ceramics due to its low thermal expansion, high heat conductivity, high heat capacity as well as high melting temperature.[42] Furthermore, it has been reported that the ZnO has the highest piezoelectric tensor within the tetrahedrally bonded semiconductors as well as compared to GaN and AlN.[43] These unique characteristics enables the ZnO a crucial important material for piezo-electrical applications.

2.3 FABRICATION METHODS OF ZINC OXIDE NANOSTRUCTURES

ZnO is an exclusive material that is, seemingly the affluent groups of NSs in the midst of all the material considering both the crystal structures and properties. Its dimension includes highly organized nanowire arrays, nanorod, nanobelt, nanoring and so forth. These structures can be fabricated by using several distinct methods, for examples chemical vapor deposition (CVD),[44, 45] physical vapor deposition (PVD),[46-51] wet chemical methods,[52-55] electrochemical deposition,[56-59] metal-organic chemical vapor deposition (MOCVD),[60,61] molecular beam epitaxy (MBE),[62] sputtering,[63,64] pulsed laser deposition,[65,66] templated growth,[67] and even top-down approach by etching,[68] and so forth.

These techniques are well establish and controllable for growth of ZnO NSs,[69] however, some of the above-quoted techniques have several detriment associated with their synthesize process, for example, the need to control a high vacuum level, handling the high growth temperatures, the synthesized NWs consist of defects and contaminations, the use of pernicious gases as well as the system involved in making samples are complicated and the experimental costs of these methods are sometimes very high. Some of the growth methods of ZnO NSs are discussed in details in the sections below.

2.3.1 Wet chemical Method

The wet chemical method is a common name of a group of methods used to fabricate the various NSs of materials, commonly in the liquid phase, such as sol-gel process, hydrothermal synthesis, spray drying, aerosol spray pyrolysis, Electrochemical deposition, cryochemical synthesis and so forth. Among these processes, the hydrothermal synthesis is widely used process of ZnO NSs growth because of low-temperature process, simplicity, reproducibility, cost-effectiveness and large-scale production.[52,54,55,70,71] The wet chemical method is widely used also in ceramics manufacturing.

For hydrothermal synthesis, an alkaline solution is necessary due to ZnO NSs growth because the divalent metal ions do not hydrolyze normally in the acidic environment.[72,73] In this case, the potassium hydroxide (KOH) and sodium hydroxide (NaOH) are commonly used as alkali compounds. KOH has a larger ion (K^+) radius compare with the NaOH and therefore, have a lower probability of incorporation into the ZnO lattice.[73] In the case of NaOH solution, Na^+ is attracted by the OH^- around the nanocrystal that leads to form a virtual capping layer, resulting in a hinder in nanocrystal growth.[74] The main chemical reactions involved in the growth of ZnO are illustrated by:[75]

$$Zn^{2+} + 2OH^- \leftrightarrow Zn(OH)^2 \tag{2.2}$$

$$Zn(OH)_2 + 2OH^- \leftrightarrow [Zn(OH)_4]^{2-} \tag{2.3}$$

$$[Zn(OH)_4]^{2-} \leftrightarrow ZnO_2^{2-} + 2H_2O \tag{2.4}$$

$$ZnO_2^{2-} + H_2O \leftrightarrow ZnO + 2OH^- \tag{2.5}$$

$$ZnO + OH^- \leftrightarrow ZnOOH^- \tag{2.6}$$
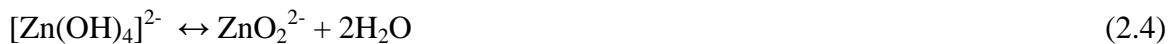
However, it is thought that the solubility of ZnO in an alkali solution increases with increasing concentration of alkali and temperature above its critical point.

Moreover, probably the most commonly used chemical agents in hydrothermal synthesis reported in the literatures are zinc nitrate $Zn(NO_3)_2$ and hexamethylenetetramine

(HMTA) ($C_6H_{12}N_4$).[76,77] $Zn(NO_3)_2$ provides the Zn^{2+} ions, while H_2O molecules in the solution contribute O^{2-} ions are obligatory for developing ZnO NWs. Although, the accurate functions of HMTA is not clear during ZnO NWs growth, it acts as coordinates and bridges the two Zn^{2+} ions.[78] Zhang *et al.*[79] reported that the HMTA acts as a weak base and pH buffer. The HMTA quickly hydrolyzes in water and gradually produces HCHO and NH_3 discharging the strain energy that is correlated with its molecular structures. These processes are very critical for ZnO synthesis as shown in the following equations.

$$HMTA + 6H_2O \leftrightarrow 4NH_3 + 6HCHO \tag{2.7}$$

$$NH_3 + H_2O \leftrightarrow NH_4^+ + OH^- \tag{2.8}$$

$$Zn^{2+} + 4NH_3 \leftrightarrow [Zn(NH_3)_4]^{2+} \tag{2.9}$$

$$Zn^{2+} + 2OH^- \leftrightarrow Zn(OH)_2 \tag{2.10}$$

$$Zn(OH)_2 \leftrightarrow ZnO + H_2O \tag{2.11}$$
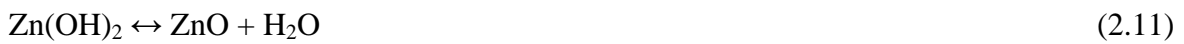
The decomposed NH_3 produces an essential environment that is crucial for the growth of $Zn(OH)_2$ as well as it coordinates with Zn^{2+} that results in a balanced aqueous Zn^{2+}. The rate of hydrolysis of HMTA decreases with increasing pH and vice versa.[80] Wang *et al.*[81] reported the aligned single crystalline ZnO NWs can be obtain *via* hydrothermal process by using zinc carbonate hydroxide hydrate ($Zn_4CO_3(OH)_6 \cdot H_2O$). Solutions containing acetate, formate or chloride formed the rods like structure, whereas the nitrate and perchlorate, and sulfate mainly produced wires and flat hexagonal platelets, respectively.

2.3.2 Vapor phase growth method

Vapor phase transport growth is one of the most widely used growth methods for obtaining high-quality metal-oxide thin films or NSs. There are several advantages of this method that the obtained NSs, for instance the NWs always possess a large aspect ratio, while the non-equilibrium growth method required the doping of some external elements within the single-crystalline NSs. The vapor phase growth methods can be categorized into the laser ablation, thermal evaporation and CVD based on the nature of precursors and heating sources.

2.3.2.1 Pulsed laser deposition

In order to growth of high quality film of material, the pulsed laser deposition (PLD) technique has been employed for several decades.[82] The PLD attracted much research interest after the growth of high temperature superconductor films. Typically, PLD is very simple and easy technique which uses high power laser pulses, apparently 10^8 Wcm^{-2} due to melting, evaporation and ionization of the material from the surface of a target as shown schematically in Fig. 2.4. The vaporized materials consists of electrons, neutrals and ions are called as laser-produced plasma-plume which spreads quickly elsewhere outside of the surface of the target with a typical velocity ~10^6 cms^{-1} in vacuum condition. The film growth takes place on the substrate whereat some plume material re-condenses. By using PLD method, several hundred nanometers thicknesses of various oxide-films can be grown under a reactive oxygen gas without requirement of further processing. During PLD, several experimental conditions can be changed, which have a strong effect on film properties. Thus, experimental conditions of this method permit the films properties to be tailored to suit the individual needs of user's applications. The main advantages of PLD experiment are the simplicity, versatility, flexibility, rapidity (10 - 15 min.) and cost-

effectiveness. However, the situation is not so simple because of huge variables influencing the properties of the films, for instance, background gas pressure in the chamber, substrate temperature and laser fluence. An extensive efforts and appreciable amount of time are essential due to optimize these variables. In addition, the fundamental processes are not clearly understood while the material transfers from the target to the substrate.
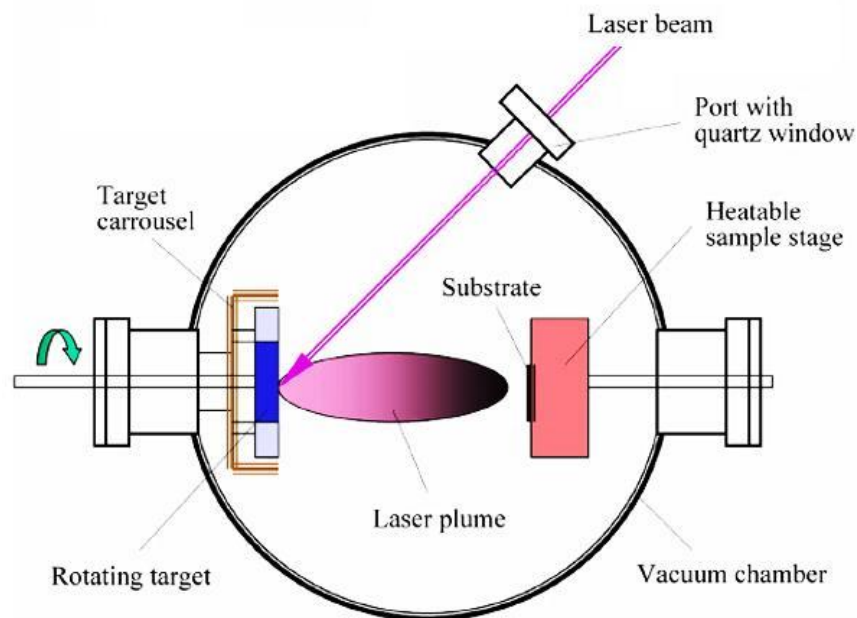
Figure 2.4: A schematic illustration of the experimental set-up for pulsed laser deposition. Adapted from ref.[83]

2.3.2.2 Chemical vapor deposition

CVD is a surface modification process whereby a solid material is coated from a vapor through the chemical reaction occurring both in the gasphase and on the surface of normally heated substrate. The solid material is achieved as a depositing, a single crystal, or as powder. By changing the experimental conditions, such as substrate temperature, total pressure gas flows, compositions of the reaction gas mixture, substrate material and so on, materials with various properties can be obtained. In a CVD process, typically the

heated substrate is exhibited into the volatile precursors (zinc vapor and oxygen, in the case ZnO NSs growth), where they react and condense on the top of substrate to obtain coveted deposition as shown in Fig. 2.5. The reactions can be boosted by heat (thermal CVD), plasma (plasma-enhanced CVD) or a higher frequency radiation, like UV (photo-assisted CVD) and so forth. There are some other widely used techniques: MOCVD that employs metal-organic precursors; Metal-organic vapor phase epitaxy (MOVPE) that also utilizes the metal-organic precursors and it yields single crystal (*i.e.* epitaxial) films on the single crystal substrates. Both in the technique of MOCVD and MOVPE, the gas-phase reactions play a significant aspect in the most deposition processes.
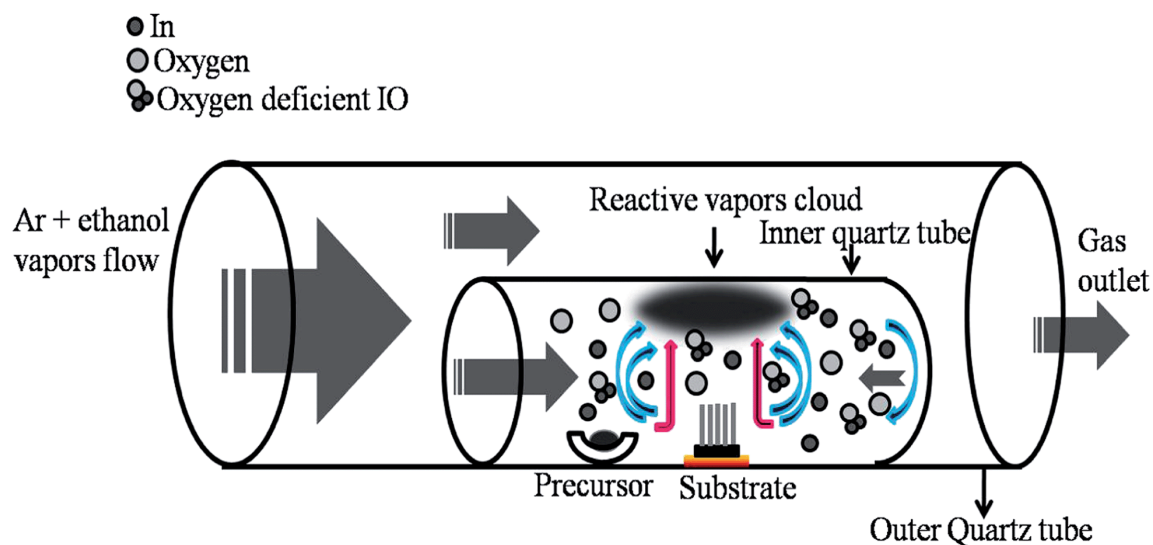
Figure 2.5: Schematic diagram of CVD system with double-tube configuration for growth of vertically aligned nanostructures. Reprint with permission from ref.[84] Copyright 2015, Royal Society of Chemistry.

CVD has a number of very strong advantages over the deposition of thin films and nanostructures. This deposition method is capable of processing solid deposition, large area, high-quality thin films at relatively high deposition rates and low vacuum condition when compare to physical vapor deposition.[85] In order to remove the impurities from gaseous precursors, distillation techniques have been employed in CVD. Recently, CVD

has been widely applied for NWs growth using catalyst in which the reactant and dopant are well defined gas sources.[84,86,87] Through this catalytic CVD method, the size, composition and doping level of NWs can be controlled precisely. In CVD method, the size of NWs is regulated by three common factors: the eutectic droplet size is controlled by the size of metal catalyst nanoclusters; the solubility of reactant in catalyst nanoclusters, subsequent size of eutectic droplets is managed by the growth temperature; and the diameter of the NWs can be affected through the vapor pressure. However, the high temperature (900-1000 °C) seriously limits the compatibility of this method, especially for applications in flexible electronics.[88,89]

2.4 GROWTH MECHANISM OF ZINC OXIDE NANOSTRUCTURES

In the CVD method, the growth mechanisms associating the ZnO NSs formation could be categorized into the vapor liquid solid (VLS) and vapor solid (VS) growth. Main dissimilarity between these mechanisms is whether a catalyst assists or directs the nucleation and growth. Note that all of the catalyst-assisted growth processes does not follow the VLS mechanism. The detailed growth mechanisms are discussed in the following section.

2.4.1 Vapor liquid solid mechanism

VLS mechanism was first introduced by Wagner *et al.*[90] who successfully applied this method in the late 1990s due to grow silicon whisker. Figure 2.6 shows a schematic diagram of the VLS mechanism. In a typical VLS mechanism, the metal NPs such as Au, Ag, Cu, Al, or their alloys are used as a catalyst mainly to initiate nucleation. During the growth process, firstly, the metal NPs are heated up above the eutectic temperature to form liquid eutectic alloy by adsorbing vapor components. With the presence of the source

material in its vapor phase, the eutectic alloy will continue to absorb the semiconductor materials over the vapor/liquid interface, resulting in a supersaturation. Further incorporation of source material within the eutectic alloy will lead to a nucleation event, whereby the source material tends to precipitate and forms a liquid/solid interface, which is so called growth interface. Therefore, growth of NWs is achieved through the transformation of semiconductor material from the vapor source at vapor/liquid interface into the eutectic, subsequent continuous solid inclusion at the liquid/solid interface. In this mechanism, the catalytic NPs lead the growth direction and usually halt at the growth front or top of the nanowires. The VLS mechanism is auspicious to obtain vertically aligned ZnO NWs with high aspect ratios.
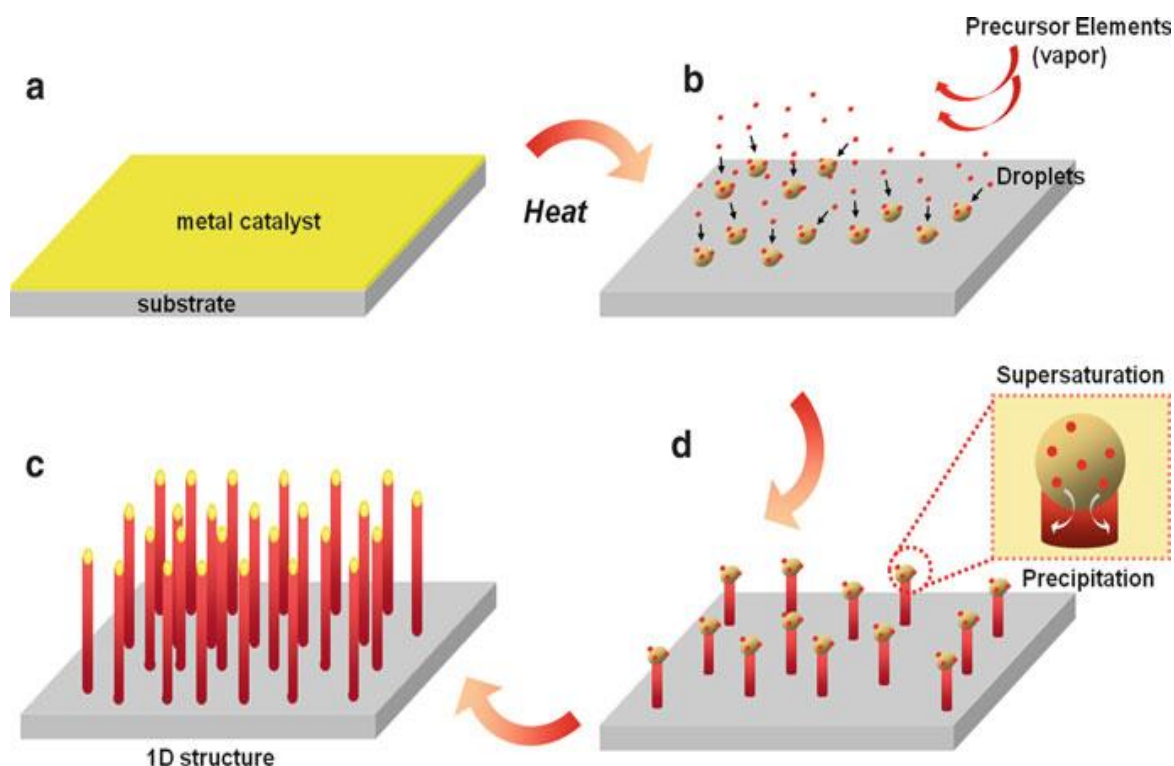
Figure 2.6: Schematic diagram of the growth of one dimensional nanostructure through VLS mechanism. Reprint with permission from ref.[91] Copyright 2015, Royal Society of Chemistry.

2.4.2 Vapor solid mechanism

VS mechanism leads to the growth of one-dimensional nanostructures. Under this mechanism, the Zn atoms condensate on a solid catalyst, such as Au at a lower temperature and the preferential deposition occurs at energetically favored nucleation sites. Zn atoms migrate due to surface diffusion and self-organized ZnO NWs form that are oriented preferentially along the *c*-axis direction. However, VS growth mode is deeply affected by the anisotropic characteristics between crystal orientations of nanostructured oxide particles, resulting in the facile growth of NSs. Consistently, the catalysts used for this growth mechanism were not only observed at the growth front of NWs, but also at roots of NWs after growth.[92] The presence of such particulate or the buried catalysts (*e.g.*, Au NPs) at the NWs root suggests a growth mechanism similar to VS mechanism. Kim *et al.*[93] demonstrated the *Vs* mechanism of NW growth using Au catalyst, as illustrated in Fig. 2.7.
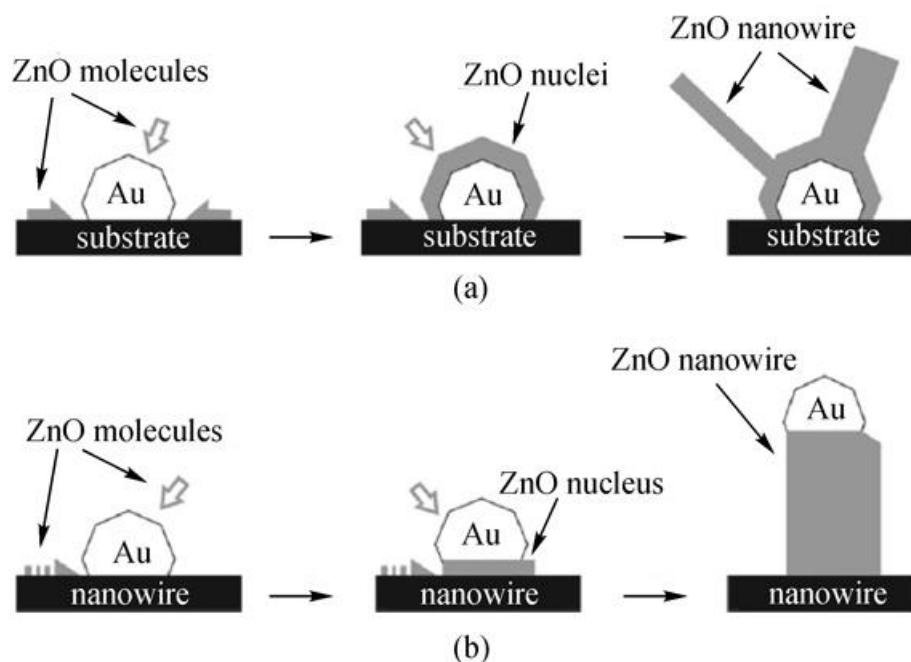
Figure 2.7: Schematic illustration of the basic steps of the growth mode of NWs with (a) Au NPs at the roots and (b) at the growth front of the NWs. Reprint with permission from ref.[93] Copyright 2015, John Wiley & Sons.

2.5 ORGANIC-INORGANIC PEROVSKITES-BASED SOLAR CELLS

2.5.1 Perovskites: crystal structures

Perovskites has come from the discovery of calcium titanate ($CaTiO_3$) by the Russian mineralogist, L. A. Perovski (1792-1856). Next, various perovskite materials with the similar crystal structure were discovered. The basic structure of perovskite is very simple. The ideal perovskite structure can be represented by the common formula of AMX_3, where A is a cation, M is the metal cation and X an oxide (O^{2-}) or a halide anion (Cl⁻, Br⁻, I⁻, etc.). In this arrangement, they form a MX_6 octahedral where M sits at the center of an octahedra surrounded by X occupied at the corners are shown in Fig. 2.8 (a). The MX_6 octahedra form an extended three-dimensional (3D) network through connecting all the corners as shown in Fig. 2.8 (b). Species A is assigned to a metal cation which fills the hole of the 3D structure formed by eight adjacent octahedra and balances the charge of the whole network. The large metal cations, A can be calcium (Ca), potassium (K), sodium (Na), strontium (Sr), lead (Pb), cerium (Ce) or various rare metals. For organic-inorganic perovskites, A is replaced by an organic cation, which is confined by the twelve closest X anions. The organic cations are of great interest in the perovskite family because of their unique structure, where the sheets of organic and inorganic components stack alternatively at a single molecular-scale. Usually, organic group consists of an alkyl-chain or aromatic group with a single-ring. The size of both organic cation and metal ion is a crucial parameter for adjusting optical and electronic properties of perovskite material. [94,95]

The ideal perovskites have cubic geometry but in fact, they are pseudo-cubic or distorted-cubic in nature because the lattices are not ever ideal.[94] Many physical, optical, electronic, magnetic and dielectric properties of perovskite materials strongly depend on the details of these distortions. Thus, the form of perovskite is supposed by a tolerance

factor (t) which is associated with the radii of A, M and X:[96] $t = \dfrac{R_M + R_X}{\sqrt{2}(R_A + R_X)}$ where R_A,

R_M and R_X are the radii of A, M and X, respectively. Until now, Goldschmidt's tolerance

factor, t has been commonly accepted as a parameter for the investigation of ionic radii

relationship that finally enables to predict the formation or stability of cubic perovskite

structure.[97] Thus, the stability and the distortion of the perovskites structure are dependent

strongly on tolerance factor and $t = 1$ is considered for ideal perovskite with a cubic

geometry.
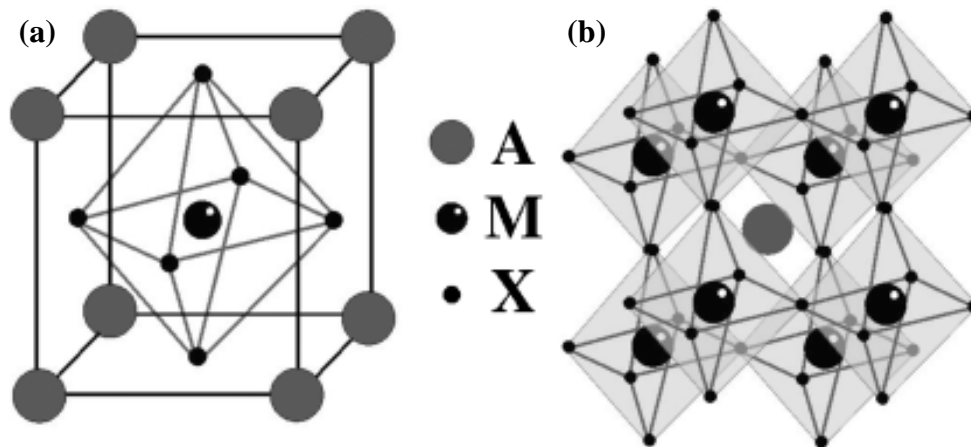
Figure 2.8: (a) A cubic structure of a conventional perovskite and (b) their extended

network structure connected by the corner-shared octahedra. Reprint with permission from

ref.[98] Copyright 2015, John Wiley & Sons.

2.5.2 Perovskites: properties

Organic-inorganic hybrid perovskites are interesting for excellent optical properties,

especially due to their tunable direct bandgap (E_g) and it can be modulate either by

changing the alkyl group, the metal cation or the halide anion.[99,100] It has been observed

that the AMX_3 band gap increases with increasing the size of A and varying B from tin

(Sn) to Pb. However, the band gap decreases with changing X from Cl to Br to I. Kim *et*

al.[101] reported a value of Eg = 1.5 eV for $CH_3NH_3PbI_3$ perovskite which was deposited on

titanium dioxide (TiO_2) film. The position of valence band energy (E_{VB}) was estimated to -5.43 eV below vacuum level. From the observed optical band gap, the position of conduction band energy (E_{CB}) was determined to -3.93 eV. Furthermore, $CH_3NH_3PbI_3$ perovskite exhibits a wide absorption spectrum that covers visible light up to a wavelength of 800 nm as well as a large optical absorption coefficient ($\alpha \sim 10^4 - 10^5$ cm^{-1}) comparable with CdTe, InP, GaAs, Cu (In,Ga)Se$_2$ (CIGS).[102-105]

The conductivity of the tin-based perovskites reveals high values,[106] and it could be tuned from *p*-type to *n*-type through the appropriate control of synthesis conditions. Charge transport properties in organic-inorganic halide perovskites are of another crucial parameter to determine the photovoltaic efficiencies. Stoumpos *et al.*[107] report the mobilities of perovskites based on various leads and tin, and the charge transport of these materials was determined through the Seebeck coefficient and Hall-effect measurements. They estimated the electron mobilities of 2320 cm^2 V^{-1}s^{-1} and 66 cm^2 V^{-1}s^{-1} for $CH_3NH_3SnI_3$ and $CH_3NH_3PbI_3$, respectively. These values are remarkably higher compare to Si (1400 cm^2 V^{-1}s^{-1}). High mobility along with high charge-carrier lifetimes is very important because the electrons and holes can move enough distances to extract the current without losing their energy as heat within the device.

2.5.3 Perovskites for solar cells application

2.5.3.1 Evolution of perovskite solar cells

The conversion of solar energy into electricity is achieved through the solar cells devices using solar thermal systems based on the photovoltaic effect. In 1839, French physicist Alexandre Edmond Becquerel, first observed the photovoltaic effect called the "Becquerel effect", when he impinged the light on the AgCl electrode in an electrolyte solution.[108] The photovoltaic effect in selenium (Se) was also discovered by Willoughby Smith in

1873. Three years later in 1877, William G. Adams and Day discovered the photovoltaic effect through the observation of illuminating a junction between Se and platinum produced electricity without heat or moving parts, when the light was exposed to selenium.[109]

Based on the above two discoveries, the first Se solar cell was fabricated in 1877. After five years later in 1883, Charles Fritts was fabricated the first Se wafers-based solar cell devices which showed PCE of approximately 1%.[110] In 1918, a Polish scientist, Jan Czochralski was discovered a method for growth of single crystals of metal,[111] and the latter single-crystal silicon (Si) was grown by applying this method. In 1941, the first single-crystal Si solar cell was demonstrated. In 1954, Chapin, Fuller and Pearson at Bell Laboratories enhanced the efficiency of a Si solar cell to 6%.[112] In 1976, Tsubomura *et al*.[113] present the first dye-sensitized solar cells (DSC) in which porous ZnO has been used as photoanode and the PCE of the cell was about 2.5%. The organic thin-film solar cell with a PCE of about 1% was first reported by Tang in 1986.[114] In the field of solar cell, the organic materials had been great interest within the scientific and industrial communities due to some advantages, such as low fabrication cost, diverse synthetic methods, flexible processing ability and sustainability. In parallel, the evolution of DSC has progressed significantly with a PCE of around 7.0% in the year 1991, by introducing the nanoporous TiO_2 electrodes.[115] In the year 2005, the reported PCE of the DSC was over 11%.[116] In 2009, Miyasaka and co-workers who first used $CH_3NH_3PbI_3$ and methylammonium lead tri-bromide ($CH_3NH_3PbBr_3$) perovskites as sensitizers in liquid electrolyte-based DSC, which resulted in PCE of 3.81% and 3.13%, respectively.[117] Recently, perovskite solar cells have received extreme attention as an auspicious material capable of fabricating high performance solar cells at a low cost.

2.5.3.2 Role of perovskite in solar cells

The role of perovskite became a general question after the research work presented by Snaith and co-workers.[118] They observed that the V_{OC} achieved with the insulating Al_2O_3-based device was 1.2 V, higher than with a TiO_2-based device. The devices had low energy losses associated with the electron injection in the mesoporous oxide demonstrated by a higher value of V_{OC}. Due to the large diffusions length of perovskites the use of mesoporous Al_2O_3 as an inert scaffold can transport electron to the photoanode. Meanwhile, several groups of researchers conducted experiments and suggested that the organic-inorganic halide perovskites are able to perform transporting the electrons and holes simultaneously and efficiently.[119,120] Thus, it became quite clear that the perovskite materials reveal the ambipolar characteristics.

The charge diffusion lengths were demonstrated for $CH_3NH_3PbI_3$ and $CH_3NH_3PbI_{3-x}Cl_x$ by using femtosecond transient absorption and picosecond time-resolved fluorescent quenching measurement. An effective charge transporting length for $CH_3NH_3PbI_3$ was ~100 nm for both electrons and holes. The length is beyond 1 μm for the mixed perovskites,[121] and the lifetimes for both electron and hole are longer than the pure iodide. Based on this study, the light absorption can be enhanced with increasing the thickness of device, while reducing the effect of charge transport in the solar cell. Further studies on both of the electron and hole diffusion length (L_D) revealed that the L_D of electrons is shorter than the L_D of holes (~1 μm), while it shows similar value about 1 μm for both hole and electron in case of $CH_3NH_3PbI_{3-x}Cl_x$ device. This could be relevant for explaining the provision of mesoporous electron selective contact for most $CH_3NH_3PbI_3$ based solar cells. This charge behavior of perovskites would be crucial factor to design the efficient solar cell structure.

2.6 PLASMONIC ENHANCED SOLAR CELLS

2.6.1 Plasmonic effects: fundamental aspects

Plasmonic effects are observed in both bulk as well as metal NPs, especially in gold (Au), Ag, copper (Cu), etc. The plasmonic effect is the interaction between the free electrons in thin-metal surface or in metal NPs and incident light. Typically, the plasmonic effects can be categorized into two types: one is the surface plasmon resonance (SPR) effect and the other is LSPR effect. For NPs smaller than the wavelengths of incident light, the free electrons can shift everywhere the NPs. Consider spherical shaped NPs: the free electrons can move everywhere along the sphere surface in any manner. Therefore, they are able to couple to any impending electromagnetic (EM) field and move together with the components of its polarization of electric field projected on the sphere. In modern nanophotonics, the application of plasmonic effects of metal NPs has emerged as an efficient tool to enhance optical absorption, light trapping in the engineering of advanced devices.

2.6.1.1 Localized surface plasmon resonance

The noble metals NPs have distinct optical and EM properties rather than those of bulk materials due to their surfaces and quantum size effects. LSPR is an optical phenomena obtained by light when it interacts with metal NPs smaller than the incident wavelength.[122, 123] The phenomenon is a consequence of interactions between the incident light and surface electrons in the metal conduction band. This interaction forms coherent oscillations with a resonant frequency that greatly depends on the size, geometry, composition, dielectric environment and the separation distance between metal NPs. LSPR differs from the SPR because the generated plasmons oscillate locally to the NP instead of the metal-dielectric interface as shown in Fig. 2.9.
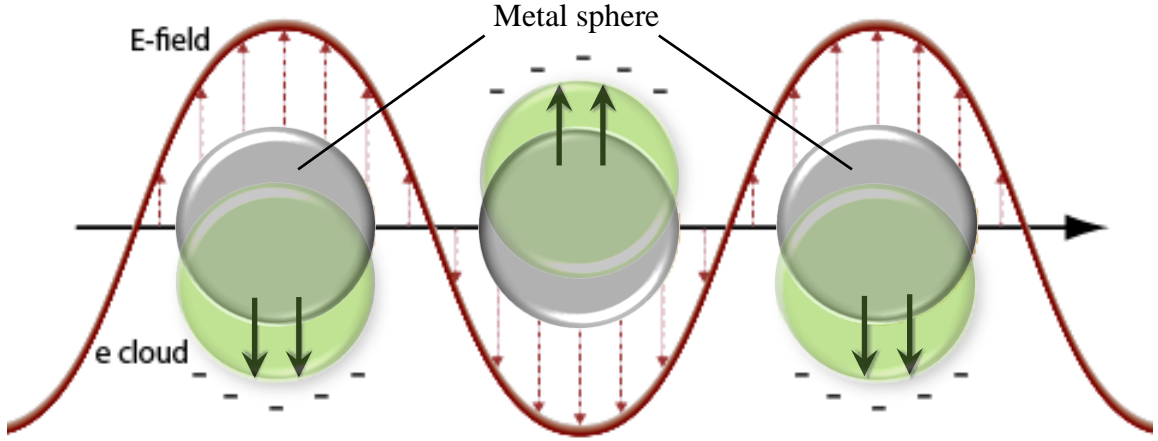
Figure 2.9: Schematic of localized surface plasmon resonance due to collective oscillation of surface electrons with incident light at a specific wavelength.

Over a century ago, Gustav Mie first elegantly described the interaction between light and small metal NPs. He solved Maxwell's equations analytically and obtained an expression for metal NPs surrounded by a dielectric medium interacting with an EM field. For spherical metal NPs smaller than the wavelength of light ($2r<<\lambda$), the extinction cross-section, σ_{ext} can be defined by the following formula:[123,124]

$$\sigma_{ext}(\lambda) = \frac{24\pi^2 r^3 \varepsilon_d^{3/2} N}{\lambda \ln(10)} \frac{\varepsilon_i(\lambda)}{(\varepsilon_r(\lambda) + 2\varepsilon_d)^2 + \varepsilon_i(\lambda)^2} \qquad (2.11),$$

where r is the radius of the NP, N is the electron density, λ the wavelength of absorbing radiations, ε_d the dielectric constant of the surrounding medium, and ε_r and ε_i are the real and imaginary part of complex dielectric function of bulk metal, respectively. The real part expresses the polarizability while the imaginary part describes the energy dissipation in the metal. Thus, equation (2.11) demonstrates the dependence of extinction, $\sigma_{ext,}$ on the dimension, shape, density and local environment of the NP. The interaction of NPs with light allows some photons to be absorbed and some to be scattered. The sum of the scattering and absorption can be determined as the extinction of the NPs. For NPs smaller than wavelength of light, the photon absorption and scattering cross section are given by:

$$C_{abs} = \frac{2\pi}{\lambda} \text{Im}[\alpha] \text{ and } C_{scat} = \frac{1}{6\pi} \left(\frac{2\pi}{\lambda} \right)^4 |\alpha|^2 \qquad (2.12),$$

where α is the polarizability provided by $\alpha = 3V (\varepsilon_m - 1) / (\varepsilon_m + 2)$ for a small NP, V the

volume of NP and ε_m the permittivity of metal. The efficiency of scattering, Q_{scat} is given

by $Q_{scat} = C_{scat} / (C_{scat} + C_{abs})$. Accordingly, absorption and scattering depend strongly on

the size of NP. The absorption enhancement occurs because of small NPs which size is

smaller than wavelength of light and therefore, the extinction is influenced by absorption.

In contrast, when the NPs size increases, the extinction is governed by scattering.

2.6.2 LSPR dependence on nanoparticles

So far, the LSPR sensing measurements have been employed Au or Ag NPs. The chemical

stability and oxidization resistance are the main advantages of Au. However, Ag has more

favorable optical properties: a stronger plasmon resonance which appears commonly at a

shorter wavelength than that of Au NPs. This feature can potentially offer a broader range

of tuning the frequency of plasmon resonance for Ag rather than Au.[125] In addition, Au

has higher loss in the intensity of absorption compare to Ag because of large reflectivity

from the metal surface. Several other metals have been also employed, for instance,

palladium (Pd), platinum (Pt), aluminum (Al), Sn, and Cu.

The size and shape of metal NPs contribute to spectral sequences because of changes

in surface polarization. The NPs with different shapes such as spheres, cubes, triangles,

octahedrons, and nanorods have been fabricated to tune the LSPR absorption ranges from

visible to infrared regions. An increase in sharpness or edges of metal NPs appears in red

shift of extinction spectra, because of their higher charge separation, which in turn can lead

to enhance the intensity of LSPR.[126] The non-spherical NPs tend to display numerous

redshifted peaks compared with the spherical NPs, as shown in Fig. 2.10.
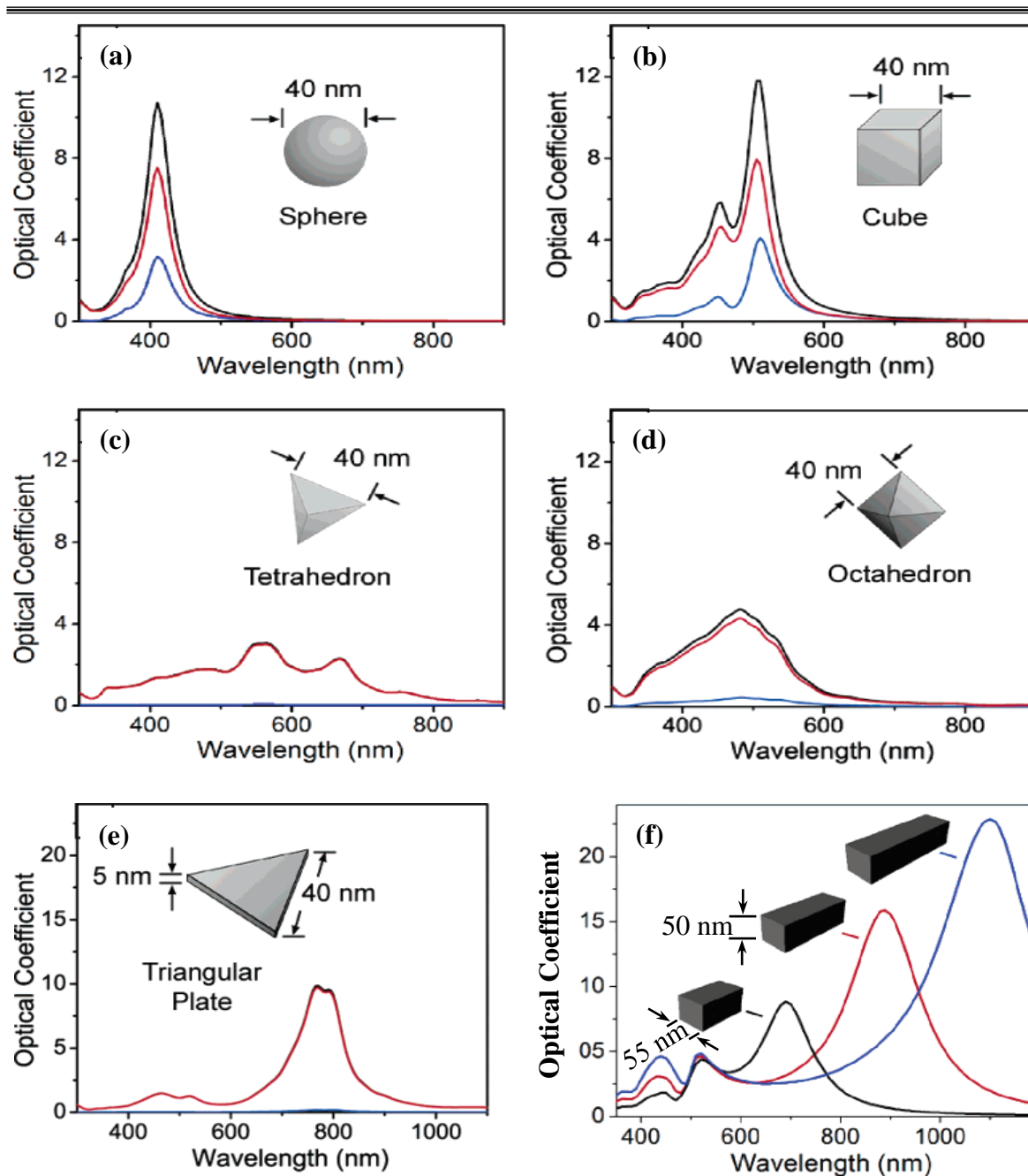
Figure 2.10: Extinction (black), absorption (red), and scattering (blue) spectra calculated for Ag NPs of different shapes: (a) a sphere exhibiting a single resonance peak, (b) a cube, (c) a tetrahedron, (d) an octahedron, (e) a triangular plate, and (f) rectangular bars with length of 100 nm (black), 150 nm (red), and 200 nm (blue). Note that the non-spherical NPs typically exhibit multiple, red-shifted resonance peaks. Reprint and modified with permission from ref.[127,128] Copyright 2015 American Chemical Society.

Another important aspect to consider is the size of the NPs, because it dominates the relative magnitudes of both absorption and scattering cross-section. For example, when the size of the NPs is smaller than 20 nm, the absorption becomes the predominant process. An increase in diameter or effective size of NPs increases the scattering cross-section, results in broader spectra. This relationship is generally indicated as a ratio of scattering to absorption. The redshifts associated with LSPR of NPs are dominated greatly by the spherical geometry rather than by an increase in size. For example in case of spherical NP, changing the size from 10 to 100 nm results in a red shift of 47 nm. On the contrary, in case of an elliptical NP, the change in aspect ratio from 2.5 to 3.5 results in shifts of the longitudinal band by 92 nm.[129] The separation distance between NP has also a great effect on response of the LSPR and it is expressed by the length of EM field decay. In practice, it was observed that the enhancement prolongs to about 10 nm from the NP surface and the intensity of SERS drops by a factor of 10, at a distance from ~ 2.8 nm.[130] Therefore, the EM field enhancement is a long-range event and extends above a monolayer regime. Thus, LSPR in noble metal NPs cause the optical absorption and scattering enhancement that is tunable through the visible and near-infrared.

2.6.3 Plasmonic-absorption enhancement mechanisms

Mechanisms to enhance absorption in solar cells are versatile. The interaction of NPs with light allows some photons to be absorbed and some to be scattered. The subwavelength metal nanostructures or NPs can be employed for scattering the incident light into broad distributions of angles, resulting in an enhancement of optical path length within the absorbing layer. In order to enhance the optical absorption, therefore, light trapping through multiple scattering is commonly achieved in solar cells by employing the metal NPs as shown in Fig. 2.11(a). This can lead to the higher short circuit current density (J_{SC})

in the solar cells.[131,132] The second mechanism involved in the absorption enhancement is related to the strong near-field intensities generated by the LSPR effect of NPs as shown in Fig. 2.11(b). Depending on size, shape, and composition of metal NPs, the excitation generates at a resonance frequency which can results in greatly enhanced field nearby NPs. As the optical absorption is commensurate with the intensity of local field, the strong local field which in turn can lead to enhance absorption. The third mechanism for enhancing absorption uses the scattering center *via* excited propagating waveguide modes inside the absorbing layer as shown schematically in Fig. 2.11(c). Since the modes propagate, partially, the energy in the waveguide mode would be absorbed inside the semiconductor layers, thereby exciting interband electron hole pairs as well as the absorption enhancement trough redirecting the light horizontally.
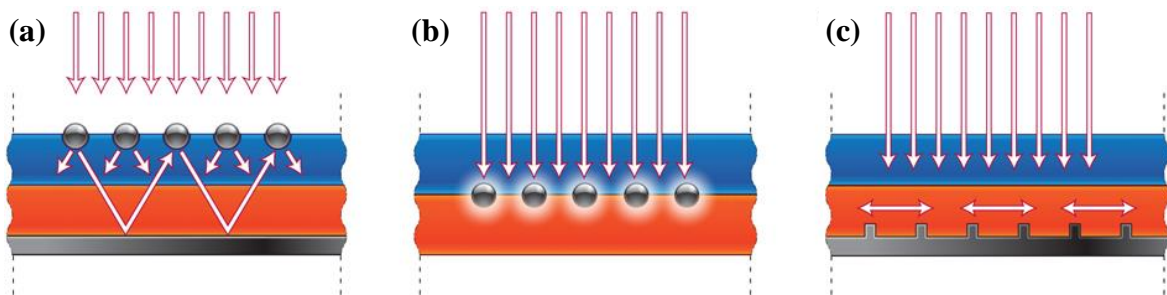
Figure 2.11: Plasmonic light-trapping by the metal NPs, causing an increase in optical absorption due to (a) light scattering, (b) strong near-field intensities through the excitation of LSP and, (c) coupling of guided modes from nanopatterned metallic back contacts. Reprint with permission from ref.[133] Copyright 2015, Nature Publishing Group.

2.6.4 Plasmonic nanoparticles in solar cells application

Metal NPs such as Au, Cu, or Ag can strongly interact with light due to their ability to support the excitations of localized surface plasmons (LSPs). The surface plasmon excitations result in intense localization of light in near-field, and absorption and/or scattering in the far-field. These unique characteristics, in particular the manipulation and

enhancement of light interaction with NPs could lead to their potential applications in various fields, such as Surface-Enhanced Fluorescence (SEF),[134,135] Surface-Enhanced Raman Scattering (SERS),[136,137] plasmonic solar cells,[138-140] nanomedicine,[141] and sensing.[142] In this section, the plasmonic NPs in solar cell applications that are recently attracting much attention will be discussed.

Plasmonic enhanced solar cell is one of the most interesting fields in nanophotonics nowadays. Plasmonic metallic NPs combined with the solar cells can concentrate and manipulate the light at the nanoscale, which in turn can lead to a reduction of the photoanode thickness required, as well as enhancing the absorption of the incident light.[133,143] It has been reported more recently, that the plasmonic NSs can intensify photo-absorption of the photocurrent generated in the solar cell in several distinct physical situations. There have been a number of interesting reports on GaAs solar cells,[132] dye-sensitized solar cells,[138] quantum well structures,[144] organic bulk heterojunctions cells,[145] ultrathin-film organic cells,[146] and perovskite solar cells.[139]

Figure 2.12 illustrates the circumstance of photocurrent enhancement in plasmonic solar cells. In their experiment, Pillai *et al.*[131] found that the LSPR of metal NPs scatter light in the visible and near-infrared region leading to the generation of guided modes, which enhance the intensity of light trapped in the silicon film. The enhancement of near-field and incident light scattering into active layer and/or wave guiding could be partially attributed to some electrical effects, including increased charge carrier transport in the active layer, or improved charge collection at the electrodes results in an enhancement of PCE of the solar cells. Kawawaki *et al.*[140] have reported the photocurrents of solar cells can be increased by using Ag nanocube structures because of plasmonic enhancement of light absorption and possible benefaction of exciton dissociation.
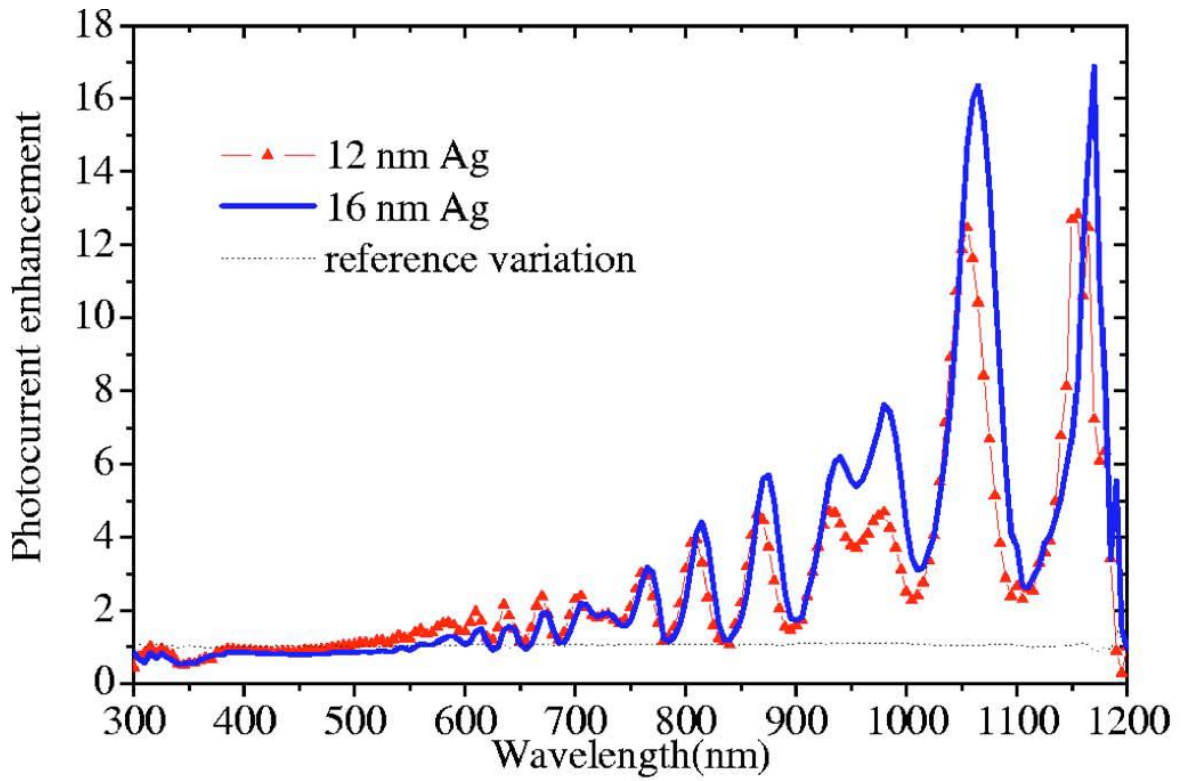
Figure 2.12: Photocurrent enhancement from silicon solar cells improved with Ag NPs with different dimensions. Reprint with permission from ref.[131] Copyright 2015, American Institute of Physics.

References

[1] http://www.webexhibits.org/pigments/indiv/history/zincwhite.html.

[2] H. Heiland, E. Mollwo and F. Stöckmann, Solid State Phys. **8**, 191 (1959).

[3] C. Klingshirn, ChemPhysChem **8**, 782-803 (2007).

[4] P. R. Bueno, J. A. Varela and E. Longo, J. Eur. Ceram. Soc. **28**, 505-529 (2008).

[5] P. R. Bueno, J. A. Varela, C. M. Barrado, E. Longo and E. R. Leite, J. Am. Ceram. Soc. **88**, 2629-2631 (2005).

[6] M. E. Brown (Ed.), *ZnO-Rediscovered* (The New Jersey Zinc Company, New York, 1957).

[7] Z. L. Wang, Mat. Today **7**, 26-33 (2004).

[8] A. Janotti and C. G. Van de Walle, Rep. Prog. Phys. **72**, 126501 (2009).

[9] D. C. Look, Mater. Sci. Eng. B **80**, 383-387 (2001).

[10] D. C. Look, J. W. Hemsky and J. R. Sizelove, Phys. Rev. Lett. **82**, 2552 (1999).

[11] A. F. Holleman, E. Wiberg, *Inorganic Chemistry* (Academic Press, San Diego, 2001).

[12] L. Li, K. Yu, Y. Wang and Z. Zhu, Appl. Surf. Sci. **256**, 3361-3364 (2010).

[13] D. M. Bagnall, Y. F. Chen, M. Y. Shen, Z. Zhu, T. Goto and T. Yao, J. Cryst. Growth **184**, 605-609 (1998).

[14] H. Kato, J. Cryst. Growth **538**, 237-239 (2002).

[15] K. Minegishi, Y. Koiwai, Y. Kikuchi, K. Yano, M. Kasuga and A. Shimizu, Jpn. J. Appl. Phys. **36**, L1453 (1997).

[16] D. C. Look, D. C. Reynolds, C. W. Litton, R. L. Jones, D. B. Eason and G. Cantwell, Appl. Phys. Lett. **81**, 1830 (2002).

[17] F. X. Xiu, Z. Yang, l. J. Mandalapu, D. T. Zhao, J. L. Liu and W. P. Beyermann, Appl. Phys. Lett. **87**, 152101 (2005).

[18] C. Jagadish and S. J. Pearton (eds.), *Zinc oxide bulk, thin films and nanostructures: processing, properties and applications* (Elsevier, Amsterdam, 2006).

[19] Ü. Özgür, Y. I. Alivov, C. Liu, A. Teke, M. A. Reshchikov, S. Doğan, V. Avrutin, S. J. Cho and H. Morkoç, J. Appl. Phys. **98**, 041301-103 (2005).

[20] S. J. Pearton, D. P. Norton , K. Lp, Y. W. Heo and T. Steiner, Superlattices Microstruct. **34**, 3-32, (2003).

[21] K. Ellmer, A. Klein and B. Rech, *Transparent Conductive Zinc Oxide Basics and Applications in Thin Film Solar Cells* (Springer, Berlin, 2008).

[22] J. C. Phillips, *Bonds and Bands in Semiconductors* (Academic Press, New York, 1973).

[23] D. P. Singh, Sci. Adv. Mater. **2**, 245-272 (2010).

[24] A. Janotti and C. G. Van de Walle, Phys. Rev. B **76**, 165202 (2007).

[25] A. Umar, C. Ribeiro, A. Al-Hajry, Y. Masuda and Y. B. Hahn, J. Phys. Chem. C **113**, 14715-14720 (2009).

[26] J. Q. Hua and Y. Bando, Appl. Phy. Lett. **82**, 1401 (2003).

[27] A. Mang, K. Reimann and S. Rübenacke, Solid State Commun. **94**, 251-254 (1995).

[28] T. Makino, Y. Segawa, M. Kawasaki, A. Ohtomo, R. Shiroki, K. Tamura, T. Yasuda and H. Koinuma, Appl. Phys. Lett. **78**, 1237 (2001).

[29] A. Ohtomo, M. Kawasaki, T. Koida, K. Masubuchi, H. Koinuma, Y. Sakurai, Y. Yoshida, T. Yasuda and Y. Segawa, Appl. Phys. Lett. **72**, 2466 (1998).

[30] M. Ghosh and A. K. Raychaudhuri, J. Appl. Phys. **100**, 034315 (2006).

[31] S. Y. Huang, S. Xu, J. W. Chai, Q. J. Cheng, J. D. Long and K. Ostrikov, Mater. Lett. **63**, 972-974 (2009).

[32] K. Reimann, M. Steube, D. Fröhlich and S. J. Clarke, J. Cryst. Growth **189**, 652-655 (1998).

[33] S. W. Kim, S. Fujita and S. Fujita, Appl. Phys. Lett. **81**, 5036 (2002).

[34] J. Nishii, F. M. Hossain, T. Aita, Y. Ohmaki, S. Kishimoto, T. Fukumura, Y. Ohno, H. Ohno, S. Takagi, K. Saikusa, I. Ohkubo, A. Ohtomo, F. Matsukura, H. Koinuma and M. Kawasaki, Jpn. J. Appl. Phys. **42**, L 347 (2003).

[35] P. Chang, Z. Fan, W. Tseng, D. Wang, W. Chiou, J. Hong and J. G. Lu, Chem. Mater. **16**, 5133-5137 (2004).

[36] W. I. Park, J. S. Kim, G. C. Yi, M. H. Bae and H. J. Lee, Appl. Phys. Lett. 85, 5052-5054 (2004).

[37] P. Wagner and R. Helbig, J. Phys. Chem. Solids **35**, 327 (1974).

[38] Y. R. Ryu and T. S. Lee, Appl. Phys. Lett. **83**, 87-89 (2003).

[39] A. Hernández Battez, R. González, J. L. Viesca, J. E. Fernández, J. M. Díaz Fernández, A. Machado, R. Chou and J. Riba, Wear **265**, 422-428 (2008).

[40] X. D. Bai, P. X. Xiao and Z. Wang, Appl. Phys. Lett. **82**, 4806-4808 (2003).

[41] G. Carlotti, D. Fioretto, G. Socino and E. Verona, J. Phys.: Condens. Matter **7**, 9147 (1995).

[42] F. C. Porter, *Zinc Handbook: Properties, Processing, and Use in Design* (Taylor and Francis: CRC Press, 1991).

[43] A. D. Corso, M. Posternak, R. Resta and A. Baldereschi, Phys. Rev. B **50**, 10715 (1994).

[44] H. Wan and H. E. Ruda, J. Mater. Sci.: Mater. Electron. **21**, 1014-1019 (2010).

[45] A. Menzel, K. Subannajui, R. Bakhda, Y. Wang, R. Thomann and M. Zacharias, J. Phys. Chem. Lett. **3**, 2815-2821 (2012).

[46] Y. C. Kong, D. P. Yu, B. Zhang, W. Fang , S. Q. Feng, Appl. Phys. Lett. **78**, 407 (2001).

[47] W. Lu, C. Jiang, D. Caudle, C. Tang, Q. Sun, J. Xu and J. Song, Phys. Chem. Chem. Phys. **15**, 13532 (2013).

[48] S. C. Lyu, Y. Zhang and C. J. Lee, Chem. Mater. **15**, 3294 (2003).

[49] H. Simon, T. Krekeler, G. Schaan and W. Mader, Cryst. Growth Des. **13**, 572 (2013).

[50] S. Lin, H. Hu, W. Zheng, Y. Qu and F. Lai, Nanoscale Res. Lett. **8**, 158 (2013).

[51] H. J. Fan, R. Scholz, F. M. Kolb, M. Zacharias, U. G¨osele, F. Heyroth, C. Eisenschmidt, T. Hempel and J. Christen, Appl. Phys. A **79**, 1895 (2004).

[52] C. H. Ku, H. H. Yang, G. R. Chen and J. J. Wu, Cryst. Growth Des. **8**, 283-290 (2008).

[53] H. M. Cheng, H. C. Hsu, S. Yang, C. Y. Wu, Y. C. Lee, L. J. Lin and W. F. Hsieh, Nanotechnology **16**, 2882 (2005).

[54] B. Weintraub, Y. Deng and Z. L. Wang, J. Phys. Chem. C **111**, 10162-10165 (2007).

[55] S. Zhang, Y. Shen, H. Fang, S. Xu, J. Song and Z. L. Wang, J. Mater. Chem. 20, 10606-10610 (2010).

[56] J. Elias, R. T. Zaera and C. L. Cle´ment, J. Electroanal. Chem. **621**, 171 (2008).

[57] S. Sanchez, C. L. Clément and V. Ivanova, J. Electrochem. Soc. **159**, 705 (2012).

[58] Z. Haibo, C. Jingbiao, C. Bingqiang, G. Ursula, B. Yoshio and G. Dmitri, Sci. Adv. Mater. **2**, 336-358 (2010).

[59] L. Ding, R. Zhang and L. Fan, Nanoscale Res. Lett. **8**, 78 (2013).

[60] W. I. Park, G. C. Yi, M. Kim, S. J. Pennycook, Adv. Mater. **14**, 1841 (2002).

[61] H. Yuan , Y. Zhang, J. Cryst. Growth **263**, 119 (2004).

[62] Y. W. Heo, V. Varadarajan, M. Kaufman, K. Kim, D. P. Norton, F. Ren and P. H. Fleming, Appl. Phys. Lett. **81**, 3046 (2002).

[63] H. Ono and S. Iizuka, J. Nanomater. **2011**, 850930 (2011).

[64] M. Purahmad, M. A. Stroscio , M. Dutta, J. Electron. Mater. **43**, 740 (2014).

[65] A. Rahm, M. Lorenz, T. Nobis, G. Zimmermann, M. Grundmann, B. Fuhrmann and F. Syrowatka, Appl. Phys. A **88**, 31 (2007).

[66] R. Guo, J. Nishimura, M. Matsumoto, M. Higashihata, D. Nakamura and T. Okada, Jpn. J. Appl. Phys. **47**, 741 (2008).

[67] Y. Li, G. W. Meng, L. D. Zhang, F. Phillipp, Appl. Phys. Lett. **76**, 2011 (2000).

[68] J. J. Wu, H. I. Wen, C. H. Tseng , S. C. Liu, Adv. Funct. Mater. **14**, 806 (2004).

[69] Q. Xu, Q. Cheng, Z. Zhang, R. Hong, X. Chen, Z. Wu and F. Zhang, J. Alloys Compd. **590**, 260-265 2014.

[70] S. Xu , Z. L. Wang, Nano Res. **4** , 1013 (2011).

[71] W. Peng, S. Qu, G. Cong and Z. Wang, Cryst. Growth Des. **6**, 1518-1522 (2006).

[72] R. A. Laudise and A. A. Ballman, J. Phys. Chem. **64**, 688-691(1960).

[73] L. N. Demianets, D. V. Kostomarov, I. P. Kuz'mina and S. V. Pushko, Crystallogr. Rep. **47**, S86-S98 (2002).

[74] A. Kawska, P. Duchstein, O. Hochrein and D. Zahn, Nano Lett. **8**, 2336-2340 (2008).

[75] L. N. Dem'yanets, D. V. Kostomarov and I. P. Kuz'mina, Inorg. Mater. **38**, 124 (2002).

[76] L. Vayssieres, Adv. Mater. **15**, 464-466 (2003).

[77] D. S. Boyle, K. Govender and P. O'Brien, Chem. Commun. **1**, 80-81(2002).

[78] I. S. Ahuja, C. L. Yadava and R. Singh, J. Mol. Struct. **81**, 229-234 (1982).

[79] H. Zhang, D. Yang, X. Ma, N. Du, J. Wu and D. Que, J. Phys. Chem. B **110**, 827-830 (2006).

[80] K. Govender, D. S. Boyle, P. B. Kenway and P. O'Brien, J. Mater. Chem. **14**, 2575-2591(2004).

[81] J. Wanga and L. Gao, J. Mater. Chem. **13**, 2551-2554 (2003).

[82] H. M. Smith and A. F. Turner, Appl. Opt. **4**, 147 (1965).

[83] http://groups.ist.utl.pt/rschwarz/rschwarzgroup_files/PLD_files/PLD.htm

[84] K. Yadav, B. R. Mehta and J. P. Singh, J. Mater. Chem. C **2**, 6362-6369 (2014).

[85] D. Yu, T. Trad, J. T. McLeskey Jr, V. Craciun and C. R. Taylor, Nanoscale Res. Lett. **5**, 1333-1339 (2010).

[86] M. H. Huang, S. Mao, H. Feick, H. Yan, Y. Wu , H. Kind, E. Weber, R. Russo and P. Yang, Science **292**, 1897 (2001).

[87] J. Liu, W. Wu, S. Bai and Y. Qin, ACS Appl. Mater. Interfaces **3**, 4197–4200 (2011).

[88] D. Yu , T. Trad, J. T. M. Jr, V. Craciun and C. R. Taylor, Nanoscale Res. Lett. **5**, 1333 (2010).

[89] M. H. Huang, Y. Wu, H. Feick, N. Tran, E. Weber and P. Yang, Adv. Mater. **13**, 113 (2001).

[90] R. S. Wagner and W. C. Ellis, Appl. Phys. Lett. **4**, 89 (1964).

[91] H. J. Choi, in *Semiconductor Nanostructures for Optoelectronic Devices, processing, characterization, and applications*, ed. G. -C. Yi (Springer-Verlag, Berlin, 2012) Chap.1.

[92] D. S. Kim, R. Ji, H. J. Fan, F. Bertram, R. Scholz, A. Dadgar, K. Nielsch, A. Krost, J. Christen, U. Gösele and M. Zacharias, Small **3**, 76-80 (2007).

[93] D. S. Kim, R. Scholz, U. Gösele and M. Zacharias, Small, **4**, 1615-1619 (2008).

[94] Z. Chenga and J. Lin, CrystEngComm. **12**, 2646-2662 (2010).

[95] D. B. Mitzi, K. Chondroudis and C. R. Kagan, IBM J. Res. & Dev. **45**, 29-45 (2001).

[96] H. J. Snaith, J. Phys. Chem. Lett. **4**, 3623-3630 (2013).

[97] S. A. Bhalla, R. Guo and R. Roy, Mater. Res. Innovations **4**, 3-26 (2000).

[98] S. Kazim, M. K. Nazeeruddin, M. Grätzel and S. Ahmad, Angew. Chem. Int. Ed. **53**, 2812-2824, (2014).

[99] D. B. Mitzi, J. Chem. Soc. Dalton Trans. 1-12 (2000).

[100] J. L. Knutson, J. D. Martin , D. B. Mitzi, Inorg. Chem. **44**, 4699-4705 (2005).

[101] H. S. Kim, C. R. Lee, J. H. Im, K. B. Lee, T. Moehl, A. Marchioro, S. J. Moon, R. H. Baker, J. H. Yum, J. E. Moser, M. Gra¨tzel and N. G. Park, Sci. Rep. **2**, 591(2012).

[102] J. H. Im, C. R. Lee, J. W. Lee, S. W. Park , N. G. Park, Nanoscale **3**, 4088-4093 (2011).

[103] G. Xing, N. Mathews, S. Sun, S. S. Lim, Y. M. Lam, M. Grätzel, S. Mhaisalkar and T. C. Sum, Science **342**, 344-347(2013).

[104] S. Sun, T. Salim, N. Mathews, M. Duchamp, C. Boothroyd, G. Xing, T. C. Sum and Y. M. Lam, Energy Environ. Sci. **7**, 399-407 (2014).

[105] T. Miyasaka, Chem. Lett. 44, 720-729 (2015).

[106] Y. Takahashi, R. Obara, Z. Z. Lin, Y. Takahashi, T. Naito, T. Inabe, S. Ishibashi and K. Terakura, Dalton Trans. **40**, 5563 (2011).

[107] C. C. Stoumpos, C. D. Malliakas and M. G. Kanatzidis, Inorg. Chem. **52**, 9019-9038 (2013).

[108] A. E. Becquerel, C. R. Acad. Sci. **9**, 561-567 (1839).

[109] W. G. Adams and R. E. Day, Proc. Roy. Soc. A **25**, 113-117 (1877).

[110] C. E. Fritts, Am. J. Sci. **26**, 465-472 (1883).

[111] J. Czochralski, Z. Physik. Chem. **92**, 219-221 (1918).

[112] D. M. Chapin, C. S. Fuller and G. L. Pearson, J. Appl. Phys. **25**, 676-677 (1954).

[113] H. Tsubomura, M. Matsumura, Y. Nomura and T. Amamiya, Nature **261**, 402-403 (1976).

[114] C. W. Tang, Appl. Phys. Lett. **48**, 183 (1986).

[115] B. O'Regan and M. Grätzel, Nature **353**, 737-740 (1991).

[116] M. Grätzel, Chem. Lett. **34**, 8-13 (2005).

[117] A. Kojima, K. Teshima, Y. Shirai and T. Miyasaka, J. Am. Chem. Soc. **131**, 6050 (2009).

[118] M. M. Lee, J. Teuscher, T. Miyasaka, T. N. Murakami and H. J. Snaith, Science **338**, 643-647 (2012).

[119] M. Liu, M. B. Johnston and H. J. Snaith, Nature **501**, 395-398 (2013).

[120] J. M. Ball, M. M. Lee, A. Hey and H. J. Snaith, Energy Environ. Sci. **6**, 1739-1743 (2013).

[121] S. D. Stranks, G. E. Eperon, G. Grancini, C. Menelaou, M. J. P. Alcocer, T. Leijtens, L. M. Herz, A. Petrozza and H. J. Snaith, Science **342**, 341-344 (2013).

[122] C. F. Bohren and D. R. Huffman, *Absorption and Scattering of Light by Small Particles* (Wiley, New York, 1983).

[123] K. A. Willets and R. P. Van Duyne, Annu. Rev. Phys. Chem. **58**, 267 (2007).

[124] E. Petryayeva and U. J. Krull, Anal. Chim. Acta **706**, 8-24 (2011).

[125] K. T. Yonga, Y. Sahoo, M. T. Swihart and P. N. Prasad, Colloids Surf. A **290**, 89 (2006).

[126] X. Lu, M. Rycenga, S. E. Skrabalak, B. Wiley and Y. Xia, Annu. Rev. Phys. Chem. **60**, 167 (2009).

[127] B. J. Wiley, S. H. Im, Z. Y. Li, J. McLellan, A. Siekkinen and Y. Xia, J. Phys. Chem. B **110**, 15666-15675 (2006).

[128] B. J. Wiley, Y. Chen, J. M. McLellan, Y. Xiong, Z. Y. Li, D. Ginger and Y. Xia, Nano Lett. **7**, 1032-1036 (2007).

[129] L. M. Liz-Marzán, Langmuir **22**, 32-41(2006).

[130] H. Ko, S. Singamaneni and V. V. Tsukruk, Small **4**, 1576-1599 (2008).

[131] S. Pillai, K. R. Catchpole, T. Trupke and M. A. Green, J. Appl. Phys. **101**, 093105 (2007).

[132] K. Nakayama, K. Tanabe and H. A. Atwater, Appl. Phys. Lett. **93**, 121904 (2008).

[133] H. A. Atwater and A. Polman, Nature Mater. **9**, 205 (2010).

[134] J. R. Lakowicz, Anal. Biochem. **324**, 153-169 (2004).

[135] J. R. Lakowicz, K. Ray, M. Chowdhury, H. Szmacinski, Y. Fu, J. Zhang and K. Nowaczyk, Analyst **133**, 1308-1346 (2008).

[136] M. Moskovits, J. Raman Spectrosc. **36**, 485-496 (2005).

[137] C. Hrelescu, T. K. Sau, A. L. Rogach, F. Jäckel and J. Feldmann, Appl. Phys. Lett. **94**, 153113 (2009).

[138] J. Qi, X. Dang, P. T. Hammond and A. M. Belcher, ACS Nano **5**, 7108-7116 (2011).

[139] W. Zhang, M. Saliba, S. D. Stranks, Y. Sun, X. Shi, U. Wiesner and H. J. Snaith, Nano Lett. **13**, 4505-4510 (2013).

[140] T. Kawawaki, H. Wang, T. Kubo, K. Saito, J. Nakazaki, H. Segawa and T. Tatsuma, ACS Nano **9**, 4165-4172 (2015).

[141] P. K. Jain, X. Huang, I. H. El-Sayed and M. A. El-Sayed, Plasmonics **2**, 107-118 (2007).

[142] M. E. Stewart, C. R. Anderton, L. B. Thompson, J. Maria, S. K. Gray, J. A. Rogers and R. G. Nuzzo, Chem. Rev. **108**, 494-521 (2008).

[143] J. A. Schuller, E. S. Barnard, W. Cai, Y. C. Jun, J. S. White and M. L. Brongersma, Nat. Mater. **9**, 368 (2010).

[144] D. Derkacs, W. V. Chen, P. M. Matheu, S. H. Lim, P. K. L. Yu and E. T. Yu, Appl. Phys. Lett. **93**, 091107 (2008).

[145] A. J. Morfa, K. L. Rowlen, T. H. Reilly III, M. J. Romero and J. v. de Lagemaat, Appl. Phys. Lett. **92**, 013504 (2008).

[146] B. Rand, P. Peumans and S. R. Forrest, J. Appl. Phys. **96**, 7519 (2004).

CHAPTER THREE

Fabrication and Characterization of Zinc Oxide Nanostructures

ZnO has demonstrated to be a possible alternative to TiO_2 for perovskite solar cells due to its comparable energy levels and sufficient electron transport and light scattering properties. ZnO NSs and their growth processes are described in this section. Relatively low temperature RE method was considered for ZnO NSs growth. The growth of the ZnO NSs without any catalyst and with Ag NPs seeded-layer as well as their diverse characterizations used to elucidate the morphological evolutions, structural and optical properties are described in this chapter. The characterization techniques employed for this study are FE-SEM, TEM, EDX, XRD, and PL spectroscopy. The principles of these techniques are explained in this section.

3.1 ZINC OXIDE NANOSTRUCTURES

Over the past few decades, nanostructured materials have been the subjects of broad interest because of their promising applications in optoelectronics, catalysis, sensing applications and so on. The properties of nanostructured materials can be dissimilar considerably from their bulk counterpart due to their extremely small sizes. The nanomaterials exhibit some unique properties, such as high aspect ratio and large surface area to volume ratio, which are commonly not observed in their usual bulk counterpart. The nanomaterials can be normally categorized in the one-dimensional (1D) nanostructures, two-dimensional (2D) nanostructures and three-dimensional (3D) nanostructures. 1D nanostructure support a direct conduction path for electrons and offer improved electron transfer compare to those of bulk and thin-film materials.[1] Due to the aforementioned advantages, the studies on nanomaterials are escalated and are spreading rapidly. In addition, the metal-oxide nanomaterials have attracted attention because of their wonderful structural adaptability associated with their unique properties. Therefore, the combinations of the benefits of NSs along with the unique properties of metal-oxide

nanomaterials make the investigations very important issues in research and development from the viewpoint of basic science and its application.

In the midst of miscellaneous metal-oxides, ZnO is one of the most prominent semiconductor materials because of its exclusive properties, such as a range of conductivity depends on doping, high transparency, piezoelectricity, room temperature (RT) ferromagnetism, wide bandgap semiconductivity (~ 3.37 eV at RT with a large exciton binding energy of 60 mV), chemical-sensing effects and so forth.[2-5] Moreover, the ease of crystallization as well as the anisotropic growth of ZnO allows it to be formed in a wide variety of NSs, such as NWs,[6-10] nanorods,[11,12] nanotubes,[13] nanoribbons,[14-16] and nanoflowers.[17] Particularly, ZnO NWs as a quasi-1D material, possess a high density of states at the band edge because of the radial quantum confinement effect that offer a great potential for various electronics applications. Therefore, the rich diversity of NSs along with their unique properties are advantageous for practical applications in the areas of optoelectronics,[18] sensors,[19] piezoelectronics,[20] field-effect transistors,[21] light-emitting diodes,[22] DSCs,[23-25] organic-inorganic hybrid perovskite solar cells,[26-28] and so forth. Hence, controlled synthesis of ZnO NSs, especially NWs under mild conditions is one of the most important issues nowadays.

3.2 FABRICATION OF ZNO NANOSTRUCTURES

ZnO NSs have been fabricated by using a range of techniques as discussed in the previous section of the literature review. Regardless of the success of these techniques, there are various disadvantages associated with their growth process, for example, the need to control a high vacuum level, the use of high growth temperature and poisonous gases, the high experimental cost as well as the process needed for preparing samples are very complexes with a huge experimental cost. To avoid such above mentioned obstacles on

growth of ZnO NSs, a promising method which have assorted advantages, for examples rapid growth, easy controllable, low-temperature, non-toxic, catalyst-free and low-cost are necessary. In this respect, the RE method occupies a rare place in modern science and technology.

The RE was first reported by Aüwarter in 1952,[29] and Brinsmaid *et al.* in 1953.[30] In 1960, the RE was applied for several oxides and their high temperature depositions on substrates were studied.[31] Their concerns were mainly in epitaxial growth. Around 20 years later, Heitmann in 1971, used RE for the deposition of oxide films through evaporation by using plasma as a reactive gas,[32] and this method is presently named as activated reactive evaporation.[33] A comprehensive study of the deposition, morphology and properties of the thin films have been discussed in the following literatures.[34,35]

3.2.1 Reactive evaporation growth of ZnO nanostructures

The RE is the principal technique in this dissertation and, therefore, comprehensive studies of this method are indispensable in order to carry on for advanced applications. The RE method cannot be categorized as PVD method. A primary discrepancy among the RE and PVD is that the PVD method has direct deposition, in contrast, the RE consists of a quartz chamber to control vapor from the source of evaporation. Therefore, the RE method is rather treated as CVD because of chemical reactions, such as oxidation, and reduction of ZnO, take place during the growth of ZnO NSs. The RE method has several advantages, for example, it does not have any drain water, discharge gas, and waste slag. The procedures convoluted in preparing samples under this method are very easy, cost effective and controllable because the sample compositions can be maximized precisely by adjusting a few experimental conditions. Manifold morphologies of ZnO NSs synthesized on FTO glass substrates are presented in this thesis.

3.2.1.1 Fabrication procedures

Self-organized ZnO NSs including NW were grown on FTO-coated glass substrates by using RE method without presence of any catalysts, as described elsewhere.[36] The synthesis was performed in a vacuum chamber. Before loading into the vacuum chamber, the substrates with a sheet resistivity of 7Ω/sq (Solaronix S.A, Switzerland) were cleaned by ultra-sonication in Semicoclean 23 (Furuuchi Chemical, Semicoclean 23), deionized water, acetone and 2-propanol, as well as blown by clean dried nitrogen.[37] After finished the surface treatments, the substrates were soon moved to the deposition chamber and placed at the top of an alumina crucible, which loaded with highly pure metal Zn powder (Furuuchi Chemical, 99.999%, 100 mesh) serving as source material.

The vertical distance between the Zn source and FTO-coated glass substrate was set to a value about 32 cm. The crucible temperature (T_{cru}) of the Zn source was set to the constant value of 400 °C for controlling the deposition rate of metal Zn. Subsequently, the substrate temperature (T_{sub}) was fixed to the convenient value ranges of 300 - 500 °C. Once the T_{sub} reached to the target value, an uninterrupted flow of highly pure oxygen gas (99.999%) was introduced into the quartz chamber through a specifically designed substrate holder to control the flow of oxygen as shown in Fig. 3.1. The oxygen pressure (P_{oxy}) in the vacuum chamber was kept at 3.9×10^{-2} Pa. by using a controlled needle valve and pumping during growth.

Samples with different growth times (t_{grow}) and T_{sub} are selected to investigate the morphological change and the formation mechanism of ZnO NWs. In parallel, Ag films of 1 - 15 nm was deposited further on FTO substrate prior to the growth of ZnO NSs due to investigate the effect of metal NPs on morphology of ZnO NSs. During the growth of NSs, the P_{oxy} was kept from 2.6 - 5.3×10^{-2} Pa. The amount of NWs obtained was controlled by

adjusting the T_{cru}, T_{sub}, and t_{grow}. After growth, the oxygen flow, T_{sub}, and T_{cru} were discontinued and the samples were left in the chamber for cooling down.
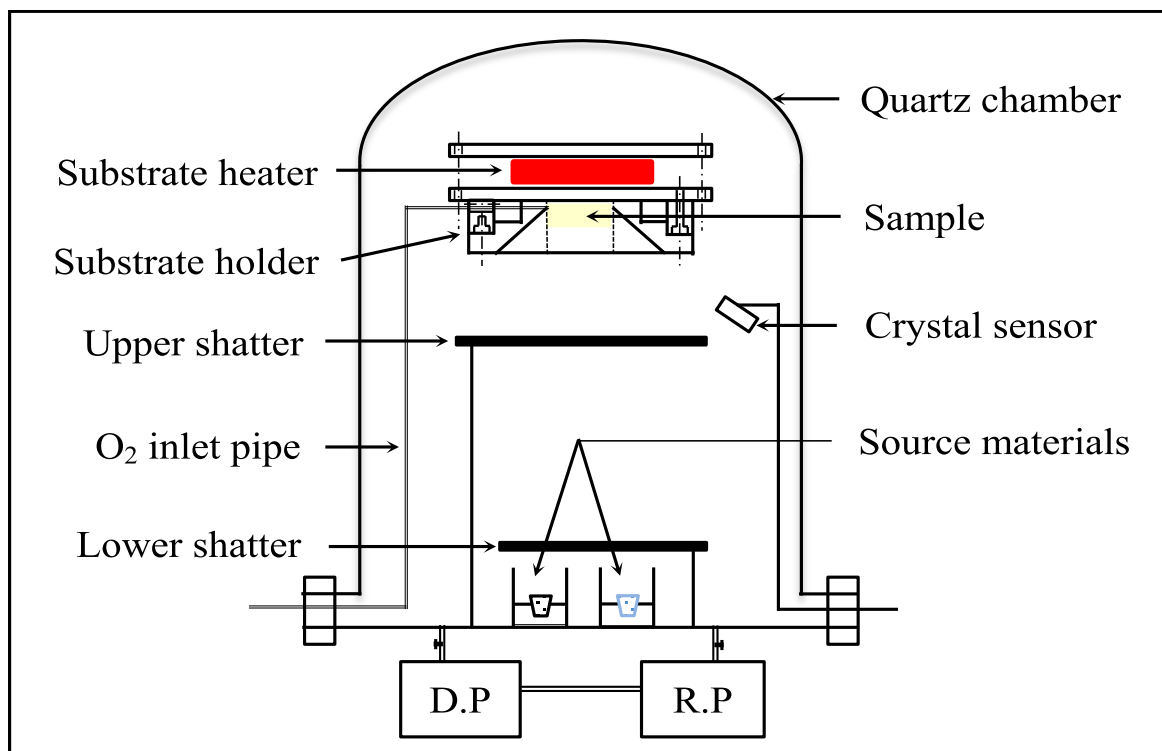
Figure 3.1: Schematic experimental setup and the synthesis system for growing ZnO NSs on the FTO-coated glass substrate without any catalysts or additives.

3.3 CHARACTERIZATIONS AND MEASUREMENTS

Characterizations of the synthesized NSs are the most essential part for studying the morphology, structures and phases, optical properties and so on. The surface morphologies of the self-organized ZnO NSs were observed by FE-SEM (JEOL, JSM-6340F). The elemental analyses of the samples were carried out by using energy EDX analyzer attached to the FE-SEM. The crystal orientation of the ZnO NWs was determined further using a high-resolution TEM (Hitachi H-7650). The structure and phase characterization of the ZnO NSs were inspected by XRD. The patterns of XRD were recorded through Bruker AXS (D8 ADVANCE) X-ray

diffractometer equipped by the Cu Kα (λ = 1.54056 Å) X-ray tube conducted at 40 kV and 40 mA using a step-size of 0.02° and a time per step of 2 s. Under these conditions, the experimental fitting of the X-ray data was carried out from 20-70° in the 2θ ranges. The optical properties of the ZnO NSs were characterized by PL measurement (Spectrofluorometer; JASCO, FP-8300) at room temperature with an excitation wavelength of 325 nm at an incident angle of 45°. The fundamental of major characterization techniques used in this study were discussed below.

3.3.1 Characterization techniques

3.3.1.1 Field-emission scanning electron microscopy

SEM is of crucial importance as it considers one of the powerful tools for materials characterization. The fundamental of the electron microscope is identical to the optical microscope. The optical microscope uses visible light as a source, whereas the electron microscope uses very energetic electrons. Therefore, the magnification of the optical microscope is restricted by its wavelengths compared with the electron microscope operated by the accelerated electrons which possess very short wavelengths. This is exactly what makes it attainable to observe very small features at nano level.

In the electron microscope, electrons possess very small wavelengths which can be changed with the applied voltages. The wavelength, λ of an electron is related to its momentum, $p = mv$, through the Planck constant, h (6.626 x 10^{-34} Js) by:[38]

$$\lambda = \frac{h}{p} = \frac{h}{mv}$$
(3.1)

where m is the mass and v refers to the velocity of the electron. The high energy electrons are speed up the velocities which is roughly similar to the velocity of light, c (2.998 x 10^{8}

m/s). In this case, considerations of relativistic effects are essential at such high velocities. The relativistic mass of an electron by:

$$m = \frac{m_e}{\sqrt{1-(v/c)^2}}$$ (3.2)

where e is the charge on an electron (1.602 x 10^{-19} C) and m_e is the rest mass of electron (9.109 x 10^{-31} kg). The energy of the electron is eV and is related to the relativistic change in mass in the form:

$$eV = (m - m_e) \, c^2$$ (3.3)

From the above equations 3.1, 3.2 and 3.3 the electron wavelength can be summarized as a function of accelerated voltage:

$$\lambda = \frac{1.5}{\sqrt{V(1+V*10^{-6})}} \, nm$$ (3.4)

for instance an accelerated voltage of 10 kV will change to a wavelength of 0.0122 nm, which is extremely smaller than the visible light (3.9 × 10^{-7} ~ 7.8 × 10^{-7} m). It is thus possible to observe the atomic structures of the materials by using extremely small-scale wavelengths through the accelerated electrons.

In an SEM, a high-energy electron beam scans the sample-surface and interacts with the atoms in a way that generate the emission of secondary electrons. These secondary electrons, such as backscattered electrons, photons (characteristic X-rays), visible light (cathodoluminescence), specimen current and transmitted electrons are detected by the sensor or detector which forms the images. The backscattered electrons reflected from the samples through elastic scattering,[39] are used for imaging in a standard detection mode of SEM. The information captured from the secondary electrons reveal useful signals about the surface of the sample containing: its surface features, sizes and shapes of the features.

The orientation of the surface features affects the direction of the emission of the secondary electrons. A schematic illustration of SEM is shown in Fig. 3.2.
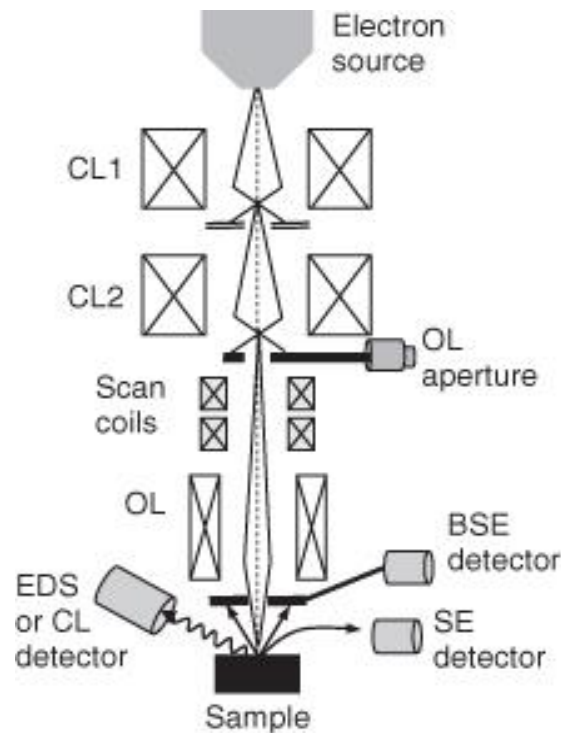
Figure 3.2: Schematic illustration of basic SEM setup. Adapted from ref.[39]

In case of high-resolution FE-SEM, field emission gun is used in place of conventional tungsten filaments. A field emission gun produces an electron beam with an extremely high current density, obtained by applying an intense electric field to a tungsten single crystal with a needle-shaped tip. Furthermore, a field-emission cathode supports narrower electron beam as well as high electron energy, resulting in both enhanced spatial resolution and reduced sample-charging and damages. In this dissertation, the FE-SEM measurement was performed due to analyzed the ZnO NSs and perovskite film morphology. The FE-SEM analysis was carried out at JEOL, JSM-6340F, operating at acceleration voltages of 5 - 15 kV.

3.3.1.2 Transmission electron microscopy

SEM is a common used method for fast and easy analysis the surface morphology of objects, while TEM allows more detailed study of the inner structures with resolutions down to the atomic level. By using TEM, information on local crystal structures, crystal orientations as well as the lattice defects can be obtained. A primary electrons beam transmitted through the object are utilized for TEM image formation. Images are high-quality and detailed. However, in case of FE-SEM image, the secondary electrons are used. The basic setup of a TEM shows similarities to SEM is shown in Fig. 3.3.

Due to ensure the transmission of electrons through the sample, acceleration voltages like few hundred kV and sample thicknesses of usually less than 100 nm are essential. Therefore, sample preparation is a difficult task for TEM analysis that involves various processing steps including focused ion beam processing or sputter etching and so on. On the contrary, nanostructure sample can be easier to make through the dispersion of NSs simply on a copper mesh or conductive carbon, may often be adequate for basic TEM analysis. TEM can be conducted in different modes, explaining various properties of the sample. In a bright-field mode, typical image can be recorded, while diffraction patterns are obtained only from a selected area of the sample (selected-area electron diffraction, SAED) by inserting an aperture in the transmitted beam path. The resolution of TEM can be upgraded even lower to atomic level when it operates in high-resolution mode. Image contrast is attained by way of phase shift between the transmitted electron wave and diffracted electron wave. The diffracted wave consists of information about atom arrangements in the sample, while the transmitted electron wave aids as a reference phase. Therefore, the HRTEM image can be treated as an interference pattern of both diffracted and incident electron waves. The HRTEM image enables detail information on local variations in the crystal structure, lattice defects, such as stacking faults, nanostructure

growth directions and interfaces. In this work, a Hitachi H-7650 TEM operating at 100kV was employed due to elucidate the structural details and crystallinity of individual ZnO NSs. Corresponding samples were prepared by scratching the NSs off the as-grown substrate and dispersing them on a conductive carbon mesh.
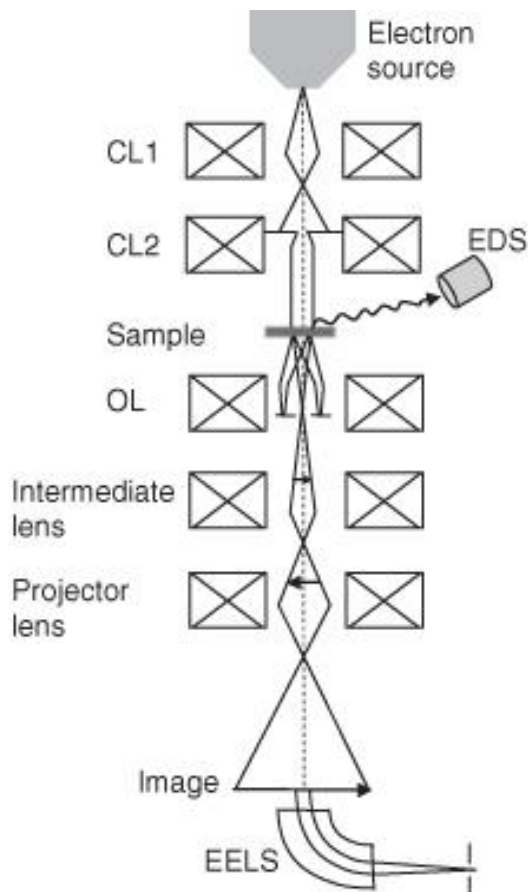
Figure 3.3: Schematic illustration of basic TEM setup and its main components. Adapted from ref.[39]

3.3.1.3 X-ray diffractometer

The atoms are arranged periodically in a solid crystal and the distances between atoms are typically on the order of few Ångström. Due to probe such specific crystal by using EM radiation, wavelengths on the same order of magnitude or lower are essential. XRD techniques can therefore be employed to reveal information about chemical composition,

crystallographic structure, lattice parameters as well as lattice stress and crystal grain sizes. The waves diffracted from different atoms can intervene with each other resulting in an intensity distribution pattern which consists of information on the crystal structure. For radiation to intervene constructively, the difference in path lengths of the particular rays reflected from the lattice planes must be an integer multiple of the wavelength λ as shown in Fig. 3.4.
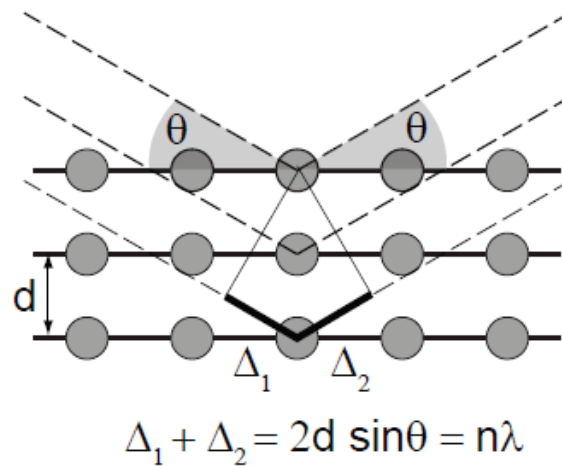
Figure 3.4: Schematic illustration of the Bragg condition. Adapted from ref.[40]

In the case of two adjacent lattice planes, this difference is equal to $2d\sin\theta$ for any arbitrary angle θ of the X-rays. The relationship between X-rays wavelength and inter-plane space d is given by Bragg's law,[41] which can be written as

$$2d\sin\theta = n\lambda \tag{3.5}$$

where λ is the wavelength, θ is the scattering angle, and the integer n depicting the order of diffraction peak (usually $n = 1$). The planes spacing are associated with lattice constants a, c, and Miller indices h, k, and l by the following relationship.[41,42]

$$\frac{1}{d_{hkl}^2} = \frac{4}{3}\left(\frac{h^2 + hk + k^2}{a^2}\right) + \frac{l^2}{c^2} \tag{3.6}$$

with the first order approximation, n = 1:

$$a = \frac{\lambda}{2\sin\theta} \sqrt{\frac{4}{3}\left(h^2 + hk + \frac{l^2}{(c/a)^2}\right)} \qquad (3.7)$$

and

$$c = \frac{\lambda}{2\sin\theta} \sqrt{\frac{4}{3\,(a/c)^2}\left(h^2 + hk + l^2\right)} \qquad (3.8)$$

Furthermore, the average crystallite size can be estimated through the Debye-Scherrer formula,[43] which uses the full-width at half-maximum (FWHM) value of XRD diffraction peak. The formula of Debye-Scherrer is presented as

$$d = \frac{k\,\lambda}{\left(\beta_{obs}^2 - \beta_{ins}^2\right)^{1/2}\cos\theta_B} \qquad (3.9)$$

where β_{obs} is the FWHM or the estimated broadening for a diffraction peak, β_{ins} is instrumental broadening, k is Scherrer's constant, the X-rays wavelength, $\lambda = 0.154$ nm and θ_B is the angle of Bragg diffraction. $\beta = \left(\beta_{obs}^2 - \beta_{ins}^2\right)^{1/2}$ is the FWHM of the diffraction peaks after correcting for peak broadening which is caused by the diffractometer.

In this work, structure and phase characterization of the ZnO NSs and $CH_3NH_3PbI_3$ perovskite were inspected by XRD. A schematic illustration of XRD setup is shown in Fig. 3.5. The patterns of XRD were recorded through the Bruker AXS (D8 ADVANCE) X-ray diffractometer. It was equipped by the fixed Cu Kα ($\lambda = 1.54056$ Å) X-ray tube, a monochromator, a goniometer and sample stage as well as a movable X-ray scintillation detector arm with a set of collimating and anti-scattering slits. The sample height and lateral positions were regulated by electrical drives on the sample stage. For measurement, the X-ray tube was conducted at 40 kV and 40 mA using a step-size of 0.02° and a time per step of 2 s. Under these conditions, the experimental fitting of XRD data was carried

out from 20-70° in the 2θ range. The measured spectra thus reveal information about the crystal structure and grain size as well as the lattice constant/interplanar spacing *d*.
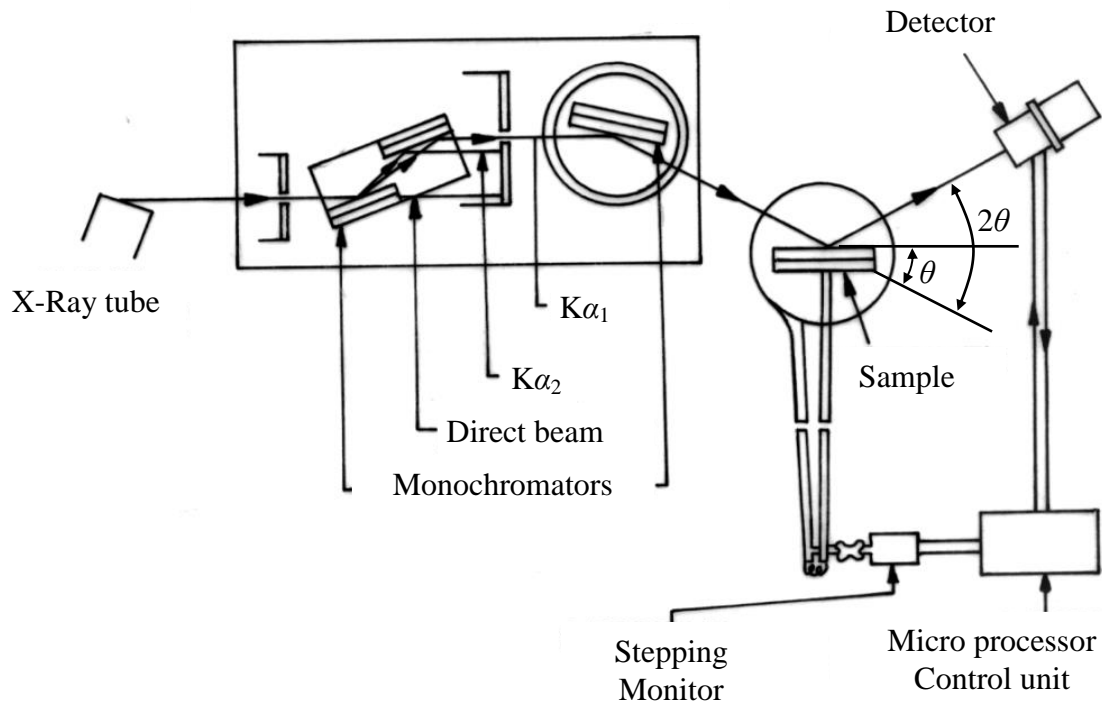
Figure 3.5: Schematic illustration of XRD setup.

3.3.1.4 Photoluminescence Spectroscopy

PL is a very powerful technique typically carried out due to investigate the semiconductor materials. In PL measurement, the materials are excited by a light source such as He-Cd laser with 325 nm, or diode laser with 405 nm, or Nd:YAG pulsed laser having wavelength of 266 nm, or Ar^+ laser with wavelengths of 316 nm/514 nm/488 nm, or a *X*enon lamp and measure the spontaneous emission of the samples by using detectors. A schematic illustration of room temperature PL setup is shown in Fig. 3.6. By varying the experimental parameters, such as very low temperature of around 4K in the PL setup, different information can be obtained.
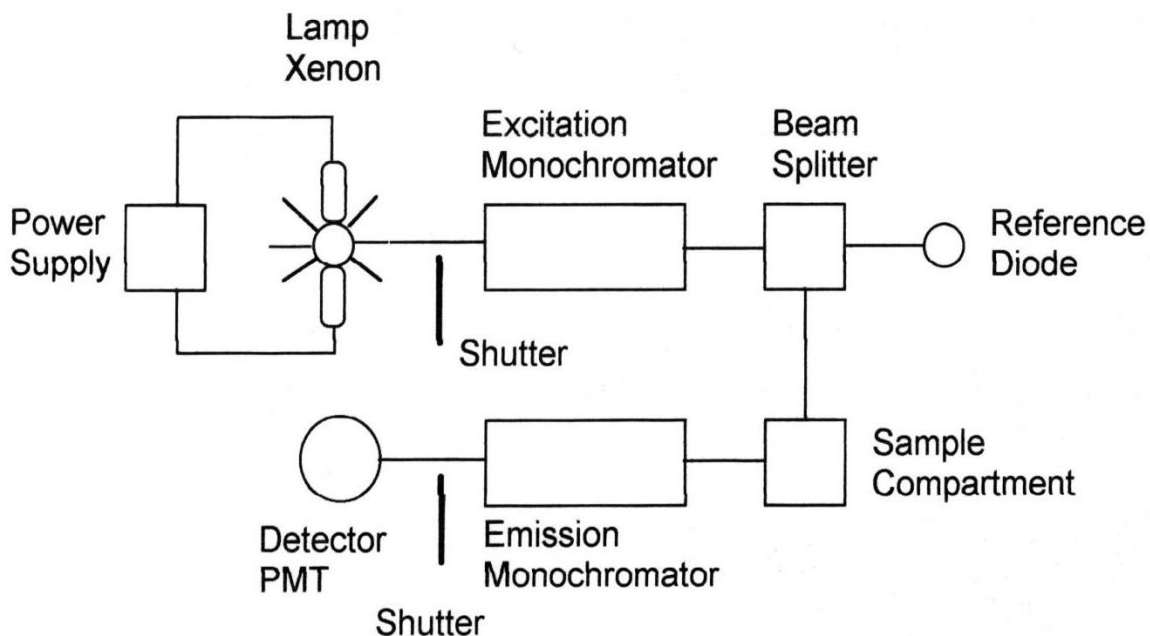
Figure 3.6: A schematic illustration of room temperature PL setup.

In PL measurement, the excitation takes place when the energy of a photon is higher than band gap energy of the material. Photons are emitted when the electrons move from an excited state to a ground state. The observed spectrum consist of information of transition energies, *i.e*., electronic band structure. The spectrum intensity reveals the relative rate of radiative and non-radiative recombination. In radiative recombination process, the electron-hole pair is recombined followed by emission of photon as shown in Fig. 3.7.[44] Non-radiative process ensures no emission of photons instead the energy, commonly converts into vibrational energy of phonons. The peaks intensity as a function of illumination time can be evaluated the photo-stability of the material. The energy position and intensity of PL peaks rely upon the nature of material components.
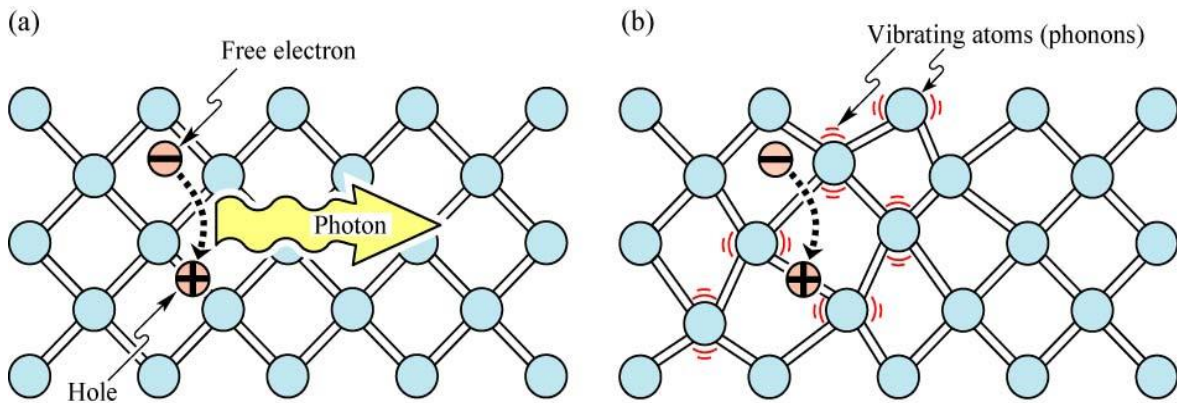
Figure 3.7: (a) Radiative recombination of an electron-hole pair accompanied by the emission of photon with energy $h\upsilon \approx E_g$. (b) In non-radiative recombination events, energy released during the electron-hole recombination is converted to photons.[44]

In this dissertation, the PL measurement was employed at RT to study the ZnO NSs. In case of ZnO NSs, a PL spectrum usually contains two emission bands can be classified as near band edge emission (NBE) and deep level emission (DLE) as shown in Fig. 3.8.
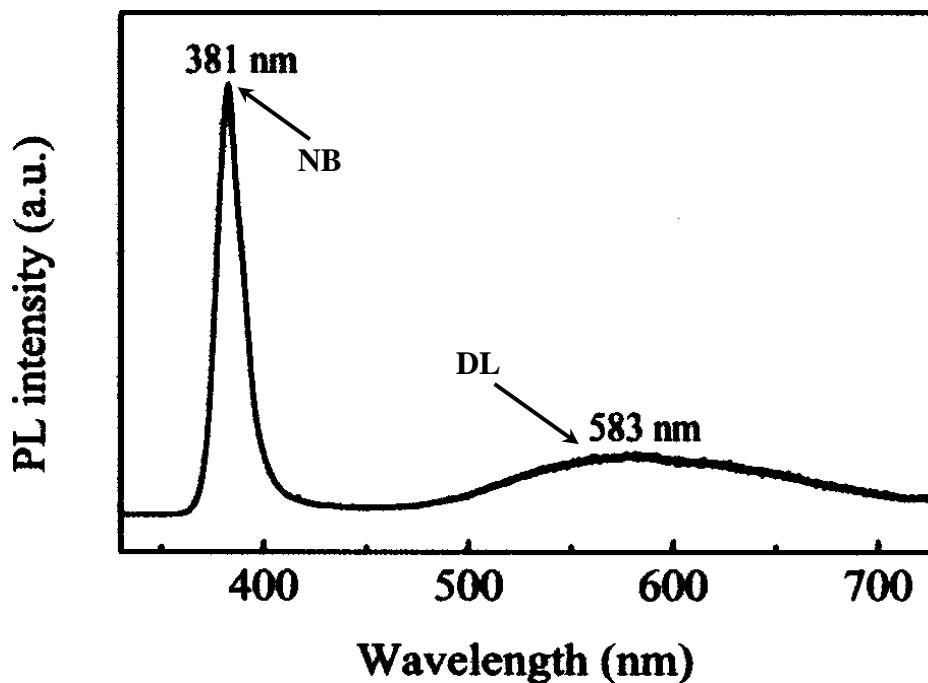
Figure 3.8: Room-temperature PL spectrum of the as-grown ZnO NWs. Reprint with permission from ref.[45] Copyright 2015, American Institute of Physics.

NBE is induced by either the free excitons or the excitons bound to the shallow level, donor acceptor pairs (DAP) and so forth. However, the DLE is caused through the carriers bound to the deep levels and the emission spectrum cover a range from around 420 to 700 nm in the visible range. The DLE is thought to be caused by some defects in the crystal structures, for instance, oxygen and zinc vacancies (V_o and V_{zn}), oxygen and zinc interstitial (O_i and Zn_i) and some other substitutional atoms such as Cu.

3.4 RESULTS AND DISCUSSIONS

3.4.1 Analysis of FE-SEM

3.4.1.1 Temperature-dependent growth

The T_{sub} is a critical parameter that influences the adsorption, surface diffusion and chemical reaction rate of Zn species, thus affecting the growth of ZnO nuclei as well as the ZnO NSs.[46] Figure 3.9 shows the representative FE-SEM images of the surface of ZnO NSs grown on FTO substrate for 30 min at T_{sub} of 300, 400, 450, and 500 °C. Note that the sizes of the ZnO NSs given below are typical diameter and apparent length viewed from the surface normal direction.

In the case of the lowest T_{sub} (300 °C), no specific ZnO NSs were grown as shown in Fig. 3.9(a), because the T_{sub} is not enough to activate the chemical reaction between Zn and oxygen. Under this T_{sub}, desorption of Zn atoms from the substrate occurs without forming ZnO. Indeed, EDX measurements of the surface did not show any peaks associated with Zn as shown in Fig. 3.9(b). The elemental spectra of oxygen (O), silicon (Si), and tin (Sn) are presented prominently. These peaks are from the FTO substrate.

Very small dot-like NSs were formed randomly on the substrate as shown in Fig. 3.9(c), when the T_{sub} was set to 400 °C. The inset shows a magnified FE-SEM image of the dot-like NSs. The diameter and length of these dot-like NSs were around 16 nm and 24

nm, respectively. Apparently, at this T_{sub} the chemical reactions lead to the nucleation of ZnO. Figure 3.9(d) shows the result at T_{sub} of 450 °C. The diameter and length of the ZnO NWs were around 56 nm and 260 nm, respectively. The diameters of NWs decreased along their growth direction, which results in a needle-like topography of the NWs. In the FE-SEM image, one can observe a large number of ZnO NWs grown at different angles from the surface of the substrate, and some appear in flower-like bunches as indicated in Fig. 3.9(d).

At T_{sub} of 500 °C, the long ZnO NWs were grown uniformly across the substrate as shown in Fig. 3.9(e). The diameter and length of the ZnO NWs were around 46 nm and 310 nm, respectively. The inset shows that the ZnO NWs have tapered ends like needles. The taper-like structures can be explained in terms of thermodynamical stability; in the absence of catalyst termination of NWs at (001) surface is energetically unfavorable because the (001) surface of ZnO is polar and has a high surface energy. Therefore, the ZnO NWs take taper-like structures. Taper shaped ZnO NWs also observed in the presence of a catalyst. At elevated temperatures, the NWs base expansion might occur after growth by surface diffusion.[47] Yuan *et al.*[48] reported that the growth of tapered-shape NWs occurs *via* surface diffusion of Zn ions along the side wall of the NWs, which results in simultaneous growth in both the axial and radial directions by reacting with oxygen. This mechanism can also be at work also in our case. The EDX spectrum in Fig. 3.9(f) also illustrates that the synthesized NWs consist of only Zn and O elements without noticeable impurities. Si and Sn signals are due to the FTO glass substrate. Overall the aspect ratio increases with the increases of T_{sub}.
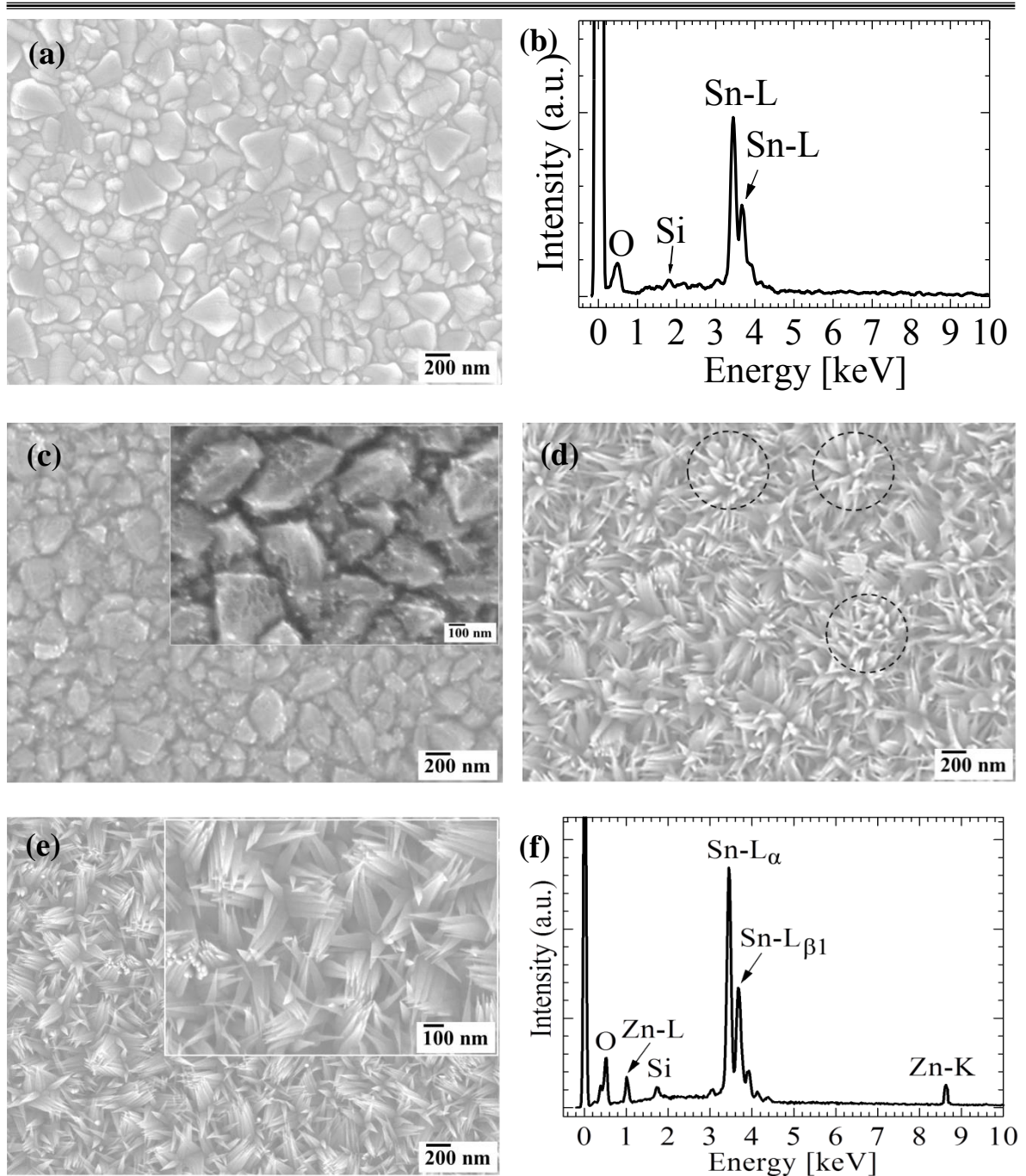
Figure 3.9: FE-SEM images of ZnO NSs grown on FTO glass substrates at the T_{sub} of (a) 300, (c) 400, (d) 450, and (e) 500 °C for 30 min respectively. (b) EDX spectra of the ZnO NSs grown on FTO glass substrates at the T_{sub} of 300 °C for 30 min. (f) EDX spectra of the ZnO NSs grown on FTO glass substrates at the T_{sub} of 500 °C for 30 min.

3.4.1.2 Time-dependent growth

To further elucidate the morphological variations of ZnO NSs, the time-dependent analysis has been carried out performing a set of experiments with different t_{grow}. Figure 3.10 (a-d) displays the FE-SEM images of ZnO NSs fabricated on FTO substrates holding the t_{grow} for 15, 20, 45, and 60 min, respectively. Figure 3.10(a) shows the growth result using the t_{grow} of 15 min. Many discrete, very small-sized ZnO NWs were formed on the FTO substrates. The average diameter and length of the NWs were around 11 nm and around 50 nm, respectively, and most of the NWs formed on the edge of the FTO facets instead of the flat surface area. This can be attributed to the higher bond energy at the edge of the faceted FTO substrate. The inset of Fig. 3.10(a) shows the EDX result collected from the area of Fig. 3.10(a) where no NWs were observed by the FE-SEM analysis. Indeed, the elemental spectra of Zn, O, Si, and Sn presented prominently. The presence of Zn and O elements may claim the formation of a thin ZnO layer on the top of substrate because, no peak of Zn metal were detected in the XRD spectrums shown in the XRD result.

When the t_{grow} was increased to 20 min, some honeycomb-like structures were formed through the interconnected NWs as shown in Fig. 3.10(b). The diameter and length of NWs were around 14 nm and 60 nm, respectively, and it was likely uniform over the entire surface of the FTO substrates. By further raising the t_{grow} to 45 min, the extended NWs were observed as shown in Fig. 3.10(c). The diameter and length of NWs were about 62 nm and 300 nm, respectively. Having a close-up view, very tiny NWs were straight-up to the large NWs along their growth direction. The similar features of NWs were observed further, when the t_{grow} increased to 60 min as shown in Fig. 3.10(d). In this case, the diameter and length of the NWs were around 70 nm and 340 nm, respectively. Formation of tiny sized NWs may be ascribed the two-step growth at their growth front because of

Zn-rich vapor environment. Zhang *et al.*[49] also reported that the secondary growth at the growth-front of NWs should be a zinc-rich process due to small O_2 gas flow.
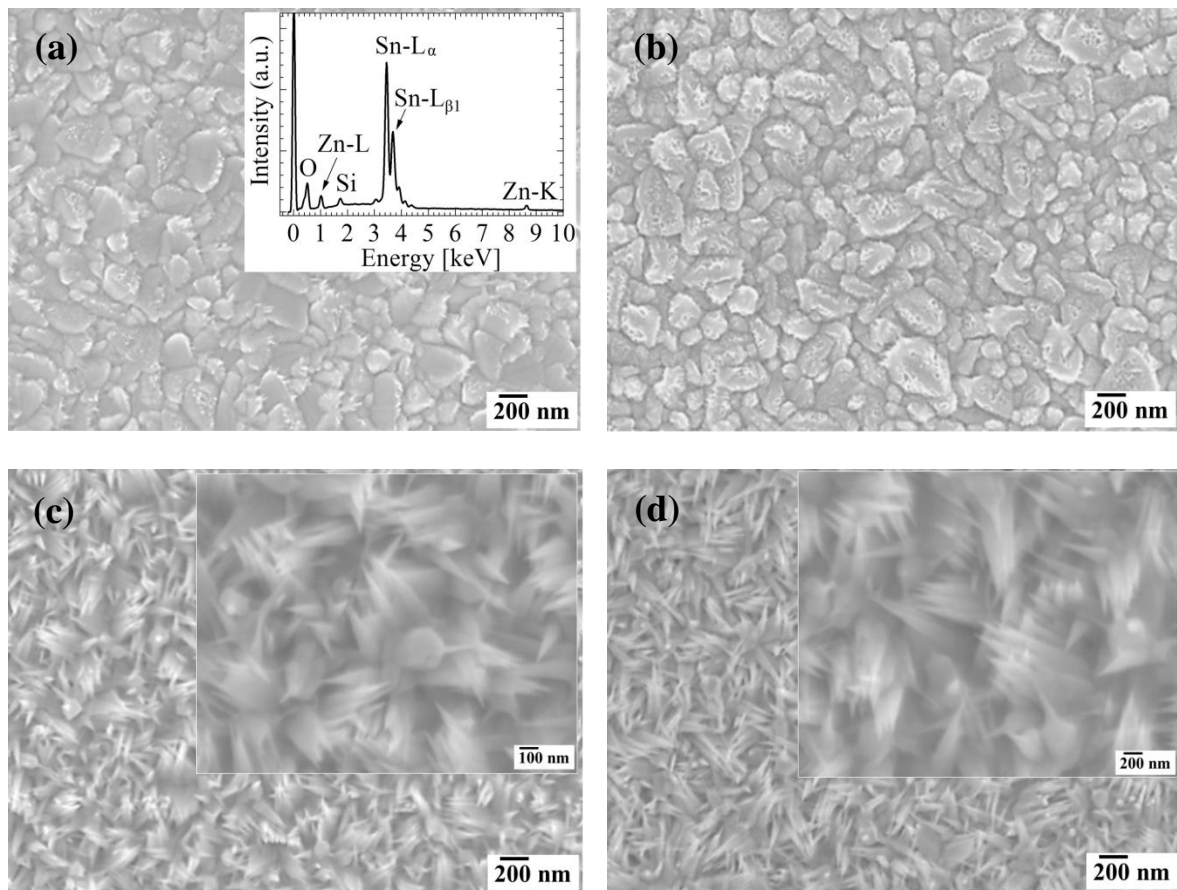
Figure 3.10: Top views of FE-SEM images of the ZnO NSs grown on FTO-coated glass substrate at T_{sub} of 500 °C for (a) 15, (b) 20, (c) 45, and (d) 60 min. The insets exhibit corresponding EDX spectra of the ZnO NSs.

3.4.1.3 Metal-seeded growth

The morphological effects of ZnO NSs were investigated on various samples prepared through different thickness of Ag films and P_{oxy}, while the T_{sub} and t_{grow} were kept at 500 °C and 30 min, respectively. This study chose Ag because that it is physically active, but chemically inert. By using PVD method, thin films of Ag were deposited on FTO glass substrates under dark environment at rates within 0.05 - 0.07 nm/s, followed by thermal

annealing. Note that the Ag films change to the NPs after annealing. The previous result of this study proved that the size of NPs varied by the film thickness, annealing temperatures and times. Figure 3.11 shows the top and perspective views (insets) of ZnO NWs grown on the 1, 3, 5, and 7 nm of thick Ag films.
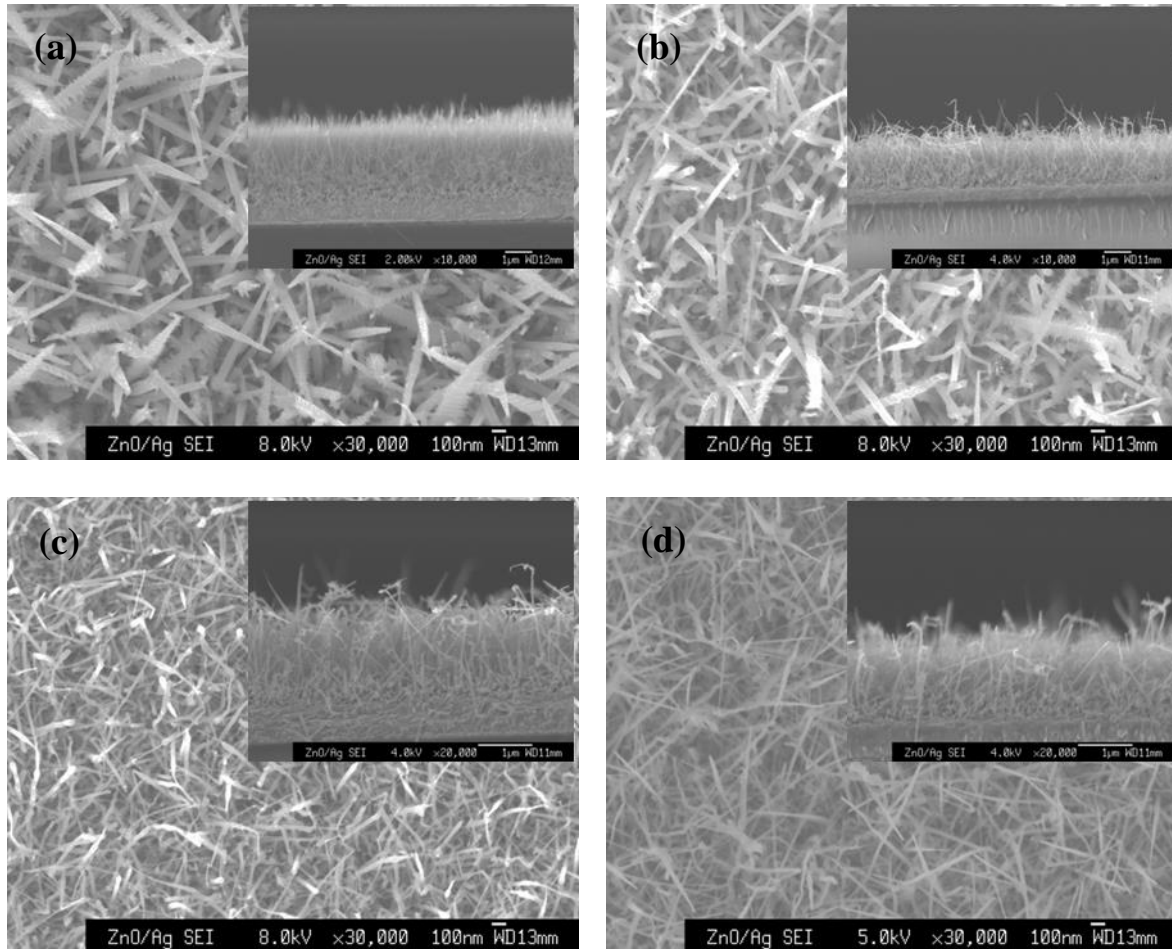
Figure 3.11: FE-SEM top and perspective views of ZnO NWs grown at T_{sub} of 500 °C for 30 min on (a) 1 nm, (b) 3 nm, (c) 5 nm and (d) 7 nm thick Ag films.

The diameters of ZnO NWs are about 55, 50, 40 and 35 nm for 1, 3, 5, and 7 nm of thick Ag films cases, respectively. One can observe that the highly dense ZnO NWs are taper like. The insets show that the NWs are typically aligned. The average lengths of the NWs are apparently 3, 2, 2.2 and 1.5 μm for 1, 3, 5, and 7 nm of thick Ag films cases, respectively. Ag NPs result in the narrowest and tallest nanowires compare with non-catalyst growth which has been discussed in the previous sections. Zhang *et.al.*[50] reported

that at 500 °C, Ag form liquid-phase droplets and start trapping Zn vapor with high accommodation efficiency. Therefore, it can be assumed that the growth of relatively uniform and longer NWs can be attributed to the liquid nanodroplets of Ag.

3.4.2 Summary of FE-SEM analysis

Based on the above mentioned experimental data, it can be summarized that the T_{sub}, t_{grow}, P_{oxy} and Ag layers over the substrate play crucial functions in controlling morphology of the ZnO NSs. The morphology of NWs, especially the size and shape substantially improve with the increase of T_{sub}. In the case of 300 °C, no specific NSs are recognized. The reasons for this may be very low T_{sub}, which is not enough to activate the chemical reaction between Zn and oxygen. However, the dot-like NSs were observed at 400 °C. Apparently, at this T_{sub} the chemical reactions lead to the nucleation of ZnO. When the T_{sub} increased to 450 °C and 500 °C, the ZnO NWs were observed. Overall the aspect ratio increases with the increases of T_{sub} as shown in Fig. 3.12 (a). Since the growth rate of length is higher than that of the diameter, the formation of NWs originates from a high growth rate along the c-axis direction, not along in-plane direction.

By using the t_{grow} of 15 min, very small-sized ZnO NWs of which most of the NWs were formed on the edge of the FTO facets instead of the flat-surface area. This can be attributed to the higher bond energy at the edge of the faceted FTO substrate. From the EDX results shown in the inset of Fig. 3.10(a) and XRD measurements, it can be assumed that very thin-layer of ZnO may form on the top of substrate, prior to the growth of NWs. When the t_{grow} increased to 20 min, some honeycomb-like structures were formed through the interconnected NWs. The diameter and length of ZnO NWs increases significantly with the increases of t_{grow} as shown in Fig. 3.12(b). However, in case of long t_{grow}, for instance 45 min and 60 min, very tiny NWs were observed straight-up to the large NWs

along their growth direction. Formation of tiny sized NWs may be ascribed the two-step growth because of Zn-rich vapor environment.
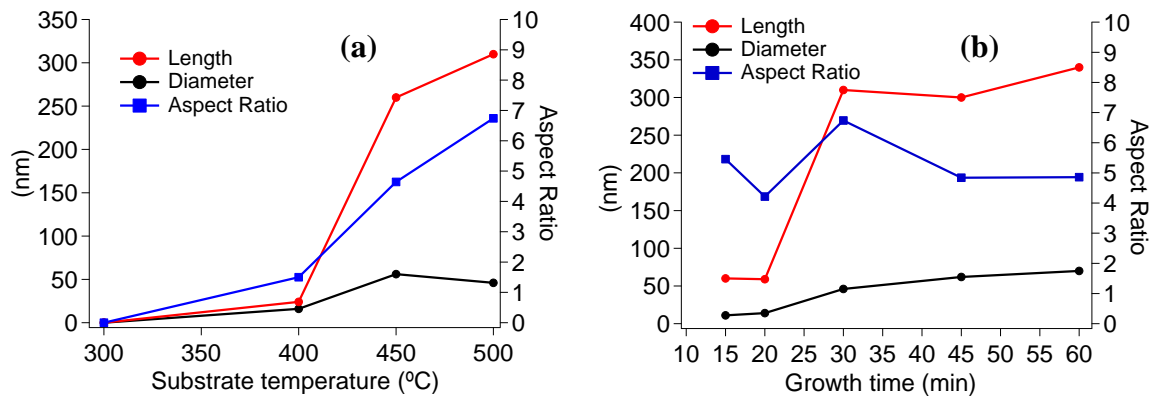
Figure 3.12: The length, diameter and aspect ratio of ZnO NSs are influenced by the (a) T_{sub} and (b) t_{grow}.

Conversely, Ag-assisted growth of ZnO NWs exhibit a different morphology compare to temperature-dependent and time-dependent growth without any catalyst. From this point of view, the Ag-assisted growth process results in the long NWs which are interconnected to each other and form a NW-NW junction or network-like morphologies. The synthesized NWs exhibit a good mechanical attachment to the FTO substrate was confirmed by the typical ultrasonic method.

3.4.3 Analysis of TEM

The structure and crystallinity of ZnO NWs were studied by TEM observations. Figure 3.13 exhibits the representative TEM images of single NW grown at a T_{sub} of 500 °C for 30 min. Synthesized NWs were peeled off from the substrates through scratching and placed in the cupper grid covered with carbon film for TEM analysis. The NW exhibits very smooth and clean surface throughout the length. Apparently, the diameter of the NW is around 60 nm and it is decreasing gradually toward the tip as shown in Fig. 3.13(a).
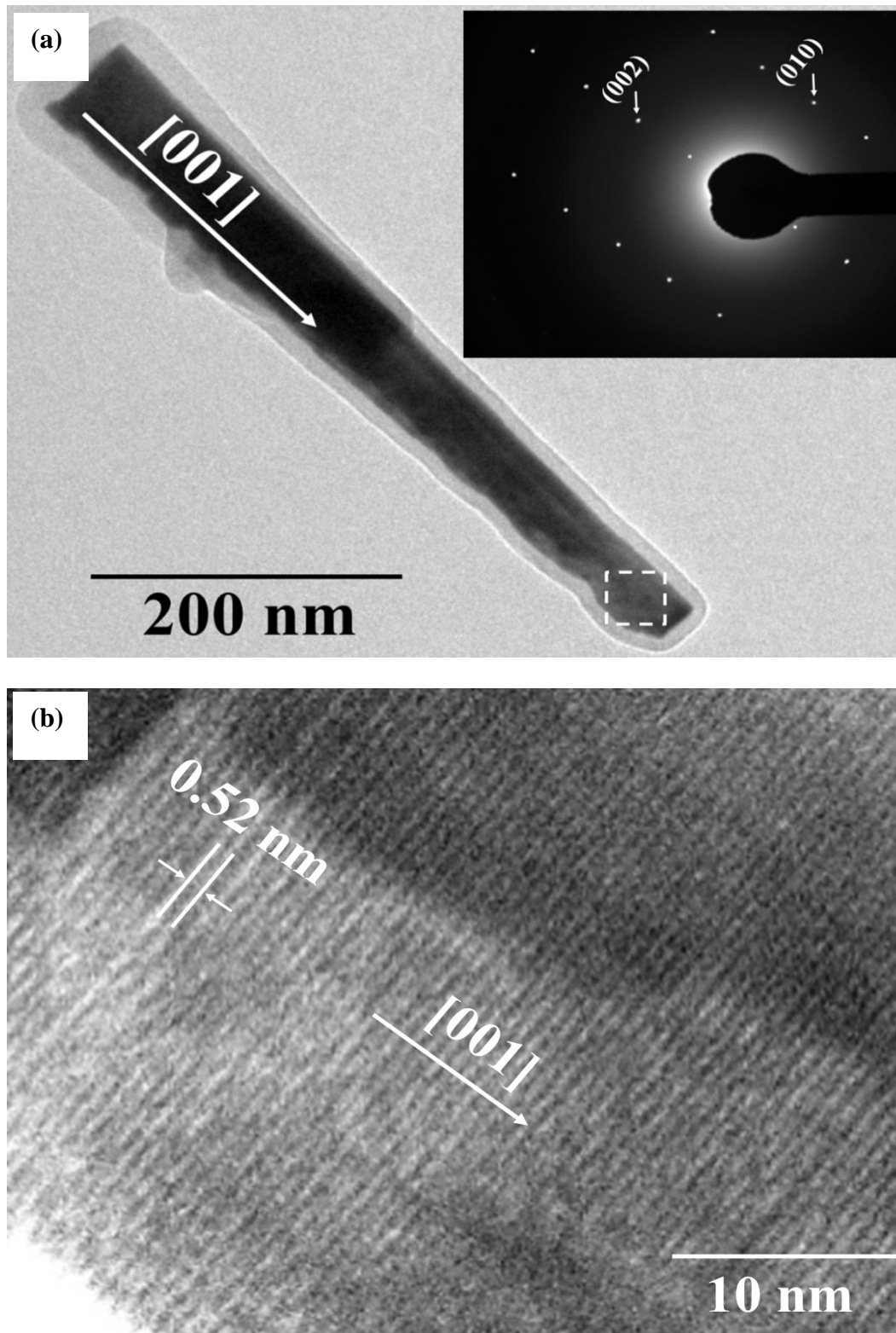
Figure 3.13: (a) TEM image of single ZnO NW grown at the T_{sub} of 500 °C for 30 min. (b) HRTEM image obtained from the selected portion in (a). The corresponding SAED pattern inset of Fig. 3.13(a), exhibits strong diffractions indicating highly crystallization.

Figure 3.13(b) shows the high resolution TEM (HRTEM) image which has been taken from rectangular area of the corresponding NW indicated in Fig. 3.13(a). The well-resolved lattice fringes were observed clearly from the HRTEM image. Estimated interplanar spacing was about 0.52 nm, which corresponds to the (001) crystal plane of wurtzite ZnO (hexagonal structure with the lattice constants of $a = 0.32$ nm and $c = 0.52$ nm), suggesting that the ZnO NWs are single-crystalline and preferentially grown along the [001] direction.[51] No extended defects, for example, dislocation and stacking fault were observed. The corresponding SAED pattern of the NW is shown in the inset of Fig. 3.13(a). The bright circular spots of SAED patterns also confirmed the good crystalline nature of the ZnO NWs. These patterns that can be indexed as wurtzite structure of hexagonal ZnO, which confirm that the ZnO NW is single crystal and grow along the *c*-axis direction.[52,53] The obtained TEM results are consistent with FE-SEM analysis and the XRD patterns, which will be discussed in the subsequent section.

3.4.4 X-ray diffraction analysis

To investigate the crystalline phase and structure of ZnO NSs, XRD measurement was conducted. Figure 3.14(a) shows the XRD patterns of samples grown on FTO substrates under various T_{sub} of (i) 500 °C, (ii) 450 °C and (iii) 400 °C for 30 min, while Fig 3.14(b) reveals the samples grown at 500 °C for various t_{grow} of (i) 60 min, (ii) 45 min, (iii) 30 min, (iv) 20 min and (v) 15 min. For all samples, the peaks that appeared at 2θ of 31.78°, 34.42°, 36.25°, 47.54°, 56.62°, and 62.87° represent the (100), (002), (101), (102), (110), and (103) planes, respectively, of the wurtzite crystal structure of ZnO according to the JCPDS card no. 00-036-1451. The peaks observed at approximately 26.73° and 52.25° were assigned to the (110) and (211) phases for FTO substrate (JCPDS card no. 01-072-1147), respectively.
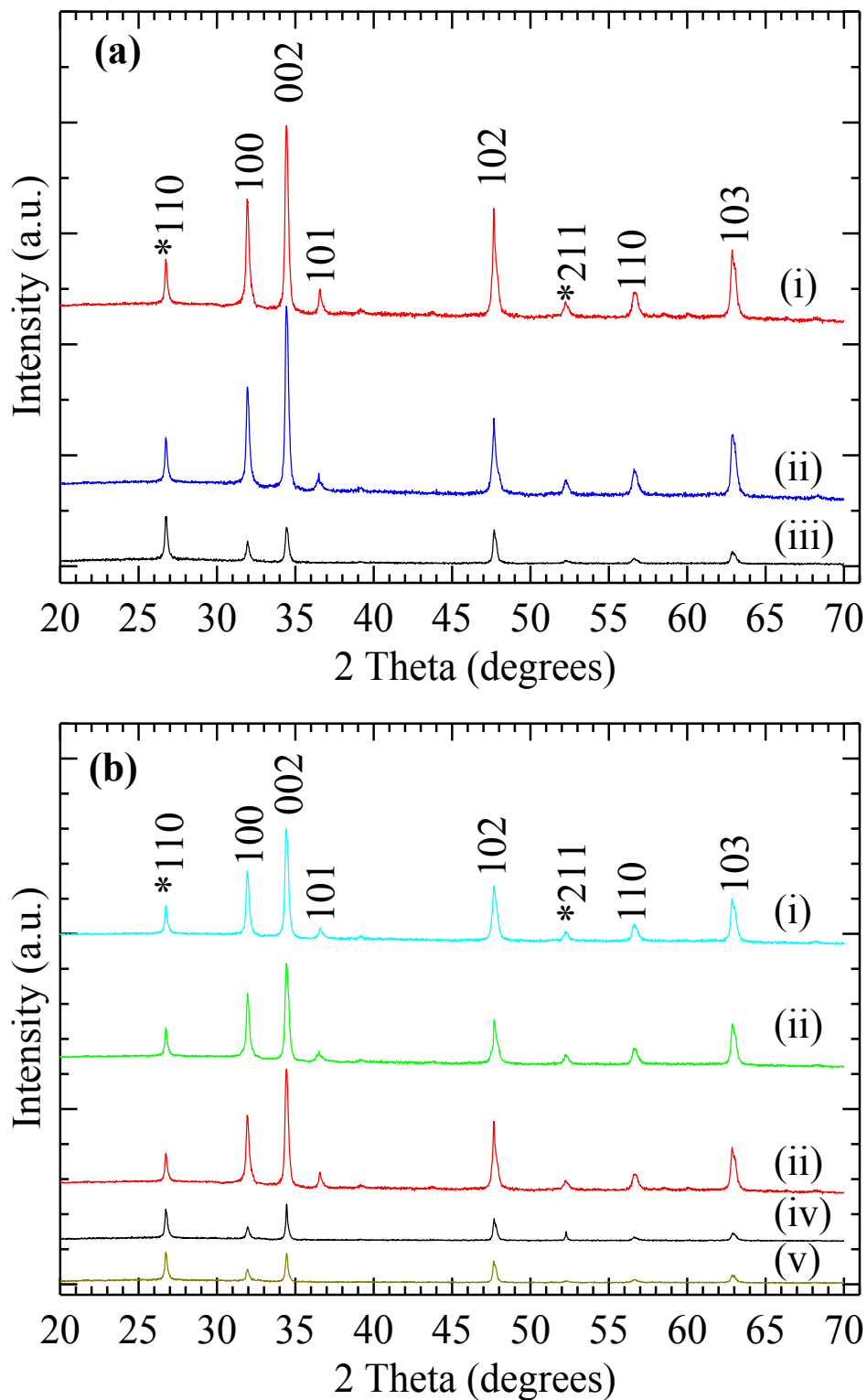
Figure 3.14: (a) XRD patterns of ZnO NSs grown on FTO substrates under various T_{sub} of (i) 500 °C, (ii) 450 °C and (iii) 400 °C for 30 min. (b) XRD patterns of ZnO NSs grown on FTO substrates at 500 °C for various t_{grow} of (i) 60 min, (ii) 45 min, (iii) 30 min, (iv) 20 min and (v) 15 min. Peaks marked with asterisk originate from the FTO substrate.

No excess peaks of impurities (such as metallic Zn) were detected in the XRD spectrums, thereby confirming the complete conversion of metallic Zn powder to ZnO NSs. It is worthwhile to mention that, the peak positions obtained in all patterns are almost same, which indicates all the NSs are of the same materials, *i.e.*, ZnO.[54] In all the patterns, the ZnO (002) peak at 34.42° is dominant over all other peaks as shown in Fig. 3.14(a) and 3.14(b). This is attributed to the highly preferred growth of ZnO NWs along their *c*-axis direction. This is also confirmed by TEM analysis. The *c*-axis is the favorable growth direction because the polar (001) crystal plane of ZnO has a high surface energy which directs the growth front. The intensities of all diffraction peaks relatively increase with increasing T_{sub} from 400 to 500 °C, reflecting that the amount of crystalline ZnO NSs may increase at a higher T_{sub}. Furthermore, the lattice constants of the ZnO NWs estimated by the TEM analysis were of $a = 0.32$ nm and $c = 0.52$ nm. The observed crystallographic parameters are very close to the standard values reported for ZnO in the literature.[55] These values are almost close to those of bulk ZnO, suggesting that the synthesized ZnO NWs features a high crystal quality. These XRD results are consistent with the PL results, which will be discussed in the next section.

3.4.5 Photoluminescence properties

The ultraviolet and visible PL spectra of the ZnO NSs were measured on a Spectrofluorometer using a *X*enon-lamp as a source of excitation with an excitation wavelength of 325 nm under RT. PL spectra of ZnO NSs grown at different T_{sub} and t_{grow} are shown in Fig. 3.15. In all the samples, there is a strong with sharp emission in the UV region around 372 nm and other very week emission band in the visible region around 460 nm are shown in the Fig 3.15(a) and 3.15(b).
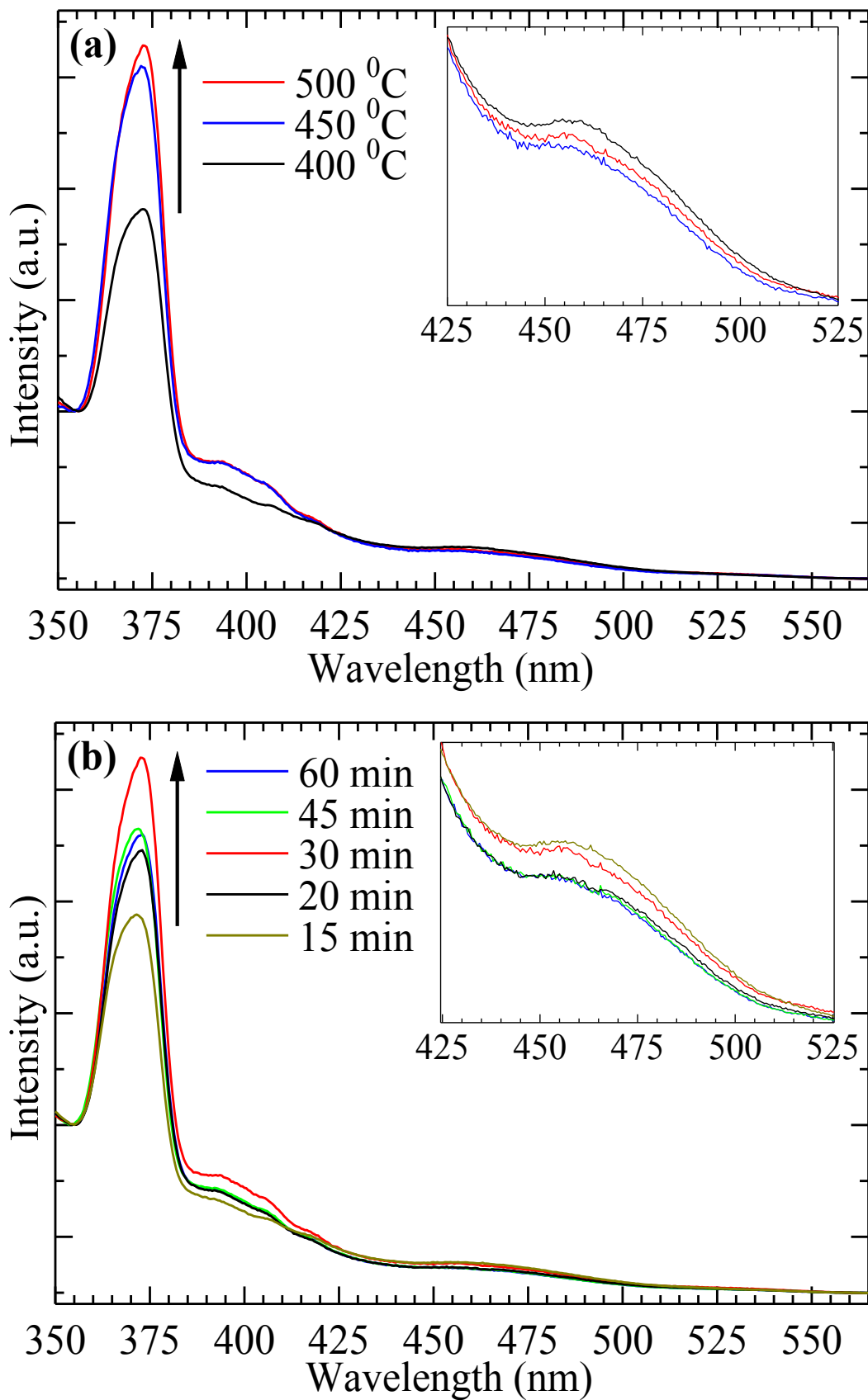
Figure 3.15: Photoluminescence spectrum of the ZnO NSs grown on FTO substrates (a) at various T_{sub} for 30 min and (b) at 500 °C for different t_{grow}.

The peaks in the UV region clearly depict the variation of intensities in which the relative intensity increases as the T_{sub} increase from 400-500 °C. Conversely, the peaks intensities are found to maintain the following order, 30, 45, 60, 20, and 15 min, in the case of various t_{grow}. It is difficult to determine the exact reason behind this variation of intensity, the higher surface area to volume ratio for ZnO NWs grown at different T_{sub} and t_{grow} might play a vital role, since the concentration of oxygen vacancy depends strongly on the surface area of the nanostructures.[9,56] The peak in the UV region called as near band edge (NBE) emission, which originated due to direct recombinations of free exciton by an exciton-exciton collision process because of 3.3 eV wide-bandgap transitions between the conduction and valence bands of ZnO NSs at RT.[57,58] The appearance of visible emission can be recognized as deep level emission, which can be ascribed to several types of defect structures in ZnO.[59] Even though the origin of visible emission in ZnO NSs is not yet clearly understood, it is generally considered as several types of structural defects and impurities (*i.e.* Zn vacancies, oxygen vacancies, oxygen interstitials, Zn interstitials, and so on) in the ZnO crystals.[59,60]

Umar *et al.*[51] reported that the crystal quality of the deposited ZnO NSs is an important factor in the appearance of a strong and sharp UV emission in the PL spectra, and hence improvement in the crystal quality may enhance the intensity of UV emission. From the PL studies performed at RT, it can be concluded that because of the presence of strong and sharp UV emission with very weak visible (blue) emission, the ZnO NSs possess very good crystallinity with less structural defects and good optical properties. This result is consistent with the TEM and XRD measurements.

3.5 CHAPTER SUMMARY

This study demonstrated the controlled growth of high crystalline ZnO NSs by the reaction of the pure metallic Zn powder with highly pure oxygen at relatively low-temperature in a vacuum chamber without using any catalysts. The size of NSs including the NWs was controlled by adjusting the T_{sub} and t_{grow}. The optimized conditions for ZnO NWs growth were observed at T_{sub} of 500 °C and with a t_{grow} of 30 min by keeping T_{cru} to 400 °C and P_{oxy} to 3.9×10^{-2} Pa. ZnO NWs continuously grow from the nuclei by further absorbing Zn atoms and reacting them with oxygen atoms. By detailed structural and compositional analysis, it was confirmed that the as-grown ZnO NWs has a good crystallinity, with hexagonal wurtzite phase. The high crystallinity, optical properties, and easily controllable morphologies of ZnO NSs, should be useful in fabricating novel devices, such as field emitters, DSC and other hybrid solar cells.

In this study, the fabricated NWs are not fully aligned, they are oriented randomly. This random orientation of ZnO NWs on the film causes high sheet resistance. In addition, random orientation of ZnO NWs has revealed NW-NW junction resistance which is the dominating factor affecting charge transport. On the contrary, aligned ZnO NWs arrays would be crucially important for solar cell application because of the high electron diffusion coefficient.[23] The aligned ZnO NWs are favorable to suppress the trap-limited diffusion for electron transport, a slow mechanism that limits electron extraction efficiency in the devices. From this point of view, the ZnO NWs grown at 500 °C for 30 min possess high-crystalline nature, singly oriented without NW-NW junction or network-like morphology compare to Ag-assisted growth of ZnO NWs. Thus, it is expected that the highly-crystalline, catalyst-free ZnO NWs would be favorable for efficient charge transport in the perovskite solar cells. Solar cell fabrication and performance measurement will be discussed in detail in a subsequent chapter.

References

[1]   Y. Li, F. Qian, J. Xiang and C. M. Lieber, Mater. Today **9**, 18-27 (2006).

[2]   L. Schmidt-Mende and J. L. MacManus-Driscoll, Mater. Today **10**, 40-48 (2007).

[3]   Z. L. Wang, J. Phys.: Condens. Matter **16**, R829-R858 (2004).

[4]   J. Tornow and K. Schwarzburg, J. Phys. Chem. C **111**, 8692-8698 (2007).

[5]   A. B. Djurisić and Y. H. Leung, Small **2**, 944-961 (2006).

[6]   D. Tsivion, M. Schvartzman, R. P. Biro and E. Joselevich, ACS Nano **6**, 6433 (2012).

[7]   S. Xu, Y. Wei, M. Kirkham, J. Liu, W. Mai, D. Davidovic, R. L. Snyder and Z. L. Wang, J. Am. Chem. Soc. **130**, 14958 (2008).

[8]   M. H. Huang, S. Mao, H. Feick, H. Yan, Y. Wu , H. Kind, E. Weber, R. Russo and P. Yang, Science **292**, 1897 (2001).

[9]   M. H. Huang, Y. Wu, H. Feick, N. Tran, E. Weber and P. Yang, Adv. Mater. **13**, 113 (2001).

[10] L. E. Greene, M. Law, D. H. Tan, M. Montano, J. Goldberger, G. Somorjai and P. Yang, Nano Lett. **5**, 1231-1236 (2005).

[11] B. Liu and H. C. Zeng, J. Am. Chem. Soc. **125**, 4430-4431 (2003).

[12] M. Guo, P. Diao and S. Cai, J. Solid State Chem. **178**, 1864-1873 (2005).

[13] B. P. Zhang, N. T. Binh, K. Wakatsuki, Y. Segawa, Y. Yamada, N. Usami, M. Kawasaki and H. Koinuma, Appl. Phys. Lett. **84**, 4098 (2004).

[14] Z. W. Pan, Z. R. Dai and Z. L. Wang, Science **291**, 1947-1949 (2001).

[15] H. Yan, R. He, J. Pham and P. Yang, Adv. Mater. **15**, 402-405 (2003).

[16] D. Pradhan, Z. Su, S. Sindhwani, J. F. Honek and K. T. Leung, J. Phys. Chem. C **115**, 18149 (2011).

[17] H. I. Abdulgafour, Z. Hassan, N. Al-Hardan and F. K. Yam, Physica B **405**, 2570 (2010).

[18] X. D. Wang , C. J. Summers and Z. L. Wang, Nano Lett. **4**, 423 (2004).

[19] S. Bai, W. Wu, Y. Qin, N. Cui, D. J. Bayerl and X. Wang, Adv. Funct. Mater. **21**, 4464 (2011).

[20] X. Y. Kong and Z. L. Wang, Nano Lett. **3**, 12 (2003).

[21] Y. Yang, J. J. Qi, W. Guo, Y. S. Gu, Y. H. Huang and Y. Zhang, Phys. Chem. Chem. Phys. **12**, 12415 (2010).

[22] S. Xu, C. Xu, Y. Liu, Y. F. Hu, R. S. Yang, Q. Yan, J. H. Ryou, H. J. Kim, Z. Lochner, S. Choi, R. Dupuis and Z. L. Wang, Adv. Mater. **22**, 4749 (2010).

[23] M. Law, L. E. Greene and J. C. Johnson, Nat. Mater. **4**, 455 (2005).

[24] L. Li, T. Zhai, Y. Bando and D. Golberg, Nano Energy **1**, 91 (2012).

[25] A. I. Hochbaum and P. Yang, Chem. Rev. **110**, 527 (2010).

[26] K. Mahmood, B. S. Swain and A. Amassian, Nanoscale **6**, 14674-14678 (2014).

[27] J. Dong, Y. Zhao, J. Shi, H. Wei, J. Xiao, X. Xu, J. Luo, J. Xu, D. Li, Y. Luo and Q. Meng, Chem. Commun. **50**, 13381-13384 (2014).

[28] F. J. Ramos, M. C. Lopez-Santos, E. Guillen, M. K. Nazeeruddin, M. Gratzel, A. R. Gonzalez-Elipe and S. Ahmad, ChemPhysChem **15**, 1148-1153 (2014).

[29] M. Aüwarter, U. S. Patent 2,920,002 (1952).

[30] D. S. Brinsmaid, W. J. Keenan, G. J. Koch and W. F. Parsons, U. S. Patent 2,784,115 (1953).

[31] L. I. Maissel and R. Glang, *Handbook of Thin Film Technology* (McGraw-Hill, 1970), pp. 11-86.

[32] W. Heitmann, Appl. Opt. **10**, 2414 (1971).

[33] Y. Miura, J. Takada, A. Osaka and T. Kawamura, Memoirs of the Faculty of Engineering,Okayama University **25**, 23-35 (1990).

[34] G. Gordillo and C. Calderón, Sol. Energy Mater. Sol. Cells **69**, 251-260 (2001).

[35] F. Mesa, G. Gordillo and C. Calderón, phys. stat. sol. (c) **1**, S88-S91 (2004).

[36] K. Yamamoto, K. Nagasawa and T. Ohmori, Physica E **24**, 129-132 (2004).

[37] M. M. Rahman, N. Hattori, Y. Nakagawa, X. Lin, S. Yagai, M. Sakai, K. Kudo and K. Yamamoto, Jpn. J. Appl. Phys. **53**, 11RE01 (2014).

[38] N. Zietteli, *Quantum mechanics: concepts and applications* (Wiley, 2001).

[39] D. C. Bell and N. Erdman, *Low Voltage Microscopy: Principles and Applications* (Wiley, 2012).

[40] M. Birkholz, *Thin Film Analysis by X-Ray Scattering* (Wiley-VCH, 2005).

[41] B. D. Cullity, *Elements of X-ray Diffractions* (Addison-Wesley, USA, 1978) 2nd ed., p. 102.

[42] A. K. Zak, W. H. A. Majid, M. E. Abrishami and R. Yousefi, Solid State Sci. **13**, 251 (2011).

[43] B. D. Cullity and S. Rstock, *Elements of X-ray Diffraction* (Prentice Hall, New Jersey, 2001).

[44] E. F. Schubert, Light-emitting Diodes (Cambridge University Press, 2006) 2nd ed.

[45] J. Q. Hua and Y. Bando, Appl. Phy. Lett. **82**, 1401 (2003).

[46]   F. Fang, D. X. Zhao, J. Y. Zhang, D. Z. Shen, Y. M. Lu, X. W. Fan, B. H. Li and X. H. Wang, Mater. Lett. **62**, 1092 (2008).

[47]   A. Kar, K. B. Low, M. Oye, M. A. Stroscio, M. Dutta, A. Nicholls and M. Meyyappan, Nanoscale Res. Lett. **2011**, 6:3 (2010).

[48]   L. Yuan, C. Wang, R. Cai, Y. Wang and G. Zhou, J. Cryst. Growth **390**, 101 (2014).

[49]   Z. Zhang, Y. Liu, D. Liu, S. Luo, J. Shen, L. Liu, W. Ma, Y. Ren, Y. Xiang, W. Zhou and S. Xie, Appl. Phys. Lett. **91**, 013106 (2007).

[50]   Z. Zhang, S. J. Wang, T. Yu and T. Wu, J. Phys. Chem. C **111**, 17500-17505 (2007).

[51]   A. Umar, C. Ribeiro, A. Al-Hajry, Y. Masuda and Y. B. Hahn, J. Phys. Chem. C **113**, 14715-14720 (2009).

[52]   H. Kim, J. Y. Moon and H. S. Lee, Electron. Mater. Lett. **7**, 59-62 (2011).

[53]   Q. Cheng and K. K. Ostrikov, CrystEngComm. **13**, 3455-3461 (2011).

[54]   A. Umar and Y. B. Hahn, Cryst. Growth Des. **8**, 2741-2747 (2008).

[55]   A. Janotti and C. G. Van de Walle, Phys. Rev. B **76**, 165202 (2007).

[56]   S. Sun, G. Meng, G. Zhang and L. Zhang, Cryst. Growth Des. **7**, 1988-1991 (2007).

[57]   Y. K. Tseng, C. J. Huang, H. M. Cheng, I. N. Lin, K. S. Liu and I. C. Chen, Adv. Funct. Mater. **13**, 811-814 (2003).

[58]   S. C. Lyu, Y. Zhang, H. Ruh, H. J. Lee, H. W. Shim, E. K. Suh and C. J. Lee, Chem. Phys. Lett. **363**, 134-138 (2002).

[59]   L. Li, K. Yu, Y. Wang and Z. Zhu, Appl. Surf. Sci. **256**, 3361-3364 (2010).

[60]   D. M. Bagnall, Y. F. Chen, M. Y. Shen, Z. Zhu, T. Goto and T. Yao, J. Cryst. Growth **184**, 605-609 (1998).

CHAPTER FOUR

Organic-Inorganic Perovskite Solar Cells based

on Zinc Oxide Nanowires

The increasing use of fossil fuel resources and the effects of CO_2 discharges on the climate are the main propulsive forces for the research of renewable energies. The sources of the renewable energies include mainly the sunlight, wind, rain, tides, and geothermal heat. Among these, the sun is the largest energy sources. The sunshine provides energy in an hour is about 3.8×10^{23} kW h^{-1}, which is enough to satisfy the highest energy demand of human for a year (1.6×10^{10} kW in 2005).[1] Solar energy is considered as a carbon-free energy which can be converted directly into electricity through the solar cell devices. There are several kinds of photovoltaic devices in which organic-inorganic perovskite solar cells have garnered great attention nowadays for their low-cost, simple preparation and high performance. In order to fabricate perovskite solar cells, the synthesized *n*-type ZnO NWs as an electron-transfer layer have been employed. In this chapter, the synthesis and characterization of organic-inorganic perovskite materials and their application to the solar cells have been presented. The filtration effects of lead iodide (PbI_2) solution on perovskite solar cell performances are described. Perovskite materials and device stability are summarized in this chapter.

4.1 ORGANIC-INORGANIC PEROVSKITE SOLAR CELLS

Recently, organic-inorganic perovskite solar cells have drawn enormous attention because of their promising material which is eligible of constructing high-efficiency next-generation photovoltaic devices at a comparatively low fabrication cost.[2-8] Organic-inorganic halide perovskite as a light absorber,[9-11] is emerging because of the simple solution processability and excellent electrical and optical properties which are efficient for perovskite solar cells. Among the family of organic-inorganic halide based perovskites, $CH_3NH_3PbI_3$ has been used frequently as light absorbing material for perovskite solar cells.[12-14] Perovskite solar cells based on $CH_3NH_3PbI_3$ have been widely explored due to

its high-absorption coefficient over a broad region of the visible spectrum,[15-16] long electron-hole diffusion lengths,[17,18] and excellent charge-carrier mobility,[15,19] leads to better performance of the solar cells.

Although perovskite was discovered a few decades ago, Miyasaka and co-workers was the pioneer who employed perovskites of $CH_3NH_3PbI_3$ and $CH_3NH_3PbBr_3$ as sensitizers on the nanoporous TiO_2 in the liquid electrolyte-based DSC and measured the PCE of 3.81% and 3.13%, respectively.[20] However, the stability of the devices was not satisfactory because of the dissolution of perovskite in the electrolyte. In 2011, Park *et al.*, prepared quantum-dot-sensitized solar cell using $CH_3NH_3PbI_3$ nanocrystals (*ca.* 2-3 nm in diameter) on nanocrystalline TiO_2 and improved PCE of 6.54% was achieved.[21] However, the solar cells were also extremely susceptible to dissolution within redox electrolyte solution. The PCE and stability of the perovskite solar cells were significantly improved by substituting liquid electrolyte with the solid hole transporting material (HTM), for instance 2, 2´, 7, 7´-tetrakis (*N,N*-di-*p*-methoxyphenylamine)-9,9´-spirobifluorene (*Spiro*-MeOTAD) to escape from the dissolution of perovskite.[6,9-11,22-26] Just as HTM, the *Spiro*-MeOTAD not only enhanced the stability, as anticipated, it also improved the PCE to 9.7%.[27] In the same year, Snaith *et al.*, demonstrated the PCE of 10.9% by substituting the mesoporous *n*-type TiO_2 with an inert Al_2O_3 scaffold.[28] One year later, Grätzel *et al.*, introduced a two-step sequential deposition process which displayed a homogeneous morphology and a high PCE of 15% because of the betterment of TiO_2 pore-filling.[29] Zhou *et al.* demonstrated that the planar perovskite solar cells with an improved PCE of around 19.3% was achieved through the effective interface-engineering technology.[30] Meanwhile, numerous studies reported that the PCE over 20% can be achieved in the future through the optimization of perovskite solar cells.[4,9,11,25,26,31,32]

Numerous endeavors are presently being guided in improving the efficiency of perovskite solar cells, which have been employed commonly a mesoporous TiO_2 as charge collecting layer, upon which $CH_3NH_3PbI_3$ light absorber can be grown. However, current study reported that the TiO_2 has low intrinsic electron mobility which leads to the unbalanced charge transport in solar cells [33] and, therefore, many scientists became interested in studying the perovskite solar cell performance of substitute semiconducting materials. ZnO is believed to be a superior alternative to TiO_2 because of higher electron mobility [34,35] than the mobility [36] of TiO_2. In addition, ZnO has an identical conduction band edge, which is suitable for efficient electron injection from the light absorbing materials. The NWs have an upward band-bending at the surface which confines the injected electrons within the wire cores.[34] Moreover, the NWs morphology allows the electrons to move easily due to the direct conduction paths from the point of injections to the point of collections. The excellent electron transport within the NWs can be ascribed to its superb crystallinity and the existence of internal electric-fields which promotes electron transport to the collecting electrode. Note that above mentioned unique properties of ZnO NWs depend strongly on their morphology, dimension, structure and crystallinity of NWs.[37] Although the NWs morphologies have many befits, there are also some critical demerits compared with the closely compact NPs thin film. In the case of vertically aligned NWs morphology, there may exist the uncovered substrate-surfaces or open spaces between NWs, resulting in the direct contacts with the oxide substrates which lead to electron recombination or electron back transfer during the charge transport process. Therefore, controlled synthesis of ZnO nanostructures, especially NWs under mild conditions is one of the most important issues nowadays.

In this dissertation, I report on the RE growth of ZnO NWs which has been discussed in detail by the previous chapter 3, and its successful application as charge transporting layer (CTL) in solution-processed organic-inorganic perovskite solar cell. The morphology of the $CH_3NH_3PbI_3$ film was investigated in detail through the observation of filtration effect of PbI_2 solution and found to influence the device performance. Spin coating of filtered PbI_2-solution assists to form the better crystal and comparably homogenous coverage of the $CH_3NH_3PbI_3$ films, resulting in an improvement of the solar cell efficiency compared with the cells prepared by using non-filtered PbI_2-solution. By fabricating the $CH_3NH_3PbI_3$ films using filtered PbI_2-solution, we achieved perovskite solar cells with the best PCE of 4.8%.[38]

4.2 DEVICE FABRICATION PROCEDURES

The preparation of perovskite solar cells is usually involved in several steps, for instance the substrate cleaning and surface treatment followed by various coating and deposition procedures as shown in Fig. 4.1. Here, a common recipe used to fabricate the perovskite solar cells is presented in the following sections.
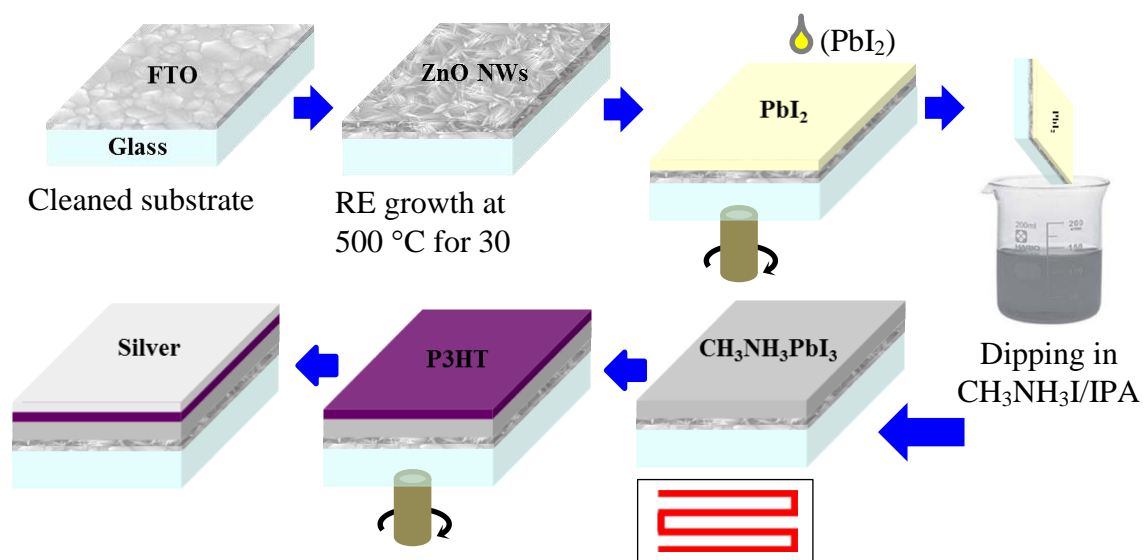
Figure 4.1: Schematic illustration of several steps to fabricate the perovskite solar cells

4.2.1 Substrate preparation

The substrate used in this thesis is typically the standard glass substrate coated with a transparent conductive oxide (TCO), such as FTO. The FTO glass substrate was chosen because of its superior stability at high temperatures. Since the growth of ZnO NWs required moderately high temperature around 500 °C. Furthermore, the FTO has a lower sheet resistance, high surface roughness with higher optical transmittance. As a consequence, the low-iron 2.2 mm thick, TCO 22-7 glass substrate (Solaronix S.A, resistance 7 Ω/sq, transmittance higher than 70% from 470 to 1100 nm of wavelength) has been used for device fabrication. Substrate-cleaning is supposed to be a crucial process that influences the solar cell performance and, therefore, the FTO substrates have been cleaned efficiently prior to the device fabrication. Several cleaning steps were conducted by using semicoclean 23, deionized water, and organic solvent. Firstly, the substrate was cleaned by ultra-sonication in semicoclean 23 (Furuuchi Chemical, Semicoclean 23) for 10 min and this process was done again two times. The substrate was further cleaned by sonication in deionized water for 5 min. This process was repeated for four cycles. Subsequently, the substrate was sonicated twice in acetone for 10 min. The same process was applied for 2-propanol. Finally, a dry nitrogen flow was used to remove the residual solvents.

4.2.2 Growth of ZnO nanowires

ZnO NSs were grown based on the RE method described in the previous chapter 3. The RE method is very simple, easy controllable, low-cost non-toxic, and catalyst-free. Although manifold morphologies of ZnO NSs can be grown by varying T_{sub}, t_{grow}, P_{oxy} in the vacuum chamber and metal seeded-layer over the FTO substrate, the ZnO NWs were considered for fabrication of perovskite solar cells. The typical diameter and length of the

ZnO NWs grown at T_{sub} of 500 for 30 min were around 46 nm and 310 nm, respectively. The fabricated NWs were used as CTL of perovskite solar cells because of the high-density morphology and high crystallinity of NWs as discussed in the previous chapter. CTL is an important part of perovskite solar cells because the CTL as oxide semiconductor has band alignments which support the electron transfer and block the holes appearing from photogeneration at the same time. After ZnO NWs growth, $CH_3NH_3PbI_3$ was deposited using a two-step deposition method in the ZnO NWs films.

4.2.3 Synthesis of methylammonium iodide

CH_3NH_3I was synthesized according to the reported procedures with some alterations.[28,39] The steps of growth of CH_3NH_3I crystal are shown in Fig. 4.2.
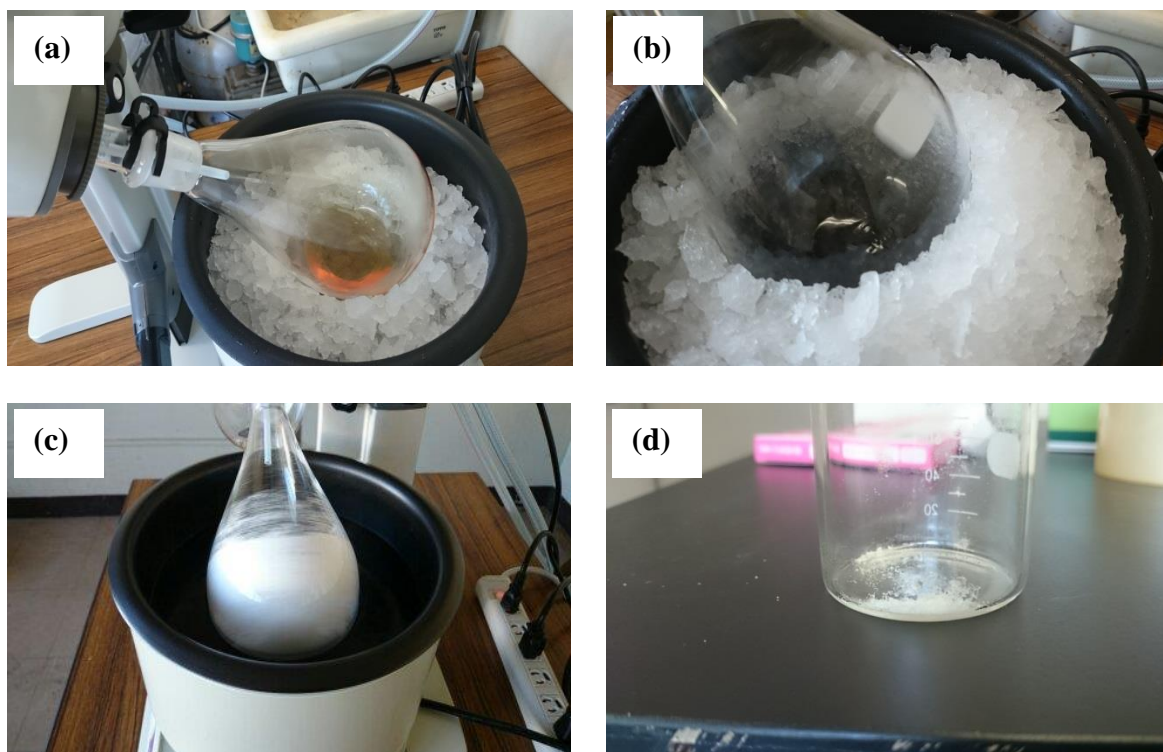
Figure 4.2: (a) Equimolar mixer of CH_3NH_2 and HI, (b) Stirring at 0 °C, (c) Precipitant (CH_3NH_3I) recovered at 60 °C and (d) Crystalline CH_3NH_3I washed with diethyl ether.

Typically, 0.273 mol (27.86 mL) methylamine (CH_3NH_2) solution (40% in methanol, Tokyo Chemical Industries) was reacted with the 0.227 mol (30mL) hydroiodic acid (HI) (57wt % in water, Tokyo Chemical Industries) with stirring at 0 °C for about 2 h, in an ice bath in order to synthesize the CH_3NH_3I. After stirring around 2 h at 0 °C, the precipitate was recovered by using a rotary evaporator at 60 °C for 1 h. The product, CH_3NH_3I crystals was obtained and washed by diethyl ether through stirring the solution for 30 min. This process was repeated for three times to achieve the white colored crystals. Finally, the CH_3NH_3I crystals were dehydrated overnight at 60 °C under dark environment.

4.2.4 Deposition of methylammonium lead triiodide

The $CH_3NH_3PbI_3$ perovskite layers were formed by means of two-step deposition method in order to obtain good coverage of the films and crystal structure compared with one-step spin-coating process, as stated in the literatures.[21,29,40] The lead iodide (PbI_2, Sigma-Aldrich) was dissolved in anhydrous N, N-dimethylformamide (DMF, Wako) at a concentration of 460 mg mL^{-1} overnight under stirring at RT, and subsequently filtered through the 0.20 μm pore poly(vinylidene difluoride) (PVDF) syringe filter (Whatman). The filtered PbI_2-solution was spin-coated on ZnO NWs at 2000 rpm for 15 s, followed by drying in the natural air for few min. For comparative analyses, PbI_2-solution without performing filtration was prepared for *in situ* growth of $CH_3NH_3PbI_3$ on ZnO NWs. Afterwards, the FTO/ZnO NWs/PbI_2 samples were immersed into a solution of CH_3NH_3I in 2-propanol at a concentration of 10 mg mL^{-1} for 60 s. The samples were subsequently left to dry in the air at RT. The color of the samples was changed rapidly from yellow to dark-brown, revealing successful growth of $CH_3NH_3PbI_3$ layers as shown in Fig.4.3. The FTO/ZnO NWs/ $CH_3NH_3PbI_3$ samples were subsequently heated at 100 °C for 90 min under dark environment.
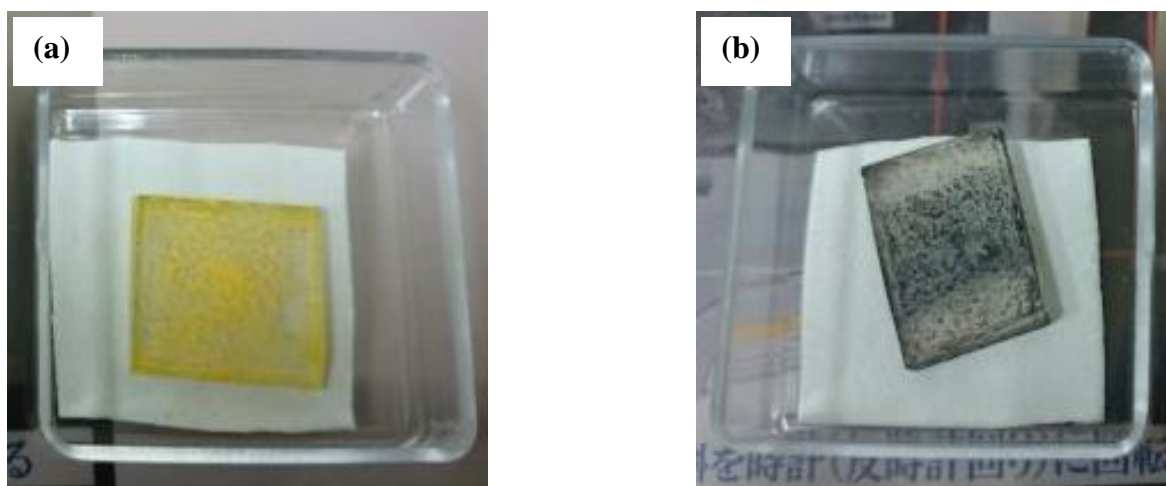
Figure 4.3: FTO/ZnO NWs/PbI$_2$ sample (a) prior to dipping and (b) after dipping into the solution of CH$_3$NH$_3$I in 2-propanol.

4.2.5 Deposition of the P3HT

In perovskite solar cells, a solid HTM is crucial since the liquid electrolyte could dissolve the perovskite light absorber. Therefore, studies of HTM itself are of interest for a large part of the solar cell community. Since the hole transporting layer (HTL) is deposited normally prior to the counter electrode, it refrain the direct contact of metal electrode with the ZnO NWs/ perovskites layer and, therefore, the selectivity of contact can be increased. Furthermore, the use of HTL in perovskite solar cells can reduce the recombination, which was evidenced by an increase of open-circuit voltage (V_{OC}) and higher luminescence efficiency.[41] The HTL thickness around 200 nm is not only surpluses the charge carrier collection efficiency, but also the light harvesting efficiency.[42] The short-circuit current density (J_{SC}) of the devices strongly depends on the thickness of HTL and it increases with an increasing of HTL thickness as shown in Fig. 4.4. This can be attributed to the enhancement of reflectivity of a smooth HTL/ counter electrode interface. However, the HTL thickness higher than 400 nm is essential for rough CH$_3$NH$_3$PbI$_3$ perovskite surface in order to avoid the recombination which results in a high V_{OC}.
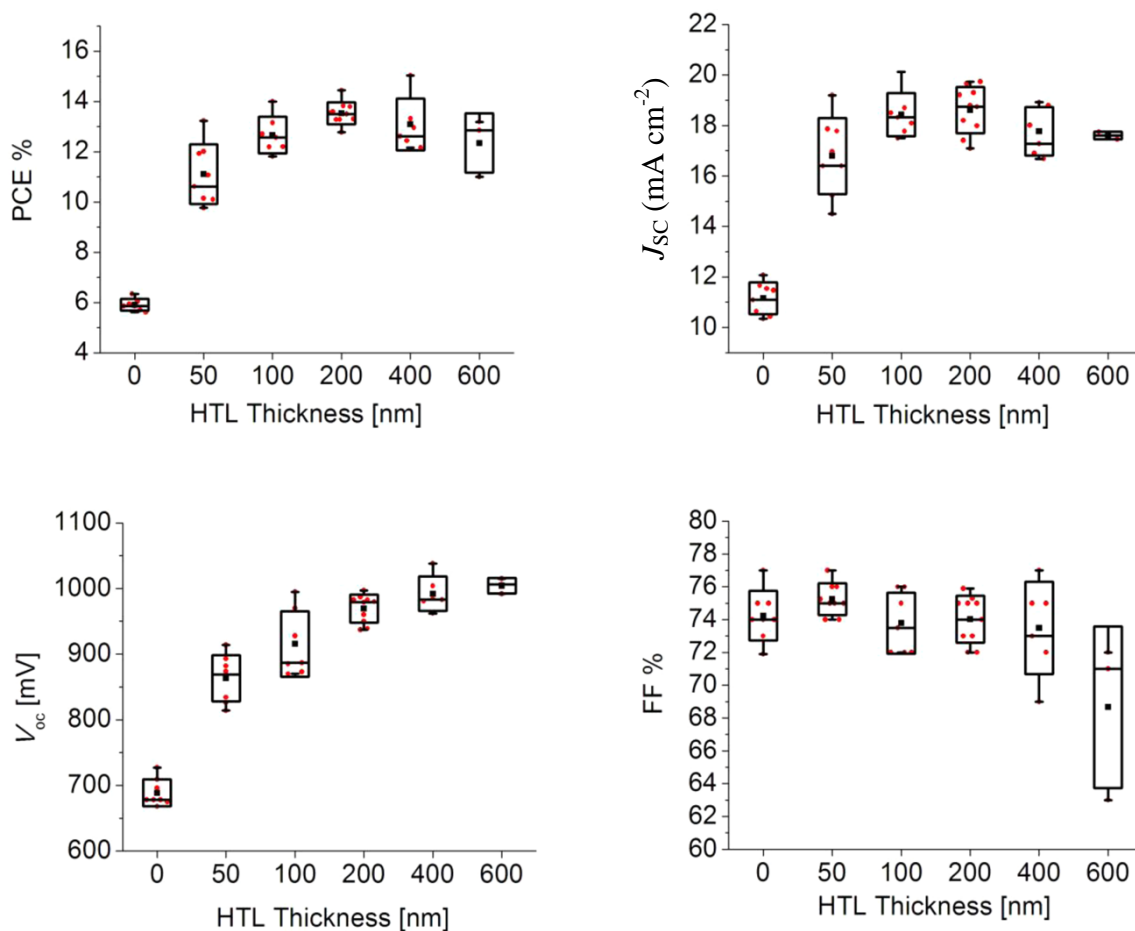
Figure 4.4: Effect of HTL thickness on PCE, J_{SC}, V_{OC}, and *FF*. Box represents the standard deviation, whiskers minimum and maximum values. Reprint with permission from ref.[42] Copyright 2015, American Chemical Society.

Meanwhile, a large variety of inorganic and organic solid HTM used in perovskite solar cells are studied. The most commonly used HTM is 2,2′,7,7′-tetrakis-(N,N-di-p-methoxyphenylamine)9,9′-spirobifluorene (Spiro-OMeTAD),[43] which exhibits excellent charge transport, low rates of recombination and good pore filling. Besides, P3HT shows relatively high hole mobility,[44-46] and good stability. P3HT has been used as a lower-priced HTM substitute to Spiro-OMeTAD for efficient perovskite based solar cells.[47] Moreover, it can be deposited by using various types of coating techniques,[48] for instance, spin coating, inkjet printing, spray-coating and so on. As for HTL, I used P3HT (Sigma-Aldrich) which was deposited by means of spin-coating technique under the ambient air

conditions. Prior to the deposition, the P3HT was dissolved in chlorobenzene (Wako) at a concentration of 15 mg mL^{-1} followed by stirring. Finally, a layer of P3HT was prepared through spin-coating process at 1500 rpm for 120 s in the air.

4.2.6 Deposition of counter electrode

The counter electrode of perovskite solar cells is usually obtained by thermal evaporation of a noble metal with a high work function, such as Ag. As a counter electrode, Ag is considered because of less expensive material, higher conductivity and Ag has demonstrated to yield excellent short-circuit photocurrent (I_{SC}).[49] Furthermore, Ag has higher reflection capabilities that are especially advantageous for metal-oxide thin films in which the incident light is not completely absorbed. Noted that the steps prior to Ag deposition are somewhat different and it depends on the kind of HTM coated on the substrate. For example, in the case of Spiro-OMeTAD, it is necessary to expose in the atmosphere for several hours because of doping and enhancing its conductivity. However, no preparative procedures are essential for P3HT. Finally, around 120 nm thick top Ag electrode was evaporated thermally under the high vacuum of 7×10^{-4} Pa., at a rate of ~ 0.1 nm s^{-1} to complete the solar cells. Around 100 nm thick of Ag was evaporated firstly, at low deposition rates of 0.03 - 0.05 nm s^{-1} due to prevent the damage of the devices.

The device configuration (FTO/ZnO NWs/CH$_3$NH$_3$PbI$_3$/P3HT/Ag) and a schematic energy-level diagram of the component materials used in perovskite solar cells are displayed in Fig. 4.5(a) and (b), respectively. The growth of CH$_3$NH$_3$PbI$_3$ perovskite layers and devices fabrication, as presented herein, are executed under ambient conditions, leaving out the ZnO NWs growth and deposition of Ag counter electrode. Solar cell's active area was kept at 0.785 cm^2 and the rest of the area of the device was masked by using an icros tape (Mitsui Chemicals ICROS^{TM} Tape) during fabrication.
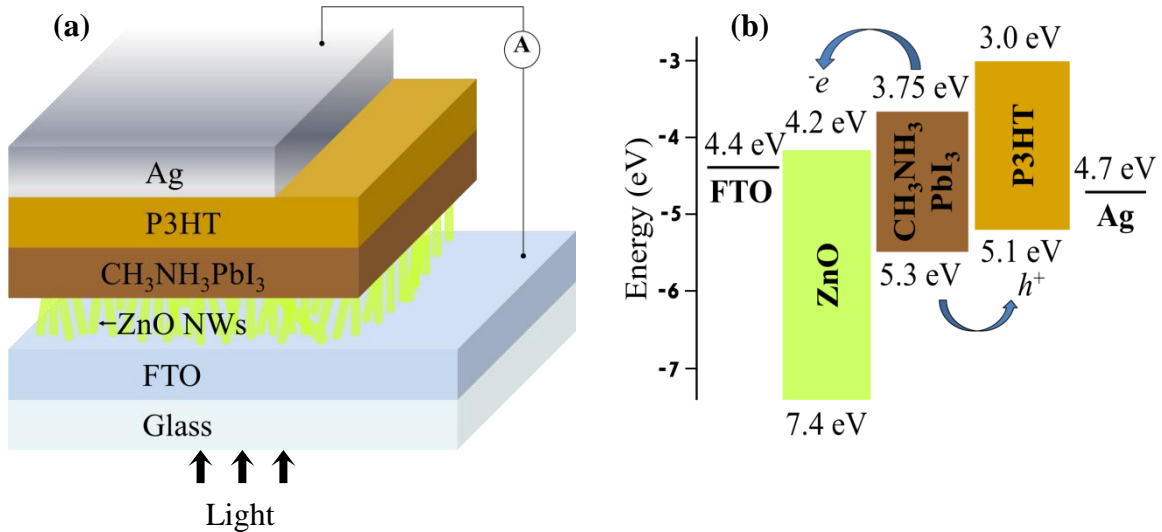
Figure 4.5: (a) Schematic diagram of the ZnO NWs based perovskite solar cell and (b) energy-level diagram of the component materials. Reprint with permission from ref.[38] Copyright 2015, Japan Society of Applied Physics.

4.3 CHARACTERIZATIONS AND MEASUREMENTS

The morphological and micro-structural characterizations were performed by using FE-SEM (JEOL JSM-6340F) and high-resolution TEM (Hitachi H-7650). Structural and phase characterizations of the ZnO NSs were carried out by XRD. The patterns of XRD were recorded *via* the Bruker AXS (D8 ADVANCE) X-ray diffractometer equipped with Cu Kα ($\lambda = 1.54056$ Å) source. UV-vis absorption spectra were obtained through the UV-vis-NIR, scanning spectrophotometer (Shimadzu UV-3100 PC) which was consisted of an integrating sphere. The measurements were done at RT where the incident beam-angle was set to 0°. The current density-voltage (*J-V*) characteristics of solar cells were determined through the Keithley 2100 unit in the dark and under an illumination of the 100 mW cm^{-2} AM1.5G spectrum by using a xenon-lamp based solar simulator (Oriel LCS-100). The measurements were performed by using a metallic shadow-mask due to outline the active area of the device and avoid any edge effects for a small-area based solar cell.

4.3.1 Characterization techniques

The common techniques of characterizations of perovskite films and devices are FE-SEM, TEM, EDX, XRD and PL which have been discussed in previous chapter 3. Additionally, UV-vis-NIR spectroscopy and Current-Voltage measurement also employed for characterization of perovskite solar cells are introduced in this section.

4.3.1.1 UV-vis-NIR spectroscopy

A UV-vis-NIR spectrophotometer can exactly measure the transmittance and reflectance spectra over a broad range of wavelengths, for instance, near-infrared to the ultraviolet region. In most cases, the absorption is not directly measured. It is calculated from the transmittance and reflectance measurements with appropriate corrections. The absorption in a perovskite layer is measured with regard to optical density. To measure the UV-vis-NIR absorption characteristics, the sample is exposed to light and the wavelengths are scanned using a monochromator from the visible to near infrared. The detector measures the ratio of transmitting light through the sample and the incident on the sample with respect to each wavelength. Once the light intensity that passes through the sample is known, the transmittance, T can be calculated according to the equation 4.1.

$$T = \frac{I_1}{I_0}$$
(4.1)

where I_1 is the light intensity after passing through the sample and I_0 is also the light intensity before passing through the sample. The T can be used to calculate the absorption, A according to the equation 4.2.

$$A = -\log_{10}(T) = -\log_{10}\left(\frac{I_1}{I_0}\right)$$
(4.2)

where A stands for the amount of photons that are absorbed.

Typically, the major ingredients of the UV-vis-NIR spectrophotometer are a source of light; double beams used for reference and sample, monochromator, a detector and a recording device as illustrated in Fig. 4.6 (a).
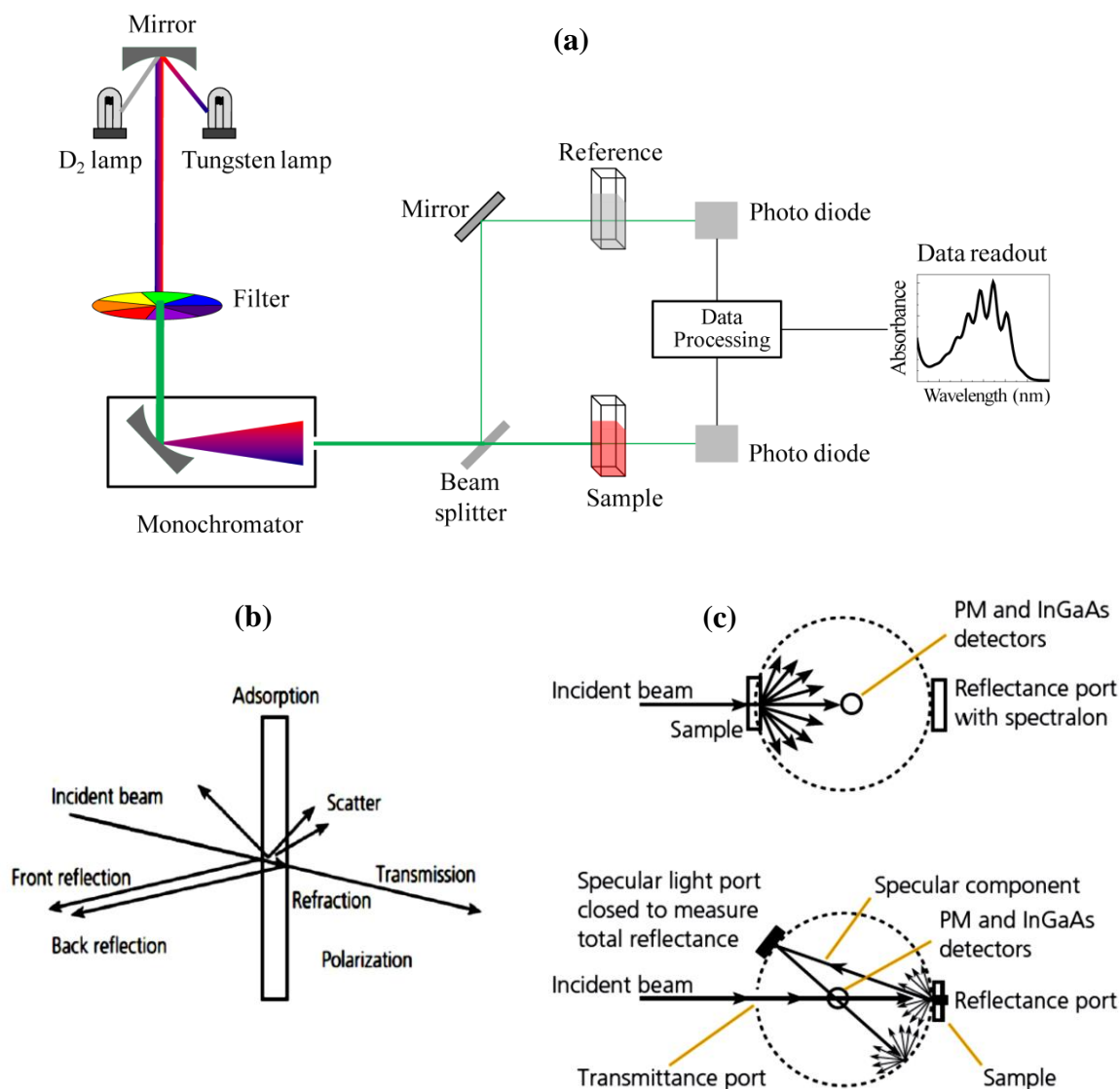
Figure 4.6: (a) Schematic of UV-vis spectrophotometer,[50] (b) interactions of light with a solid and (c) measurements with an integrating sphere: transmission (upper) and reflection (lower).[51]

The lights of sources are commonly a tungsten filament-lamp and deuterium discharge-lamp applied to measure the visible and UV region, respectively. The light comes after the sources are in two beams for the reference and sample. The ratio of the beam intensity

between reference and sample are recorded by the spectrometer. The recorder plots the absorbance with respect to wavelength. In the case of solid sample, when the beam of light comes into contact, it may be reflected, transmitted, diffused, absorbed, refracted or polarized as illustrated in Fig. 4.6 (b). In order to perform a correct transmittance measurement, such as direct transmittance, diffuse transmittance for a solid sample, particular equipment named as an integrating sphere is necessary as shown in Fig. 4.6 (c). As with the case of transmittance measurement, an integrating sphere is essential to measure the specular and diffuse or overall reflectance, R. The percentage of absorption spectra can be obtained by %A $(\lambda) = 100\%$ - %T (λ) - %R (λ).[52,53]

4.3.1.2 Current-Voltage measurement

The current-voltage is measured to evaluate the performance of a solar cell. The measurements of J-V characteristics are performed both in the dark and under illumination through an external potential bias to the cell as long as the response of current is measured. An ideal perovskite solar cell exhibits usual diode behavior in dark condition is presented in Fig 4.7 (a). At low applied voltage, extremely little or no current flows through the device because of low conductivity of the metal-oxide, resulting from a small charge density. However, the charge density increases with increasing applied voltage and enhances the quasi-Fermi level in metal-oxide. When the quasi-Fermi level advances the conduction band, the dark current improves steeply because of easily electrons flow to the HTM. Note that under dark condition, the electrons are injected inside the metal-oxide and recombines with holes in the HTM. Thus, dark current is controlled by the recombination process which leads the damage of photogenerated charge carriers in illumination.

Under illumination, the solar cells operate as a source of current and the photocurrent flows opposite to diode current. Figure 4.7 (b) shows a typical J-V curve, which has been

measured under illumination. The shapes of J-V curve strongly depend on photocurrent generation and electron-hole recombination. At low forward bias, one can observe that most of the charge carriers are collected prior to recombination. When the applied bias is increased, the recombination becomes dominant that leads the losses of photogenerated charge carriers, finally. Under this situation, the *J-V* begins to decline until it arrived at the point, where no current is flowing. This restricted point is named as the V_{OC}. Besides, the point where the external bias applied to the solar cell is zero denoted as the J_{SC}.
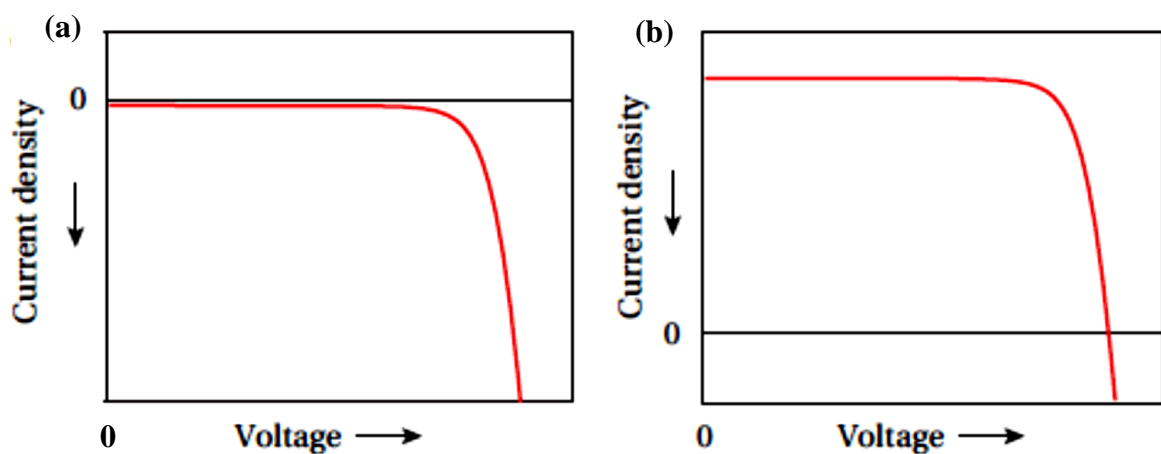
Figure 4.7: A typical *J-V* curve of a solar cell measured (a) in the dark condition, (b) under illumination.

By using *J-V* characteristics, several other important parameters, such as PCE, maximum power point (*MPP*), current at maximum power point (J_{MP}), voltage at maximum power point (V_{MP}) and fill factor (*FF*) can be obtained to evaluate the performance of solar cells as shown in Fig. 4.8. The *FF* represents the 'green squareness' of the *J-V* curve. The *FF* is the ratio between the product of J_{MP} and V_{MP}, and J_{SC} and V_{OC} can be depicted according to equation 4.3.

$$FF = \frac{V_{MP}.\,J_{MP}}{V_{OC}.\,J_{SC}} \tag{4.3}$$

Through the *FF*, the maximum power output of the solar cell can be written in accordance with equation 4.3.

$$P_{MAX} = V_{OC}. J_{SC}. FF \tag{4.4}$$

Lastly, the power conversion efficiency is determined as the power produced by the cell (P_{MAX}) divided by the power incident on the representative area of the cell (P_{light}).

$$PCE = \frac{P_{MAX}}{P_{light}} = \frac{V_{OC}. J_{SC}. FF}{P_{light}} \tag{4.5}$$
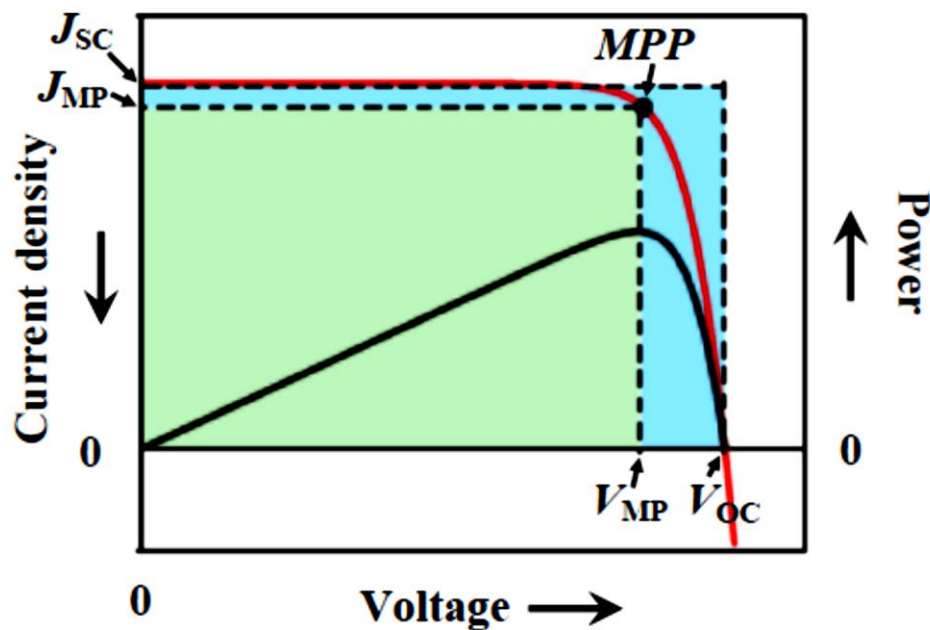
Figure 4.8: A typical *J-V* curve of a solar cell measured under illumination and the corresponding power curve (right-hand axis, black curve). The black dot on the *J-V* curve marks the point where the electrical power output is maximized.

The *PCE* of solar cell is deeply moved on the resistances. For estimation of the resistance losses, the series resistance, R_S and parallel resistance, R_P can be added to the equivalent circuit of the solar cell. Figure 4.9 (a) represents the equivalent circuit with the R_S and R_P. Basically, R_S is related to the charge transfer processes at the connections built to the solar cell and/or the sheet resistance of the substrate. Furthermore, the R_S is affected

by the charge transport of HTM, in case of the perovskite solar cell. Besides, the R_P emerges from the loss-processes in the solar cell, governing to the leakage current. The leakage current arises because of the flawed layer of metal oxide, which causes contact in the midst of TCO and the HTM. The consequence of R_S and R_P on the *J-V* characteristics is schematically displayed in Fig. 4.9 (b), and (c). As is apparent from the figure, the *FF* of the solar cell decrease with increasing R_S or a decrease in R_P.
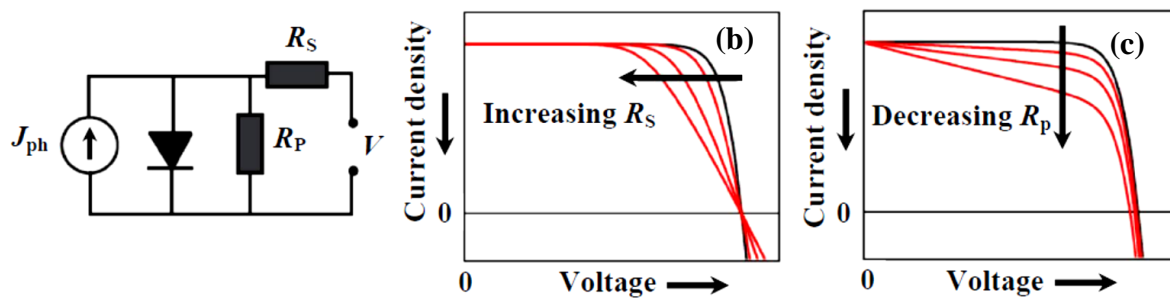
Figure 4.9: (a) Equivalent circuit based on *J-V* characteristics of a solar cell, (b) effect of an increase in R_S and (c) a decrease in R_P.

4.3.1.3 Quantum efficiency measurement

The quantum efficiency (*QE*) of solar cell is measured as a function of wavelengths. It is shown as the ratio of incident photons to converted electrons that reach the external circuit. Ideally, the *QE* has a square type pattern in which the *QE* value is somewhat constant over the entire wavelengths measured. However, in most cases, the *QE* is made smaller because of recombination effects, in which the charge carriers cannot reach into the external circuit. There are two types of *QE*: the external quantum efficiency (*EQE*), and internal quantum efficiency (*IQE*). The *EQE* is also mentioned as incident monochromatic photon-to-electron conversion efficiency (*IPCE*), taking into account all incident photons that are emitted from a solar simulator strike the active cell area. The *IPCE* can be estimated from the known photon flux, J_0 of the solar simulator according to equation 4.6.

$$IPCE\ (\lambda) = \frac{J_{SC}(\lambda)}{eJ_0} \tag{4.6}$$

where $J_{SC}\ (\lambda)$ is the short-circuit photocurrent density under monochromatic irradiation and e is the elementary charge. The *IPCE* can also be calculated according to equation 4.7.

$$IPCE\ (\lambda) = LHE\ (\lambda)\ \times\ \eta_{inj}(\lambda)\ \times\ \eta_{coll}(\lambda) \tag{4.7}$$

where *LHE* is the efficiency of light harvesting, η_{inj} is the efficiency of electron injection and η_{coll} refers as charge collection efficiency. The *LHE* is similar to absorptance which is simply obtainable through the measurement of absorption spectrum of the solar cell. The *IQE* is obtained by dividing the *IPCE* number by the *LHE*. It is also referred as absorbed photon-to-electron conversion efficiency (APCE) (*i.e.,* only photons are absorbed by the cell).

4.4 RESULTS AND DISCUSSIONS

4.4.1 Comparison between filtered and non-filtered PbI$_2$ solution deposition

The CH$_3$NH$_3$PbI$_3$ film used to fabricate the perovskite solar cell were prepared by using two-step deposition process on FTO/ZnO NWs samples. As noted, the PCE of perovskite solar cell is determined by the morphology of CH$_3$NH$_3$PbI$_3$ film and its crystalline nature, which in turn are partly dependent on the PbI$_2$ solution and subsequent treatments performed. I therefore employed the filtered and non-filtered PbI$_2$ solution to prepare the CH$_3$NH$_3$PbI$_3$ film on FTO/ZnO NWs substrates. It is crucial to determine whether the filtration and non-filtration of PbI$_2$ solution would have any effects on the CH$_3$NH$_3$PbI$_3$ structure, morphology, or the performance of the resultant solar cells. The SEM images show the results of the PbI$_2$ film deposited by spin-coating as shown in Fig. 4.10, and the samples were prepared outside the glove box under ambient air conditions.
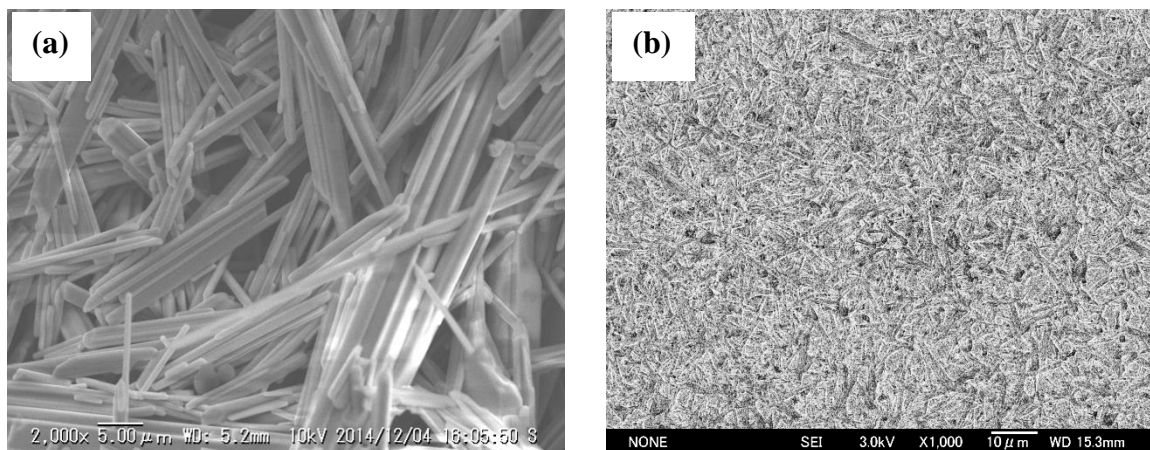
Figure 4.10: FE-SEM images of the PbI$_2$ film deposited on FTO/ZnO NWs substrates using (a) non-filtered PbI$_2$ and (b) filtered PbI$_2$ solution.

In the case of non-filtered PbI$_2$ solution, the rod-like structures and voids were observed. The length and diameter of these structures are apparently a few tens μm and 2 μm, respectively. The rod-like structures can be attributed to the PbI$_2$ crystals, which may grow somewhat due to the phase transformation of the large sized PbI$_2$ nanoparticles. As the PbI$_2$ solution is filtered, there is a drastic change in the appearance of the PbI$_2$ film formed. No rod-like structures and voids were observed. The morphology of PbI$_2$ film is relatively smooth and uniform. Hence, Fig. 4.10 clearly depicts that the morphology of the PbI$_2$ film formed is significantly influenced by the filtration effects.

4.4.2 Filtration effect of PbI$_2$ solution on solar cell performance

4.4.2.1 Observation of CH$_3$NH$_3$PbI$_3$ perovskite morphology

As is evident from the Fig. 4.10 of the previous section, the filtration of PbI$_2$ solutions influence the growth of PbI$_2$ films, subsequently, which in turn led to the formation of morphology and structure of CH$_3$NH$_3$PbI$_3$ films. Indeed, the surface morphology of CH$_3$NH$_3$PbI$_3$ films significantly varied between the filtered and non-filtered PbI$_2$-solution.

The morphology of the $CH_3NH_3PbI_3$ films were analyzed by using FE-SEM, and the corresponding results are illustrated in Fig. 4.11.
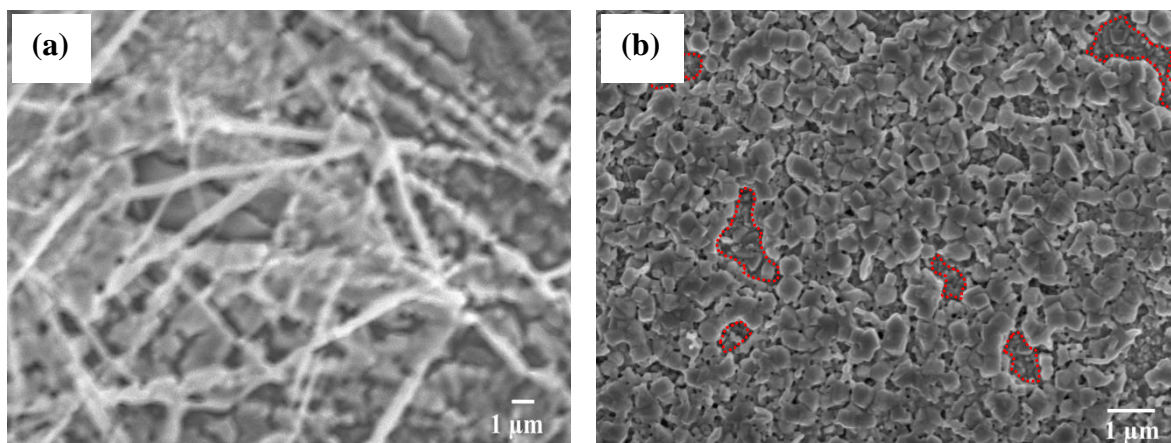
Figure 4.11: Top view of FE-SEM images of $CH_3NH_3PbI_3$ film prepared on ZnO NWs layer by using (a) non-filtered and (b) filtered PbI_2-solution. Reprint with permission from ref.[38] Copyright 2015, Japan Society of Applied Physics.

The $CH_3NH_3PbI_3$ film prepared by using non-filtered PbI_2-solution shows the fiber-like structures over the non-uniform layers of perovskite, resulting in a poor surface coverage, as shown in Fig. 4.11 (a). By observing the FE-SEM images of PbI_2 layer prepared from non-filtered PbI_2-solution, which consists of few tens μm thick rod-like structures (Fig 4.10(a)), It can be assume that the fiber-like structures shown in Fig 4.11 (a) are mainly unreacted PbI_2 that remains on the surface. In contrast, the $CH_3NH_3PbI_3$ films prepared on ZnO NWs layer using filtered PbI_2-solution exhibit relatively homogeneous domains in which the cube-like crystals are formed as shown in Fig. 4.11(b). Apparently, the size of the $CH_3NH_3PbI_3$ crystals is around 400 nm. Perovskite crystallites with a large grain size are favorable for charge transport,[54] because the carriers would need to across the smallest number of grain boundaries before collections. Moreover, there is a correlation between mobility and grain size, so that the mobility increases with increasing the grain size.[55] Furthermore, the perovskite crystals with large grain size act

also as light scattering centers of the incident light,[31] and therefore preferable for the development of high efficiency solar cell.

4.4.2.2 X-ray diffraction analysis

An XRD spectroscopy was used to investigate the crystallites structure of the $CH_3NH_3PbI_3$ perovskite obtained by using filtered and non-filtered PbI_2-solution under the two-step deposition process, PbI_2 and CH_3NH_3I. The XRD patterns are displayed in Fig. 4.12. The red and black curves in Fig. 4.12(a) show the XRD spectra measured for solid state $CH_3NH_3PbI_3$ films prepared by using filtered and non-filtered PbI_2-solution, respectively. The dipping time was 60 s for both of the samples. The samples were subsequently left to dry in the air at RT, and then thermally annealed at 100 °C for 90 min under dark conditions. The XRD patterns of PbI_2 film prepared through spin-coating on FTO glass substrate were shown in the gray black curve. For comparison, nanocrystalline powder of CH_3NH_3I was prepared and their XRD spectrum (green line) displayed in Fig. 4.12(b). The stronger diffraction peaks were observed for $CH_3NH_3PbI_3$ film prepared using filtered PbI_2-solution compared to the non-filtered PbI_2-solution.The strong diffraction peaks at 14.08°, 28.41°, 31.85°, and 43.19° are assigned as the (110), (220), (310), and (330) planes of a cubic $CH_3NH_3PbI_3$, which are in good agreement with the previous reports,[29,54,31] indicating that the perovskite structure with high crystallinity is formed.[56] The presence of FTO peaks are indicated by asterisks in Fig. 4.12(a). However, there are peaks that show the presence of unreacted PbI_2 which may partly affect the morphology and optical properties of perovskite layers. It is unclear where the unreacted PbI_2 exactly exists. The amount of unreacted PbI_2 may depend on the concentration of the CH_3NH_3I solution. I believe this factor is also related to surface roughness that occurs during conversion.
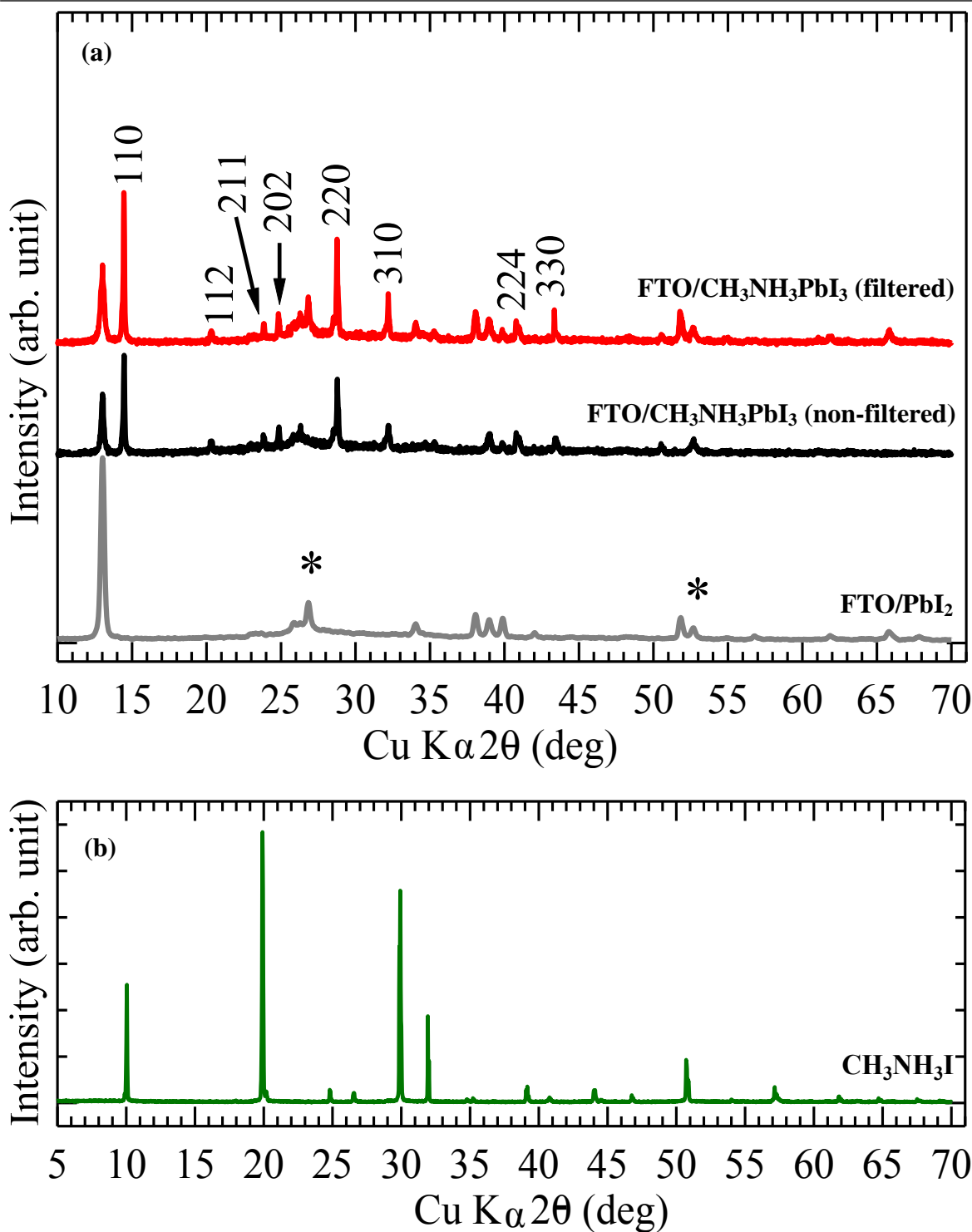
Figure 4.12: (a) XRD patterns of $CH_3NH_3PbI_3$ film prepared using filtered PbI_2-solution (red line) and non-filtered PbI_2-solution (black line) in addition to PbI_2 film grown on FTO substrate using filtered PbI_2-solution (gray line). Asterisks denote the FTO substrate peaks. (b) XRD spectrum of nanocrystalline CH_3NH_3I (green line). Reprint with permission from ref.[38] Copyright 2015, Japan Society of Applied Physics.

4.4.2.3 Analysis of optical absorption

The transformation of PbI_2 to $CH_3NH_3PbI_3$ through the two-step deposition method was also investigated by UV-visible spectroscopy. The UV-vis absorption spectra of the $CH_3NH_3PbI_3$ perovskite material grown on FTO/ZnO NWs substrates are presented in Fig. 4.13. The samples prepared using filtered and non-filtered PbI_2-solution show the typical absorption spectrum of the $CH_3NH_3PbI_3$ perovskite which was consistent with the reported literatures.[21,28,57] The absorption spectra of the samples cover almost all the visible to near infrared region over the spectral range about 400 - 800 nm. This is in agreement with the energy bandgap of 1.5 eV for $CH_3NH_3PbI_3$ perovskite.[58]

For both of the two samples, a clear absorption edge appears at about 790 nm, which is attributed to formation of $CH_3NH_3PbI_3$ perovskite. However, the sample prepared by using filtered PbI_2-solution shows the enhanced light harvesting in the whole spectrum compared to the sample prepared by using non-filtered PbI_2-solution. Such an enhancement is related to the variation in the crystallinity and morphology of $CH_3NH_3PbI_3$ films, *i.e.*, the relative increase in the crystallites grain size of perovskite material and surface coverage of perovskite film which can also be confirmed from the FE-SEM results. The relative shifted upwards of the whole spectrum can be attributed to the light scattering or and light trapping effects caused by the formation of large perovskite crystals.[59]

The inset shows the differential spectrum estimated from the original absorbance of filtered PbI_2-solution and non-filtered PbI_2-solution curves. The feature of the differential spectrum is exponential-like with a peak around 500 nm wavelength associated with crystalline PbI_2.[60] This implies that the majority of absorption enhancement of the filtered PbI_2-solution may be due to scattering and absorption effects of the PbI_2 at short wavelengths, although further study is required to elucidate the mechanistic details of absorption enhancement and deterioration.
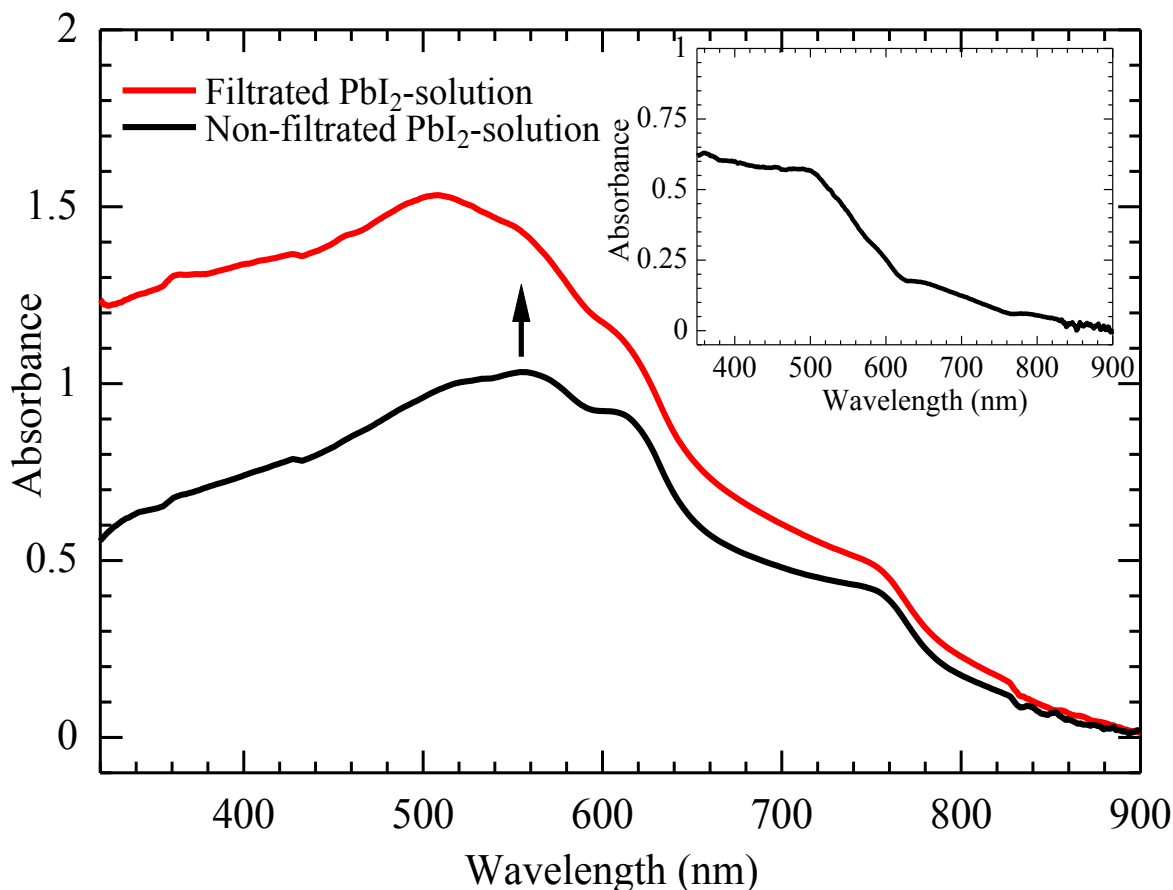
Figure 4.13: UV-vis absorption spectra of the $CH_3NH_3PbI_3$ perovskite material grown on FTO/ZnO NWs samples by using filtered and non-filtered PbI_2-solutions. All measurements were carried out using an integrating sphere. Absorption of FTO/ ZnO NWs was subtracted for all samples and set the absorbance of 0 at 900 nm. Reprint with permission from ref.[38] Copyright 2015, Japan Society of Applied Physics.

4.4.2.4 Device performance measurements

The effects of surface coverage and crystallinity of the $CH_3NH_3PbI_3$ films were evaluated from the performance of the perovskite solar cells. *J-V* characteristics of the perovskite solar cells (using filtered and non-filtered PbI_2 solution) were performed in air around 27-28 hours later, from the growth of $CH_3NH_3PbI_3$ crystals on the FTO/ZnO NWs. The results of *J-V* characteristics are displayed in Fig. 4.14. In the case of best device prepared using filtered PbI_2-solution, I derive values for the J_{SC}, V_{OC}, *FF* and *PCE* of 7.6 mA cm^{-2},

0.79 V, 0.63 and 4.8%, respectively. Besides, the device fabricated by using non-filtered PbI$_2$-solution exhibits values for the J_{SC}, V_{OC}, *FF* and *PCE* of 4.78 mA cm^{-2}, 0.69 V, 0.33, and 1.4%, respectively. Using filtered PbI$_2$-solution, I obtained a higher J_{SC} compared with the device prepared by using non-filtered PbI$_2$-solution. The reason for having higher J_{SC} would be probably because of improvement of crystallites grain size and surface coverage of CH$_3$NH$_3$PbI$_3$ perovskite film as shown in in Fig. 4.11(b). Hence, my approach is a significant contribution that clarifies the role of filtration of PbI$_2$-solution in improving the surface coverage and morphology of the CH$_3$NH$_3$PbI$_3$ film, yielding a higher performance of the perovskite solar cells.

Recent studies have reported the PCE of 15.4% for ZnO NWs-based perovskite solar cells,[61] that is significantly higher than the observed PCE of 4.8%. The major difference is in J_{SC}, which can be ascribed to the current leakage. This can be attributed to the incomplete coverage of perovskite film on FTO/ZnO NWs indicated by the red dotted line in Fig. 4.11(b). Sufficient surface coverage not only reduces the amount of light passed straight through the cell without absorption, but also reduces charge recombination at the interfaces. In order to quantify the effects of surface coverage of CH$_3$NH$_3$PbI$_3$ layers on the current leakage, I have estimated shunt resistance (R_{sh}) from the slope of reverse bias part of the current-voltage (*I-V*) curve in the range of -0.10 V to -0.07 V. The estimated R_{sh} values for filtered and non-filtered PbI$_2$-solution were approximately 255 Ω and 187 Ω, respectively. The lower V_{OC} might be due to the direct contact of HTL with the ZnO NWs. Hence, precisely controlled morphology of the CH$_3$NH$_3$PbI$_3$ films is essential for boosting performance of the perovskite solar cell. This could be achieved by varying the process conditions, such as the rate of spin-coating, layer thickness, annealing temperature and condition together with this filtering approach.
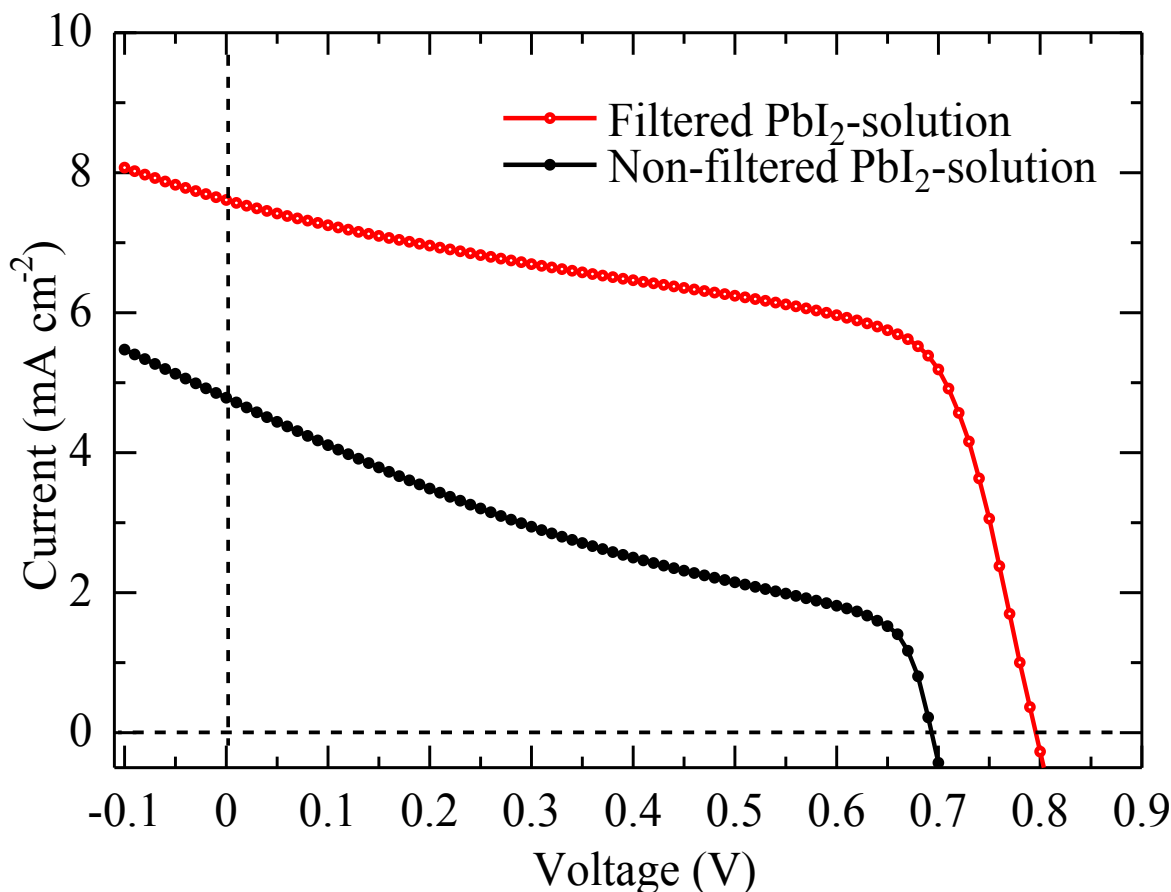
Figure 4.14: *J-V* curves of the highest-performing perovskite solar cells measured under solar irradiation and in the dark. The red line and black line represent the *J-V* curves of the devices in which the $CH_3NH_3PbI_3$ film was prepared using filtered PbI_2-solution and non-filtered PbI_2-solution, respectively. Reprint with permission from ref.[38] Copyright 2015, Japan Society of Applied Physics.

4.5 STABILITY STUDIES FOR MATERIALS AND DEVICES

Perovskite solar cells have demonstrated the possibility of achieving high PCEs comparable to those attained for thin film solar cells. However, in practical applications, the solar cells suffer from unstable and rapid decomposition with water, light and heat that drastically reduce the performance of devices within a short period of time. This is due to

the instability of both the perovskites and charge transport materials used in the solar cells. Therefore, reliability issues are the major concerns for commercial implementation.

The stability of the perovskite materials greatly depends on the quality of its components, for instance Pb-based perovskites (*i.e.,* $CH_3NH_3PbCl_3$, $CH_3NH_3PbBr_3$ and $CH_3NH_3PbI_3$) materials are extremely sensitive to moisture due to their ionic nature. The degradation of perovskite materials (*i.e.*, CH_3NH_3I and PbI_2) is very fast and it can be completed within several minutes in the existence of water. However, Sn-based perovskites are extremely sensitive to air and moisture that lead to decompose partially within 2 h and completely after just one day.[62,63] The Pb-based perovskites are known to undergo phase transitions.[64,65,66] In particular, $CH_3NH_3PbI_3$ undergoes phase transitions from tetragonal to cubic around 54 °C, which is very near to operating-temperature of the solar cell under direct sunlight. Furthermore, the perovskites may decompose due to annealing process. For growth of $CH_3NH_3PbI_3$ films, annealing is normally carried out at 100 °C for tens of minutes. Dualeh *et al*,[67] reported that the perovskite begins to decompose into PbI_2, CH_3NH_3I when the annealing temperature is higher than 120 °C. Once the annealing temperature attains around 300 °C, the perovskite decomposes into PbI_2, CH_3NH_2 and HI.

For investigation of various degradation pathways of perovskite, it is important to understand its basic chemical reactions: $PbI_2(s) + CH_3NH_3I (aq) \leftrightarrow CH_3NH_3PbI_3 (s)$. Since the reaction is reversible, there is perovskite formation in one direction, while the other brings about decomposition. Mainly, humidity, UV light, oxygen, solution (solvent, solute), and temperature are the major contributors for perovskite degradation.[68] In the presence of moisture, $CH_3NH_3PbI_3$ tends to hydrolyze because of its high sensitivity to water, leading to the degradation of perovskite. The degradation occurs according to the following reaction mechanism:

$$CH_3NH_3PbI_3 \text{ (s)} \leftrightarrow PbI_2 \text{ (s)} + CH_3NH_3I \text{ (aq)} \qquad (4.8)$$

$$CH_3NH_3I \text{ (aq)} \leftrightarrow CH_3NH_2 \text{ (aq)} + HI \text{ (aq)} \qquad (4.9)$$

$$4HI \text{ (aq)} + O_2 \text{ (g)} \leftrightarrow 2I_2 \text{ (s)} + 2H_2O \text{ (l)} \qquad (4.10)$$

$$2HI \text{ (aq)} \leftrightarrow H_2 \text{ (g)} + I_2 \text{ (s)} \qquad (4.11)$$
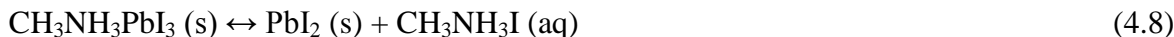
The first step reveals that the highly hygroscopic CH_3NH_2 ion is removed from the $CH_3NH_3PbI_3$ crystal and connects with iodine to rebuild aqueous CH_3NH_3I and solid PbI_2 salt. Subsequently, CH_3NH_3I may decompose into aqueous CH_3NH_2 and HI. Next, HI degrades with O_2 or by a redox reaction results in a formation of H_2O and I_2. Finally, I_2 and gaseous hydrogen are formed from the HI *via* a photochemical reaction induced by UV radiation. Noh *et al.*[69] reported that the decomposition of perovskite occurs at humidity levels as low as 55%, subsequent change in color from dark black to yellow.

4.6 CHAPTER SUMMARY

Solid state organic-inorganic perovskite solar cells based on ZnO NWs have been fabricated successfully. The synthesis of CH_3NH_3I, $CH_3NH_3PbI_3$ layers and spin-coating of P3HT were carried out under ambient conditions where the dry atmosphere is unnecessary to achieve the perovskite crystal properly. Very simple, easy and low-cost ambient air process may reduce the manufacturing costs of perovskite solar cells for industrial production. Since the controlled morphology of the $CH_3NH_3PbI_3$ films is crucial due to improve efficiency, I have demonstrated that the filtration of PbI_2-solution has a major effect on morphology of $CH_3NH_3PbI_3$-film. The perovskite solar cell fabricated by using filtered PbI_2-solution showed a PCE of 4.8%, with a J_{SC} of 7.6 mA cm^{-2}, a V_{OC} of 0.79 V and a FF of 0.63, which are significantly better than the device based on non-filtered PbI_2-solution. Characterizations using FE-SEM, UV-vis-NIR and *J-V* curves showed that the filtration of PbI_2-solution is necessary for uniform growth of $CH_3NH_3PbI_3$ film with higher

surface coverages to achieve higher efficiency of perovskite solar cells.

There is enormous scopes for further research to enhance the PCE of perovskite solar cells by improving the perovskite surface coverage, which is sensitive to the concentration of perovskite solution, speed of spin-coating and annealing temperature as reported recently.[70] In addition, the enhancement of light absorption, optical path-length should be crucial, because the absorption drop-down around the NIR region. An incorporation of LSPR of Ag NPs would be one of the effective routes to control the propagation of light through the devices, resulting in an enhancement in photocurrent generation and efficiency of the solar cell. Preparation, characterization and application of Ag NPs to the perovskite solar cells will be described in chapter 5.

References

[1] V. P. Koch, R. Hezel, A. Goetzberger, *High-Efficient Low-Cost PhotoVoltaics* (Springer Series in Optical Sciences, 2009). Vol. 140.

[2] T. B. Song, Q. Chen, H. Zhou, C. Jiang, H. H. Wang, Y. M. Yang, Y. Liu, J. You and Y. Yang, J. Mater. Chem. A **3**, 9032-9050 (2015).

[3] J. Fan, B. Jia and M. Gu, Photon. Res. **2**, 111-120 (2014).

[4] N. G. Park, J. Phys. Chem. Lett. **4**, 2423-2429 (2013).

[5] N. G. Park, Mater. Today **18**, 65-72 (2015).

[6] P. P. Boix, K. Nonomura, N. Mathews and S. G. Mhaisalkar, Mater. Today **17**, 16-23 (2014).

[7] J. You, Z. Hong, Y. M. Yang, Q. Chen, M. Cai, T. B. Song, C. C. Chen, S. Lu, Y. Liu, H. Zhou and Y. Yang, ACS Nano **8**, 1674-1680 (2014).

[8] L. Zheng, D. Zhang, Y. Ma, Z. Lu, Z. Chen, S. Wang, L. Xiao and Q. Gong, Dalton Trans. **44**, 10582-10593 (2015).

[9] M. A. Green, A. H. Baillie and H. J. Snaith, Nat. Photonics **8**, 506 (2014).

[10] S. Luo and W. A. Daoud, J. Mater. Chem. A **3**, 8992-9010 (2015).

[11] B. Wang, X. Xiao and T. Chen, Nanoscale **6**, 12287-12297 (2014).

[12] G. Hodes, Science **342**, 317-318 (2013).

[13] J. H. Im, I. H. Jang, N. Pellet, M. Grätzel and N. G. Park, Nat. Nanotechnol. **9**, 927-932 (2014).

[14] J. J. Choi, X. Yang, Z. M. Norman, S. J. L. Billinge and J. S. Owen, Nano Lett. **14**, 127-133 (2014).

[15] S. Sun, T. Salim, N. Mathews, M. Duchamp, C. Boothroyd, G. Xing, T. C. Sum and Y. M. Lam, Energy Environ. Sci. **7**, 399-407 (2014).

[16] T. Miyasaka, Chem. Lett. **44**, 720-729 (2015).

[17] G. Xing, N. Mathews, S. Sun, S. S. Lim, Y. M. Lam, M. Grätzel, S. Mhaisalkar and T. C. Sum, Science **342**, 344-347 (2013).

[18] S. D. Stranks, G. E. Eperon, G. Grancini, C. Menelaou, M. J. P. Alcocer, T. Leijtens, L. M. Herz, A. Petrozza and H. J. Snaith, Science **342**, 341-344 (2013).

[19] T. Salim, S. Sun, Y. Abe, A. Krishna, A. C. Grimsdale and Y. M. Lam, J. Mater. Chem. A **3**, 8943-8969 (2015).

[20] A. Kojima, K. Teshima, Y. Shirai and T. Miyasaka, J. Am. Chem. Soc. **131**, 6050-6051 (2009).

[21] J. H. Im, C. R. Lee, J. W. Lee, S. W. Park and N. G. Park, Nanoscale **3**, 4088-4093 (2011).

[22] S. Kazim, M. K. Nazeeruddin, M. Grätzel and S. Ahmad, Angew. Chem. Int. Ed. **53**, 2812-2824 (2014).

[23] T. C. Sum and N. Mathews, Energy Environ. Sci. **7**, 2518-2534 (2014).

[24] S. Gamliel and L. Etgar, RSC Adv. **4**, 29012-29021 (2014).

[25] H. J. Snaith, J. Phys. Chem. Lett. **4**, 3623-3630 (2013).

[26] H. S. Kim, S. H. Im and N. G. Park, J. Phys. Chem. C **118**, 5615-5625 (2014).

[27] H. S. Kim, C. R. Lee, J. H. Im, K. B. Lee, T. Moehl, A. Marchioro, S. J. Moon, R. H. Baker, J. H. Yum, J. E. Moser, M. Grätzel and N. G. Park, Sci. Rep. **2**, 591 (2012).

[28] M. M. Lee, J. Teuscher, T. Miyasaka, T. N. Murakami and H. J. Snaith, Science **338**, 643-647 (2012).

[29] J. Burschka, N. Pellet, S. J. Moon, R. H. Baker, P. Gao, M. K. Nazeeruddin and M. Gra¨tzel, Nature **499**, 316-319 (2013).

[30] H. Zhou, Q. Chen, G. Li, S. Luo, T. b. Song, H. S. Duan, Z. Hong, J. You, Y. Liu and Y. Yang, Science **345**, 542-546 (2014).

[31] D. Liu and T. L. Kelly, Nature Photon. **8**, 133-138 (2013).

[32] Y. Ma, S. Wang, L. Zheng, Z. Lu, D. Zhang, Z. Bian, C. Huang and L. Xiao, Chin. J. Chem. **32**, 957-963 (2014).

[33] C. S. Ponseca Jr, T. J. Savenije, M. Abdellah, K. Zheng, A. Yartsev, T. Pascher, T. Harlang, P. Chabera, T. Pullerits, A. Stepanov, J. P. Wolf and V. Sundström, J. Am. Chem. Soc. **136**, 5189-5192 (2014).

[34] M. Law, L. E. Greene and J. C. Johnson, Nat. Mater. **4**, 455 (2005).

[35] D. C. Look, D. C. Reynolds, J. R. Sizelove, R. L. Jones, C. W. Litton, G. Cantwe and W. C. Harsch, Solid State Commun. **105**, 399-401 (1998).

[36] R. G. Breckenridge and W. R. Hosler, Phys. Rev. **91**, 793-802 (1953).

[37] Y. Xia, P. Yang, Y. Sun, Y. Wu, B. Mayers, B. Gates, Y. Yin, F. Kim and H. Yan, Adv. Mater. **15**, 353 (2003).

[38] M. M. Rahman, N. Uekawa, F. Shiba, Y. Okawa, M. Sakai, K. Yamamoto, K. Kudo and T. Konishi, Jpn. J. Appl. Phys. **55**, 01AE09 (2015) .

[39] J. H. Heo, S. H. Im, J. H. Noh, T. N. Mandal, C. S. Lim, J. A. Chang, Y. H. Lee, H. j. Kim, A. Sarkar, M. K. Nazeeruddin, M. Gra¨tzel and S. I. Seok, Nat Photon. **7**, 486-491 (2013).

[40] L. Zheng, Y. Ma, S. Chu, S. Wang, B. Qu, L. Xiao, Z. Chen, Q. Gong, Z. Wu and X. Hou, Nanoscale **6**, 8171-8176 (2014).

[41] W. Tress, N. Marinova, O. Inganäs, M. K. Nazeeruddin, S. M. Zakeeruddin and M. Grätzel, (40th Photovoltaic Specialist Conference, 2014); IEEE, p.1563-1566.

[42] N. Marinova, W. Tress, R. H. Baker, M. I. Dar, V. Bojinov, S. M. Zakeeruddin, M. K. Nazeeruddin and M. Grätzel, ACS Nano **9**, 4200-4209 (2015).

[43] I. K. Ding, N. Tétreault, J. Brillet, B. E. Hardin, E. H. Smith, S. J. Rosenthal, F. Sauvage, M. Grätzel and M. D. McGehee, Adv. Funct. Mater. **19**, 2431-2436 (2009).

[44] G. G. Belmonte, A. Munar, E. M. Barea, J. Bisquert, I. Ugarte and R. Pacios, Org. Electron. **9**, 847-851 (2008).

[45] K. Yang, Y. Wang, A. Jain, L. Samulson and J. Kumar, J. Macromol. Sci., Part A: Pure Appl.Chem. **44**, 1261-1264 (2007).

[46] S. A. Choulis, Y. Kim, J. Nelson, D. D. C. Bradley, M. Giles, M. Shkunov and I. McCulloch, Appl. Phys. Lett. **85**, 3890-3892 (2004).

[47] F. D. Giacomo, S. Razza, F. Matteocci, A. D'Epifanio, S. Licoccia, T. M. Brown and A. D. Carlo, J. Power Sources **251**, 152-156 (2014).

[48] R. Søndergaard, M. Hösel, D. Angmo, T. T. Larsen-Olsen and F. C. Krebs, Mater. Today **15**, 36-49 (2012).

[49] H. J. Snaith, A. J. Moule, C. Klein, K. Meerholz, R. H. Friend and M. Grätzel, Nano Lett. **7**, 3372-3376 (2007).

[50] https://en.wikipedia.org/wiki/Ultraviolet%E2%80%93visible_spectroscopy.

[51] http://www.perkinelmer.com/pdfs/downloads/APP_UseofUVVisNIRinDevelopment PV.pdf

[52] M. F. Cansizoglu, R. Engelken, H. W. Seo and T. Karabacak, ACS Nano **4**, 733 (2010).

[53] Y. H. Ko and J. S. Yu, Phys. Status Solidi A **208**, 2778-2782 (2011).

[54] Q. Chen, H. Zhou, Z. Hong, S. Luo, H. S. Duan, H. H. Wang, Y. Liu, G. Li and Y. Yang, J. Am. Chem. Soc. **136**, 622-625 (2014).

[55] W. Nie, H. Tsai, R. Asadpour, J. C. Blancon, A. J. Neukirch, G. Gupta, J. J. Crochet, M. Chhowalla, S. Tretiak, M. A. Alam, H. L. Wang and A. D. Mohite, Science **347**, 522-525 (2015).

[56] T. Baikie, Y. Fang, J. M. Kadro, M. Schreyer, F. Wei, S. G. Mhaisalkar, M. Gra¨tzel and T. J. White, J. Mater. Chem. A **1**, 5628-5641 (2013).

[57] Y. Zhao and K. Zhu, J. Phys. Chem. Lett. **4**, 2880 (2013).

[58] S. D. Wolf, J. Holovsky, S. J. Moon, P. Löper, B. Niesen, M. Ledinsky, F. J. Haug, J. H. Yum and C. Ballif, J. Phys. Chem. Lett. **5**, 1035-1039 (2014).

[59] S. M. Jain, B. Philippe, E. M. J. Johansson, B. W. Park, H. Rensmo, T. Edvinsson and G. Boschloo, J. Mater. Chem. A (2016). DOI: 10.1039/C5TA08745G

[60] J. A. Christians, P. A. Miranda Herrera and P. V. Kamat, J. Am. Chem. Soc. **137**, 1530-1538 (2015).

[61] J. Dong, Y. Zhao, J. Shi, H. Wei, J. Xiao, X. Xu, J. Luo, J. Xu, D. Li, Y. Luo and Q. Meng, Chem. Commun. **50**, 13381-13384 (2014).

[62] F. Hao, C. C. Stoumpos, D. H. Cao, R. P. H. Chang and M. G. Kanatzidis, Nat. Photonics **8**, 489-494 (2014).

[63] N. K. Noel, S. D. Stranks, A. Abate, C. Wehrenfennig, S. Guarnera, A. A. Haghighirad, A. Sadhanala, G. E. Eperon, S. K. Pathak, M. B. Johnston, A. Petrozza, L. M. Herz and H. J. Snaith, Energy Environ. Sci. **7**, 3061-3068 (2014).

[64] N. Onoda-Yamamuro, T. Matsuo and H. Suga, J. Phys. Chem. Solids **51**, 1383-1395 (1990).

[65] H. Mashiyama and Y. Kurihara, J. Korean Phys. Soc. **32**, S156 (1998).

[66] A. Poglitsch and D. Weber, J. Chem. Phys. **87**, 6373 (1987).

[67] A. Dualeh, N. Tétreault, T. Moehl, P. Gao, M. K. Nazeeruddin and M. Grätzel, Adv. Funct. Mater. **24**, 3250-3258 (2014).

[68] G. Niu, X. Guo and L. Wang, J. Mater. Chem. A **3**, 8970-8980 (2015).

[69] J. H. Noh, S. H. Im, J. H. Heo, T. N. Mandal and S. I. Seok, Nano Lett. **13**, 1764-1769 (2013).

[70] G. E. Eperon, V. M. Burlakov, P. Docampo, A. Goriely and H. J. Snaith, Adv. Funct. Mater. **24**, 151-157 (2014).

CHAPTER FIVE

Application of Silver Nanoparticles in Organic-Inorganic Perovskite Solar Cells

Fabrication of Ag NPs and their application to the ZnO NWs based organic-inorganic perovskite solar cells are described in this section. Ag NPs were successfully prepared by PVD method and subsequent thermal annealing was carried out. The growth of the Ag NPs and their diverse characterizations used to elucidate the morphology and optical properties are described in this section. The absorption peaks in the UV-vis spectra were detected and the peaks displayed a red-shift with increase in average size of NPs. Such facts imply that the absorption peaks may emerge due to the LSPR. Subsequently, the synthesized NPs were integrated into the ZnO NWs based organic-inorganic perovskite solar cells and their performances were measured. The effects of Ag NPs on PCE of solar cells are explained in this section.

5.1 SILVER NANOPARTICLES

Recently, there have been highly extensive interests in NPs as well as their size-dependent characteristics. Various types of noble metal NPs, for instance, Au, Cu and Ag NPs exhibit a strong absorption band in the UV-vis-NIR region that are greatly depends on the size and shape of NPs, but in the case of bulk metal, the former facts are not observed.[1-4] The absorption band appears when the light impinge on metal NPs with a diameter smaller than the light of wavelength; it originates collective oscillations of the conduction electrons at a frequency are known as LSPR.[5-8] Excitation of LSPR are the consequences of absorption of selective photons and formation of locally enhanced EM fields at the surface of NPs. EM fields enhanced by raising the size of NPs, yielding a higher scattering and lower absorption of light.[9-12] The enrichment of optical absorption and scattering at the LSPR wavelength can be considered to be the basis of applications in plasmonics,[8] biosensors,[13] optical sensors,[14] surface-enhanced spectroscopies,[15] DSCs,[16-20] and so on.

For solar cells system, it is crucial that the active layer of the device absorbs as many photons as possible to generate more carrier electrons. In other words, the equal photocurrent may be generated with a decreased film thickness as well as an additional enhancement is anticipated in thinner solar cell as a result of suppressed carrier recombination and thus decreased internal resistance. Accordingly, Ag NPs can contribute for efficient light absorption of solar cells, through the local-field enhancement *via* the LSPR, and the light scattering leading to extended optical-path lengths.[21] The absorption spectrum of the active layer in the solar cell is potentially tunable by adjusting the size and shape of NPs. Therefore, cost effective and controlled fabrication of Ag NPs is highly desired for efficient solar cell application.

Here, I employed Ag NPs to ZnO NWs based organic-inorganic perovskite solar cell for the first time, aiming at enhanced light absorption led to a higher photocurrents and PCE. Although the absorption coefficient of organic-inorganic perovskite at 550 nm is apparently 1.5×10^4 cm^{-1},[22-24] the absorption is drop-down around the band edge.[25] Therefore, it should be a promising to enhance the light absorption of organic-inorganic perovskite through the integration of plasmonic Ag NPs.

5.2 FABRICATION PROCEDURES OF NANOPARTICLES

Various methods have been used to fabricate the Ag NPs, for example, magnetron sputtering,[26] electrochemical deposition,[27] hydrothermal treatment,[28] electron beam lithography,[29] and so on. Among the major methods used for Ag NPs synthesis are classified as physical and chemical methods. However, the synthetic cost and the requirement of toxic substances which may absorb onto Ag NPs are the major problems of chemical and physical methods. In this case, the vacuum vapor evaporation or PVD method would be the feasible alternatives due to overcome the above mentioned issues.[30]

Considering these advantages, I have employed PVD method which is very simple, low-cost, quite reliable and popular as well as it is capable of producing uniform Ag layers on the substrate. The Ag films were subsequently annealed thermally due to the growth of Ag NPs or nanoislands.

The indium tin oxide (ITO) coated glass substrates was collected from the Luminescence Technology. The thickness of ITO films was around 120-160 nm with a sheet resistivity of 9-15Ω/sq. The substrates were cleaned sequentially by scrubbing both sides with the semicoclean (Furuuchi Chemical semicoclean 23) and deionized water, acetone, and isopropanol under sonication for 10 min. The substrates were subsequently dried with N_2-blow as well as the UV ozone treatment was performed for 20 min. After surface treatments, the substrates were rapidly transferred into deposition chamber, where high purity (99.99%) Ag (Nilaco) was deposited on the 3×3 cm^2 ITO/glass substrates by using a thermal evaporator. Typically, 1 - 20 nm mass thicknesses of Ag films were successively deposited under dark condition. Deposition rates of Ag and base pressure of the deposition chamber were 0.05 - 0.06 nm s^{-1} and 7×10^{-4} Pa, respectively. The thicknesses of Ag layer were measured by using a quartz crystal-sensor. After deposition, the samples were annealed under an ambient condition at 500 °C for 1 - 20 min. Similarly, Ag layers of 1 - 15 nm in mass thicknesses were deposited on FTO glass substrate. Subsequently, the annealing treatment was performed under vacuum condition at 500 °C for 30 min.

5.3 CHARACTERIZATIONS AND MEASUREMENTS

The morphology of self-organized Ag NPs or nanoislands was investigated through the FE-SEM (JEOL, JSM-6340F). The sizes and distributions of Ag NPs acquired from the FE-SEM images were estimated by using imageJ 1.45s software. Elemental analyses of the

Ag NPs were carried out *via* EDX analyzer which was attached with FE-SEM. The optical properties of the Ag NPs were characterized by Shimadzu UV-vis-NIR scanning spectrophotometer (UV-3100 PC) which was consisted of an integrating sphere. The measurements were performed at RT where the wavelengths of light were ranged from 300 to 1000 nm and the incident beam-angle was set to 0°. The diffuse-reflectance spectra were obtained by using the reference material as $BaSO_4$ powder.

5.4 RESULTS AND DISCUSSIONS

5.4.1 Morphology of silver nanoparticles

The annealing temperature is a crucial parameter of the experiment because the annealing temperature, which in turn can lead to surface energies, diffusions, and mobilities of the Ag atoms that can have influences on the size, distance between NPs, and the shape of Ag NPs. The Ag NPs fabricated by using 5-20 nm thick films through annealing at 500 °C for 1-20 min are shown in Fig. 5.1. One can notice that the small NPs with high-density grow rapidly within a few minutes of annealing, typically 1 - 10 min, afterwards the rate of growth decreases sharply. The size of Ag NPs increased with increasing the time of annealing while their density decreases. The spherical shaped NPs were formed and they were dispersed randomly on the substrates surface due to long-time annealing, typically 20 min. However, a small portion of NPs were progressively aggregated with increasing the time of annealing. Moreover, the average size and density of Ag NPs were increased with increasing thicknesses of Ag films while their annealing time was constant. From the FE-SEM images, it can be observed in case of 5 nm thick-film that the sizes, shapes and distributions of NPs become uniform with rising the time of annealing as shown in Fig. 5.1(a). The average diameter of NPs ranged from 60.5 - 176.5 nm, while their density per image declined notably between 11.6 - 4.0%.
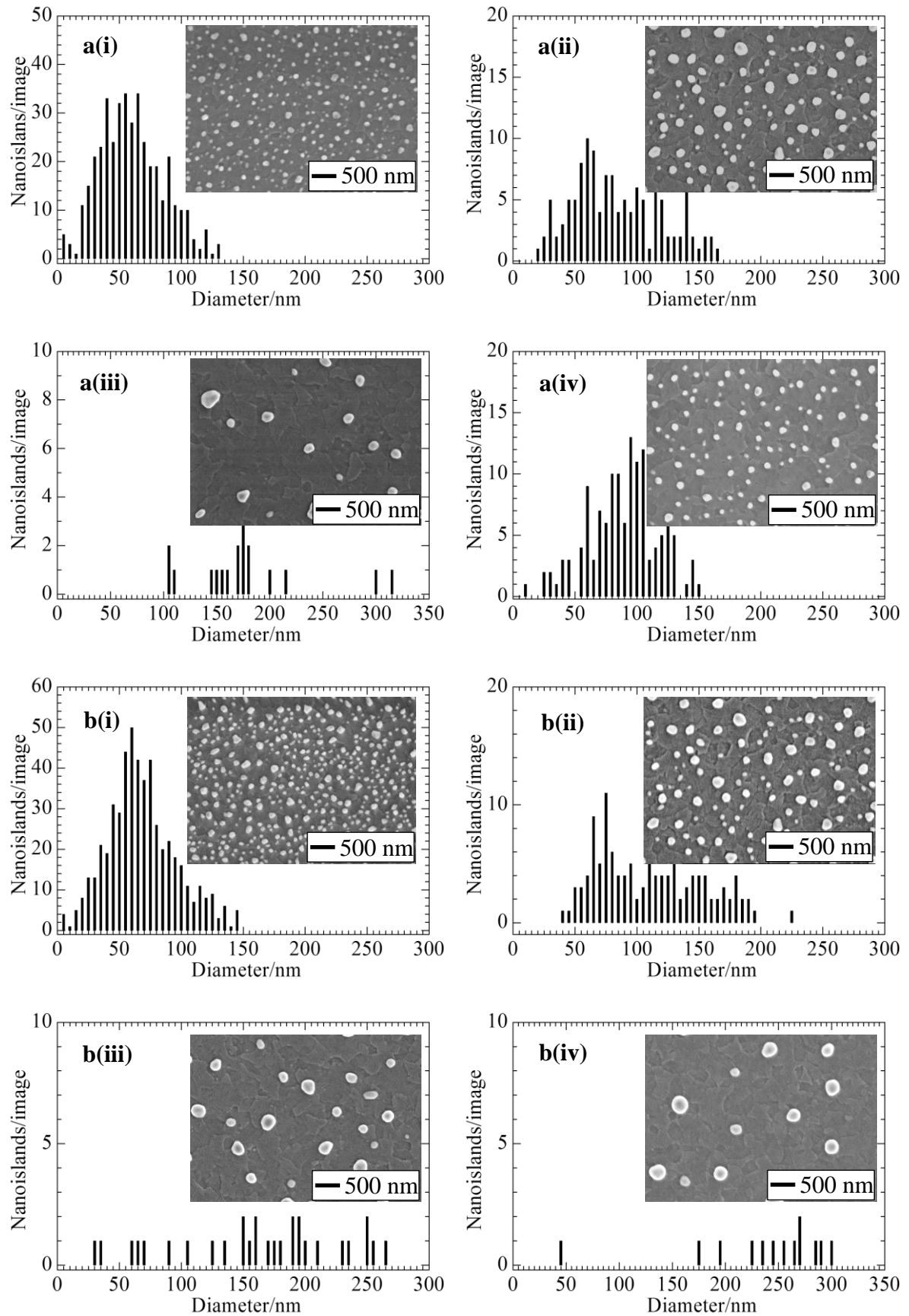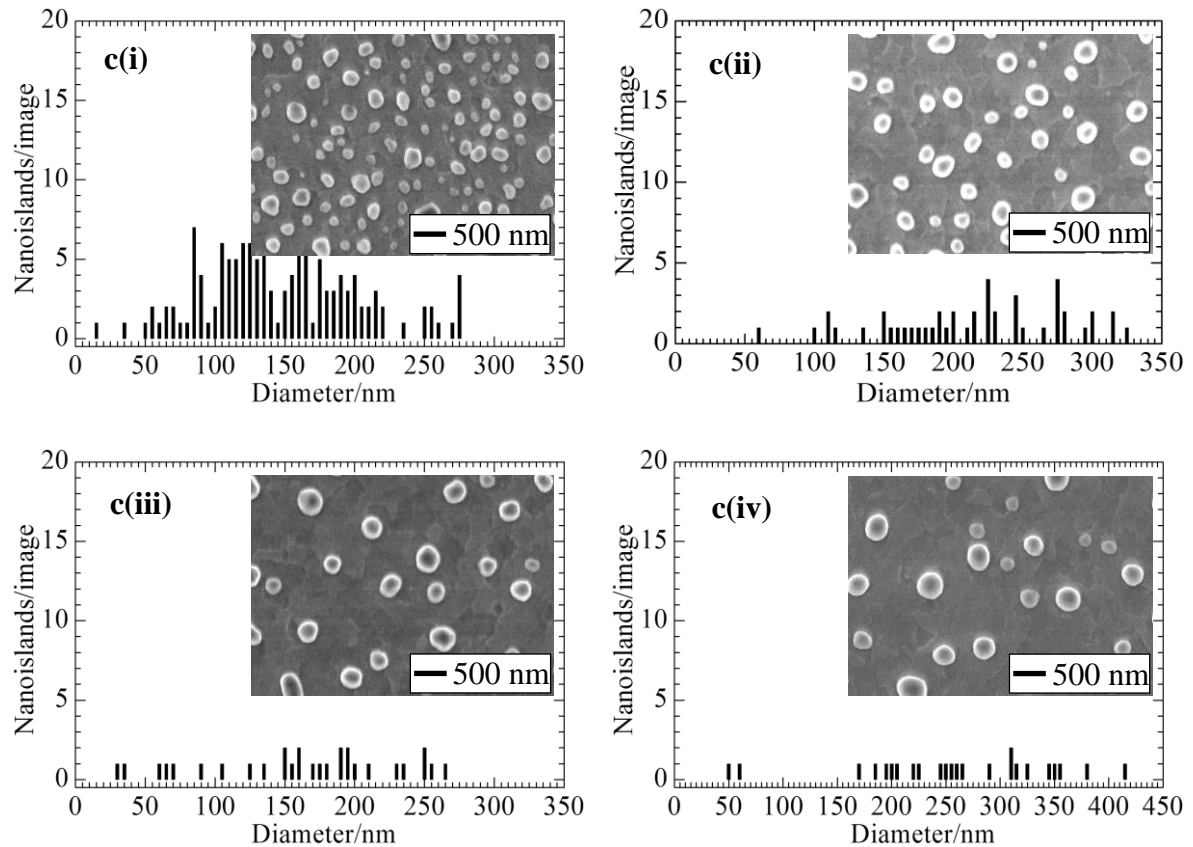
Figure 5.1: FE-SEM images and histograms of various sized NPs prepared by using (a) 5, (b) 10, and (c) 20 nm thick-films of Ag deposited on ITO/glass substrates and subsequent annealing under ambient condition at 500 °C for (i) 1, (ii) 5, (iii) 10, and (iv) 20 min. Adapted with permission from ref.[12] Copyright 2015, Japan Society of Applied Physics.

Figure 5.1 (b) displays the FE-SEM images of Ag NPs prepared by using 10 nm thick films. The distributions of NPs are mostly uniform. Actually, these NPs agglomerated and formed likely, 3D islands with different sizes of diameter, typically from 68 - 229 nm and their densities declined between 18.8 - 5.2% with increasing the time of annealing. In case of 20 nm thick-films of Ag, the average diameter of NPs monotonically increases from 148 - 258 nm and their densities reduced between 22.2 - 11.8% with increasing the time of annealing as shown in Fig. 5.1(c). The densities and diameter sizes of NPs comparably increased with increasing the thicknesses of film and the time of annealing. Table 5.1 shows the average size and density of Ag NPs estimated from the FE-SEM images.

Table 5.1: Average diameter, standard deviation and density per image in percentage of NPs grown by using Ag films *via* annealing treatment at 500 °C. Adapted with permission from ref.[12] Copyright 2015, Japan Society of Applied Physics.

Sample of Ag film	Annealing time (min)	Average diameter of Ag NPs (nm)	Standard deviation (±)	Ag NPs density /image (%)
5 nm thick	1	60.5	25.5	11.5
	5	84.5	35.0	6.8
	10	176.5	56.0	4.0
	20	89.0	28	7.5
10 nm thick	1	68.0	27.5	18.8
	5	110.5	42.0	11.1
	10	161.0	67.0	5.8
	20	229.0	69.0	5.2
20 nm thick	1	148.0	57.0	22.2
	5	214.0	64.0	15.2
	10	252.5	76.5	12.4
	20	258.0	91.0	11.8

In order to investigate further the morphology of NPs, the Ag film thicknesses were increased to around 100 nm. Figure 5.2 displays that the dispersed nanoislands merged together and form continuous film-like structures, but the intricate-shape openings remained in the film. This would be attributed to the deficiency of thermal activated surface diffusion for 100 nm thick Ag film. Considering all these facts, it can be concluded that the atoms spread out from the surface of small nanoislands to that of larger nanoislands. Therefore, the quantities of small nanoislands decrease while the larger nanoislands increase.
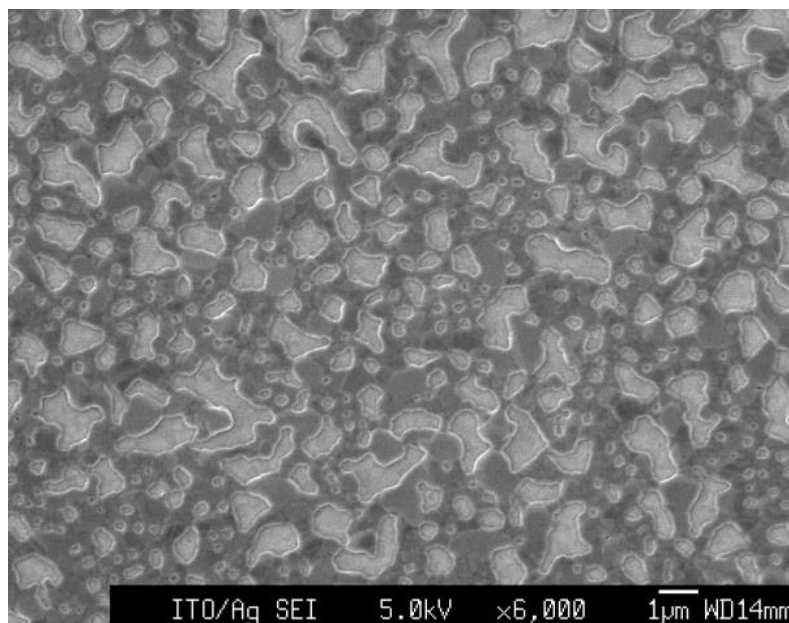
Figure 5.2: FE-SEM image of Ag nanoislands grown on ITO/glass substrate by using an Ag film with thickness of 100 nm and subsequent thermal annealing at 500 °C for 20 min under ambient condition. Adapted with permission from ref.[12] Copyright 2015, Japan Society of Applied Physics.

Figure 5.3 shows the FE-SEM images of Ag NPs prepared on FTO glass substrate by using Ag films with thickness of 1-15 nm followed by thermal annealing at 500 °C for 30 min under vacuum condition. Since the growth of ZnO NWs required high temperature around 500 °C, FTO glass substrate was chosen because of its higher stability at high temperatures. At high temperature, surface tension leads to the metal atoms of thin films to integrate together to form particles. The SEM images of Ag NPs prepared from the Ag films with thickness of 1-8 nm revealed that the form and distribution of NPs become more uniform after annealing. However, as the thickness of films increases, the NPs tend to lose their spherical shape which looks elongated and island-like. This result was consistent with the ITO/glass substrates that the mean average diameter increased with the increasing thickness. The estimated diameters of the NPs are 5, 15, 25, 40, 60, 90, 115, and 150 nm for film thickness of 1, 3, 5, 7, 8, 10, 12 and 15 nm, respectively.
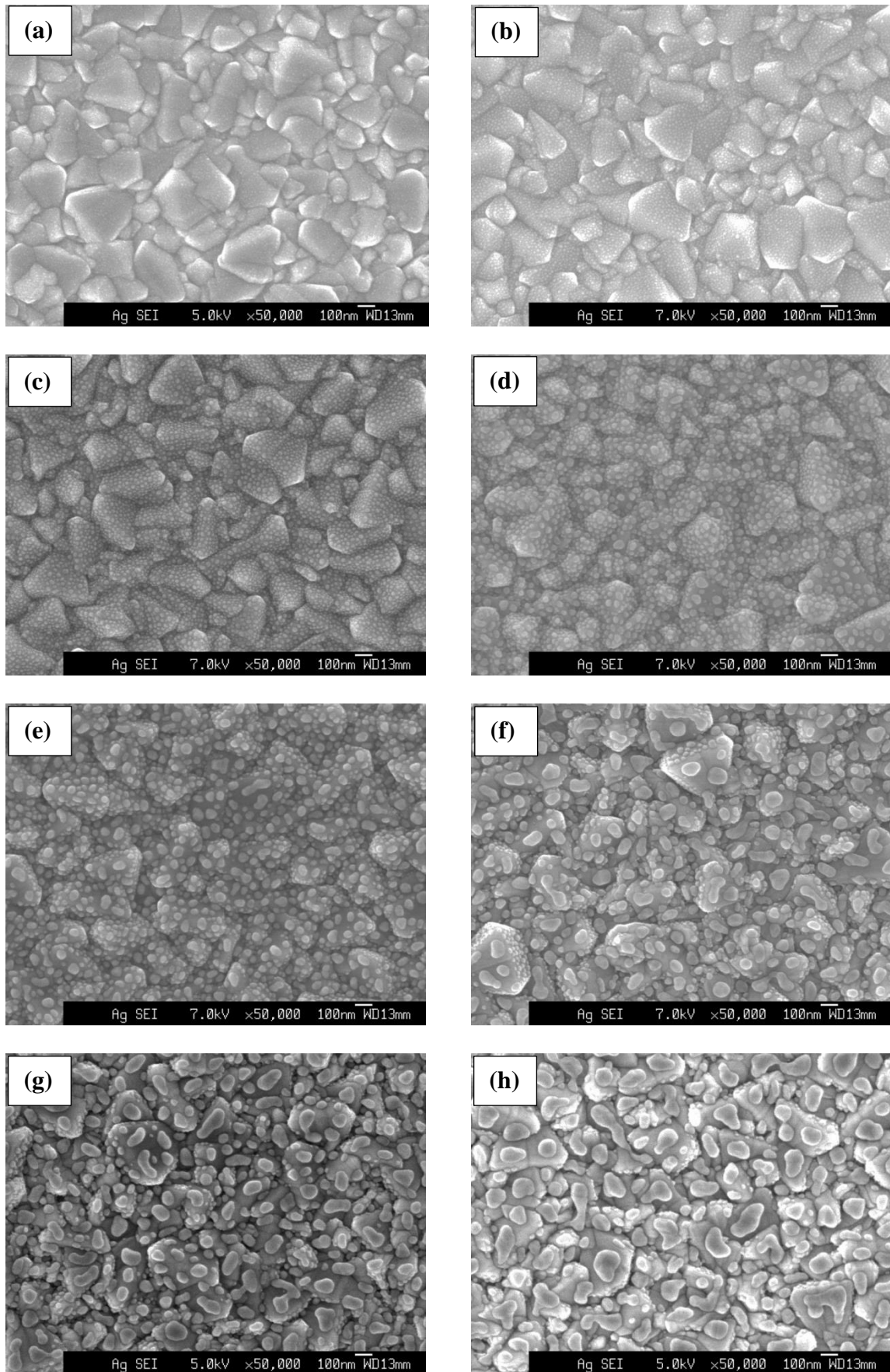
Figure 5.3: Top view of FE-SEM images of Ag NPs grown on FTO/glass substrate by using Ag film with thickness of (a) 1, (b) 3, (c) 5, (d) 7, (e) 8, (f) 10, (g) 12, and (h) 15 nm followed by thermal annealing at 500 °C for 30 min under vacuum condition.

5.4.2 Elemental analysis

Figure 5.4 displays the EDX spectrum of spherical shaped Ag NPs scattered randomly on ITO substrates. The vertical axis shows the number of X-ray counts per second while the horizontal axis reveals the energy in keV. The peaks around 3.0 - 3.4 keV corresponds to the binding energies of Ag while the peaks located at the binding energies of 3.2 keV and 3.5 keV belong to indium. Metallic Ag NPs usually exhibit the peak of EDX spectra approximately at 3.0 keV due to LSPR.[31]
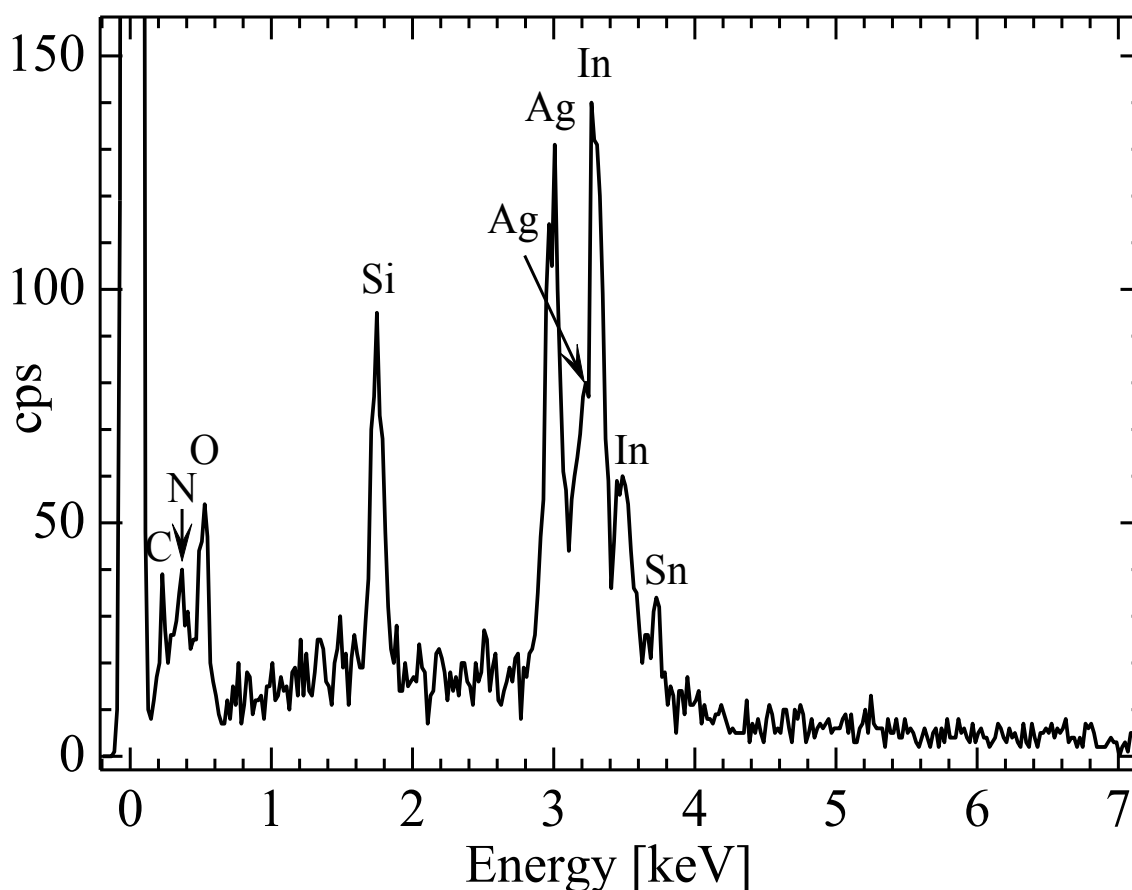
Figure 5.4: EDX spectrum of Ag NPs prepared from Ag film with thickness of 20 nm. Adapted with permission from ref.[12] Copyright 2015, Japan Society of Applied Physics.

The peaks around 1.8 and 3.8 keV correspond to the binding energies of silicon and tin, respectively. Such silicon and tin may be the part of elements of ITO/glass substrates. The peaks in the visible region confirm the existence of carbon, nitrogen and oxygen substances in the samples correspond to their binding energies of approximately 0.2, 0.4, and 0.6 keV, respectively. The carbon, nitrogen and oxygen peaks exhibited in the EDX analyses can be attributed to the surrounding residuals material and/or the carbon tape used for FE-SEM grid preparation. No obvious peaks belong to impurity is detected throughout the scanning ranges of binding energies. Considering all these aspects, it can be concluded that the Ag NPs are in metallic form and free from any other impurities. Therefore, the growth products are homogeneous, stable and consist of high purity Ag NPs.

5.4.3 Optical properties of silver nanoparticles

Optical properties of metallic NPs are greatly rely upon their size, shape, chemical composition and the surrounding dielectric environment.[10] For optical measurements, such as transmission, reflection, and absorption, the Ag NPs were prepared on ITO glass substrates. Firstly, the transmittance spectra of Ag NPs have been obtained in normal transmission mode of a UV-vis-NIR spectrophotometer under normal circumstance. The transmittance spectra are given as the percentage ratios of transmitting light to the incident light, and the percentage of transmittance is calculated as $\%T = (I/I_0) \times 100$,[32] where I is the transmitted light intensity, I_0 is the incident light intensity at a specific wavelength. Figure 5.5 displays the transmittance spectra of irregular, spherical shaped Ag NPs prepared from Ag films with thickness of 5 - 10 nm and subsequent thermal annealing ranges from 1 to 20 min. As can be seen in Fig. 5.5 (a), the transmittance of 5 nm thick films were increased from ~70 - 86% with increasing the annealing time and saturated at 10 min. For 10 nm thick films, transmittances were increased from ~36 - 82% with

increasing annealing time as shown in Fig. 5.5 (b). In this case, the saturation level was also observed at 10 min of annealing. However, the comparable transmittance of Ag NPs prepared by using 10 nm thick films was decreased with respect to 5 nm thick films. This can be partially attributed to the increased mean diameter and density of Ag NPs. Both of the transmittance peaks obtained from the Ag NPs which were fabricated by using Ag films with thicknesses of 5 and 10 nm showed a redshift as well as broadened to the 400 - 600 nm wavelength regions. In the case of 20 min annealing, the observed transmittances were approximately 68 and 62% at wavelengths less than 560 nm, for Ag films with thicknesses of 5 and 10 nm, respectively. The decreases in transmittance are not linearly proportional to the volume of Ag NPs, suggesting that there are possibilities of increased reflectance due to the enhancement of surface roughness.

Figure 5.5: Transmittance spectra of Ag NPs prepared by using Ag films with thicknesses of (a) 5 and (b) 10 nm, after subtracting the contribution on ITO glass substrate. Adapted with permission from ref.[12] Copyright 2015, Japan Society of Applied Physics.

Figure 5.6 shows the reflectance spectra in percentage was obtained from the Ag NPs grown by using Ag films with thicknesses of 5 - 10 nm, subsequently annealed at 1 - 20 min. The samples displayed a dip in optical reflectance spectra corresponding to the LSPR of Ag NPs. In Fig. 5.6 (a), Ag NPs exhibited the reflectance ranged from 15 - 24%, at wavelength approximately 400 nm. The reflectances of the Ag NPs were enhanced with

increasing the annealing times within the window of 300 - 500 nm wavelengths. On the other hand, the reflectances decrease down to ~15% for lower annealing time, especially, 1 - 5 min. Between 500 - 800 nm wavelengths, the reflectances fluctuate around 20% because of interference effects from the surface.[33] In the case of 10 nm thick Ag film, the reflectances varied from ~21% - 34% at the wavelength around 400 nm as shown in Fig. 5.6(b). The highest intensity of reflectances was observed at 20 min of annealing; besides the lowest reflectance was for 1 min of annealing. This can be attributed to the enhancement of NPs size and, therefore, an increase of scattering which lead to increase the reflectance.

Figure 5.6: Reflectance spectra of Ag NPs prepared by using Ag films with thicknesses of (a) 5 and (b) 10 nm, after subtracting the contribution on ITO glass substrate. Adapted with permission from ref.[12] Copyright 2015, Japan Society of Applied Physics. .

Absorption spectra of Ag NPs were estimated from the measured reflectance and transmittance data as shown in Fig. 5.7. The percentage of absorption can be estimated by %A (λ) = 100% - %T (λ) - %R (λ).[34, 35] As can be seen in Fig. 5.7(a), the absorption of Ag NPs prepared by using Ag film with thickness of 5 nm, was significantly enhanced at ~ 620 nm wavelengths while a slight enhancement was observed in the NIR wavelength ranges. The absorption peaks were gradually redshifted, whereas the intensities of peaks decreased with increasing annealing time. The peaks shifted to the red could be ascribed to

the LSPR induced by the Ag NPs.[10, 36, 37] LSPR results in strong local EM fields with increasing the size of Ag NPs. When the size of Ag NPs increases, there are enhancements of not only EM fields but also scattering efficiencies. Higher scattering lead to a lower absorption of light. Therefore, the larger NPs tend to absorb less at shorter wavelengths, whereas the peaks in the absorption spectra showed a redshift and broadening gradually in the visible wavelength because of LSPR.[8,10,12,36-39] Figure 5.7(b) reveal the absorption spectra of Ag NPs prepared by using Ag films with thickness of 10 nm. The absorption peaks were increased gradually over a broad range of wavelength, where a strong peak was observed at ~ 640 nm wavelength. The absorption peaks shifted to the red and broadening as well as the intensity of peak decreased with increasing annealing time. The broadening and shifting of absorption peaks can be presumably attributed to the radiative damping of the resonances, as the scattering cross-section increase with increasing the size of Ag NPs. When the size of NPs increases, the surface roughness and penetration depth increase, which leading to increase in the absorption. In addition, quantum size effects and scattering within the NPs layer yielding an increased path of light would be the reasons for enhancement of optical absorption.
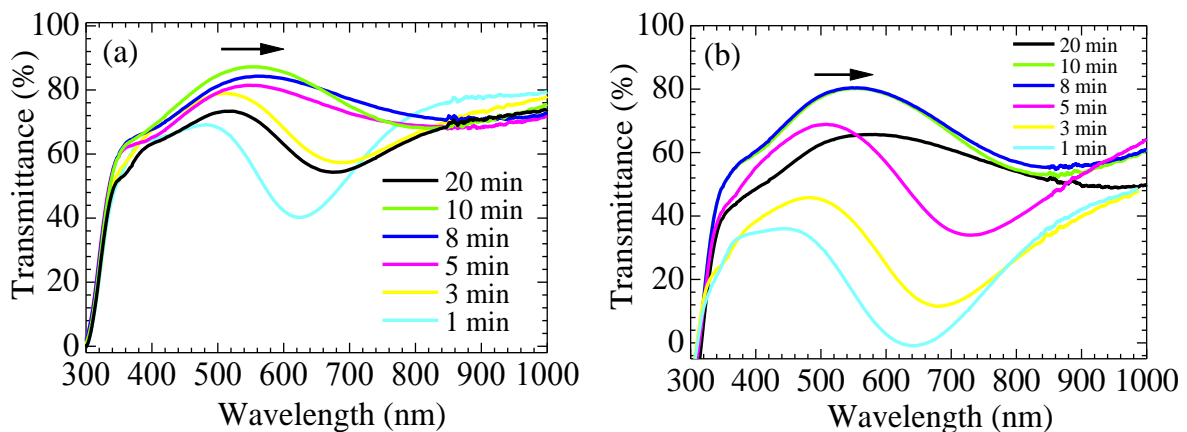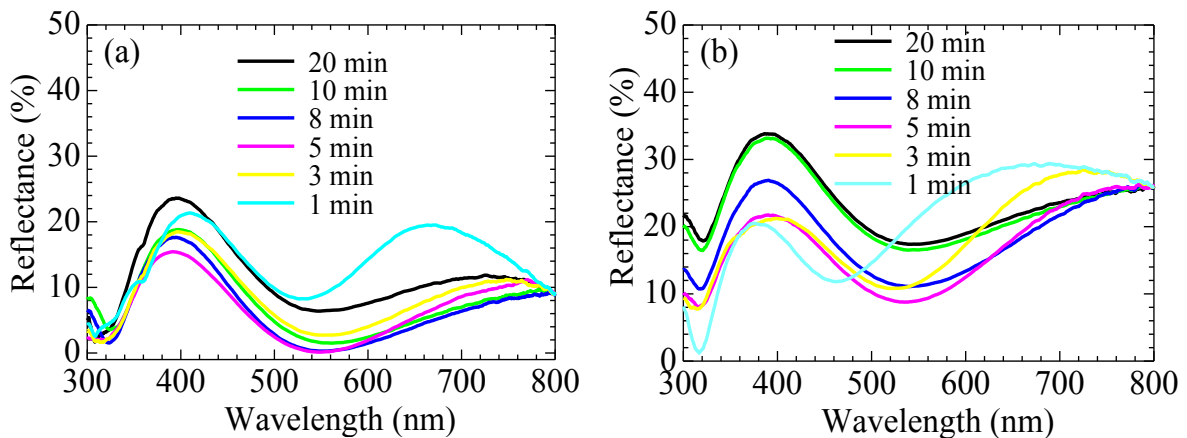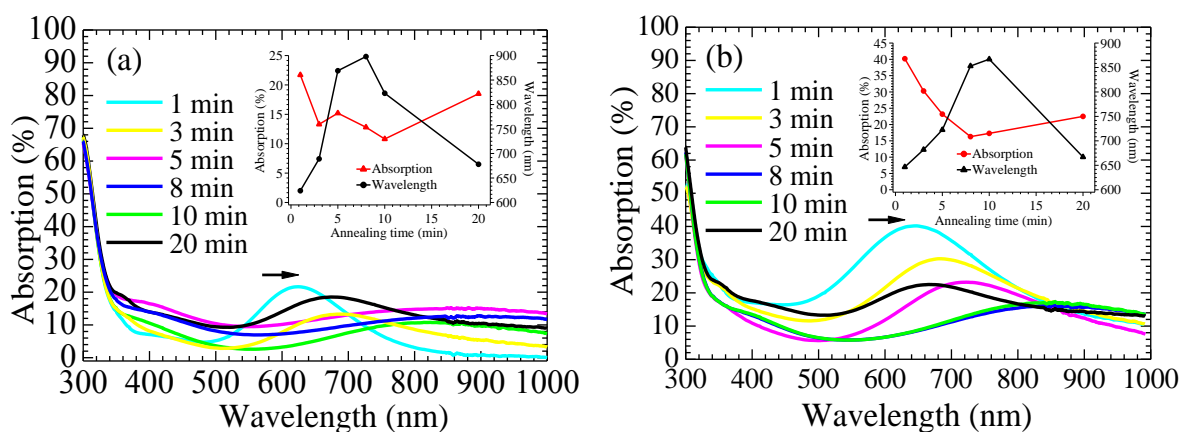

Figure 5.7: Absorption spectra of Ag NPs prepared by using Ag films with thicknesses of (a) 5 and (b) 10 nm, after subtracting the contribution on ITO glass substrate. Adapted with permission from ref.[12] Copyright 2015, Japan Society of Applied Physics.

Considering heat stability of FTO glass substrate as discussed in the previous section, the Ag NPs were prepared on FTO substrate for solar cells application. The corresponding absorption spectra are shown in Fig. 5.8. The peaks intensities were increased with increasing the thicknesses of Ag films as shown in Fig. 5.8 (a). As the size of NPs became larger by increasing thicknesses of Ag films, the absorptions were gradually increased over a broad range of wavelength ~ 400 -800 nm. In measured spectra, two distinct resonance peaks are clearly observed at wavelengths ~ 350 - 360 nm and 440 - 560 nm arise from the plasmon modes associated with the quadrupole and dipole in Ag NPs, respectively.[40] Also, the quadrupole and dipole plasmon resonances were enhanced and red-shifted with increasing the film thickness. However, the quadrupole resonance peak was not observed in case of 1 nm thick film and the dipole resonance peak began to decrease for 15 nm thick films. As it can be seen in Fig. 5.8 (b), the stronger dipole resonance peaks of Ag NPs were positioned at wavelengths of 446, 448, 486, 502, 510, 512, 531, 533 and 562 nm for NPs diameter sizes of 5, 15, 25, 40, 60, 90, 115, and 150 nm, respectively. It is reasonable that the red-shift in the LSPR peak occurs with increasing size of Ag NPs.
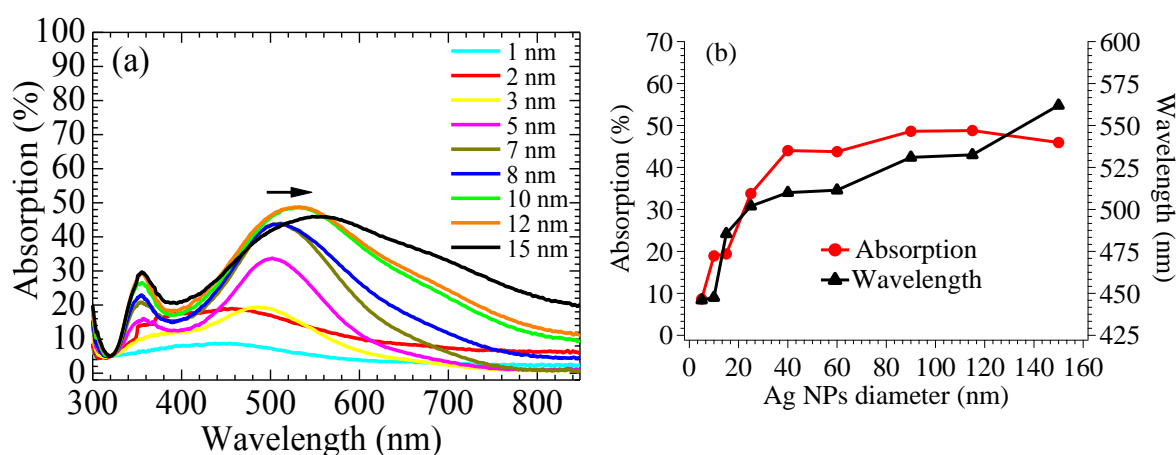
Figure 5.8: Absorption spectra of Ag NPs prepared on FTO glass substrate by using Ag films with thicknesses of (a) 1-15 nm, after subtracting the contribution on FTO/glass and (b) the effect of NPs sizes on absorption and wavelength.

5.4.4 Integration of silver nanoparticles to the perovskite solar cells

The detailed synthesis of ZnO NWs, $CH_3NH_3PbI_3$ perovskite and Ag NPs were discussed in chapters 3, 4 and 5, respectively. In short, to fabricate perovskite solar cells incorporating Ag NPs, ZnO NWs was grown on FTO substrates. Subsequently, the thin layer of Ag film of roughly 10 nm in thickness was deposited through PVD method. The layer was then thermally annealed in vacuum condition at 500 °C for 30 min. Once cooled, the filtered PbI_2-solution was spin-coated on FTO/ZnO NWs/Ag NPs layer at 2000 rpm for 15 s, and was subsequently dried in air for several minutes. The coated films were then dipped into a solution of CH_3NH_3I in 2-propanol at concentration of 10 mg mL^{-1} for 60 s and was left to dry for several minutes in air. The samples were then heated at 100 °C for 90 min under dark conditions. After cooling down to room temperature, the P3HT was dissolved in chlorobenzene at a concentration of 15 mg mL^{-1}, and was subsequently spin-coated onto the perovskite-coated substrate at a rate of 1500 rpm for 120 s. Finally, top Ag electrode around 120 nm thicknesses was thermally evaporated under high vacuum of 7×10^{-4} Pa, at a rate of ~ 0.1 nm s^{-1} to complete the solar cells. The solar cell architecture and a schematic view of Ag NPs on ZnO NWs are shown in Fig. 5.9.
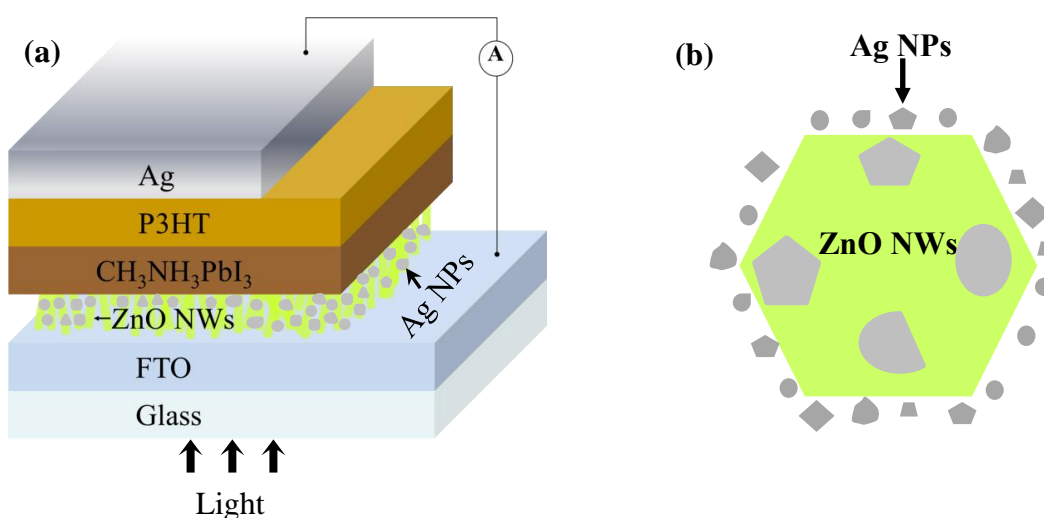
Figure 5.9: Schematic structure of (a) perovskite solar cell with Ag NPs incorporated in the ZnO NWs and (b) a schematic view of Ag NPs on ZnO NWs.

5.4.5 Effects of silver nanoparticles on perovskite solar cells

5.4.5.1 Analysis of optical absorption

Figure 5.10 shows the UV-vis absorption spectra of $CH_3NH_3PbI_3$ perovskite grown on FTO/ZnO NWs/Ag NPs and FTO/ZnO NWs samples. Absorption spectra of perovskite cover almost the visible to near infrared wavelength range of about 320 - 800 nm. By incorporating Ag NPs between the ZnO NWs and $CH_3NH_3PbI_3$ perovskite layer, a significant increase in optical absorbance was observed as it is shown in the Fig. 5.10.
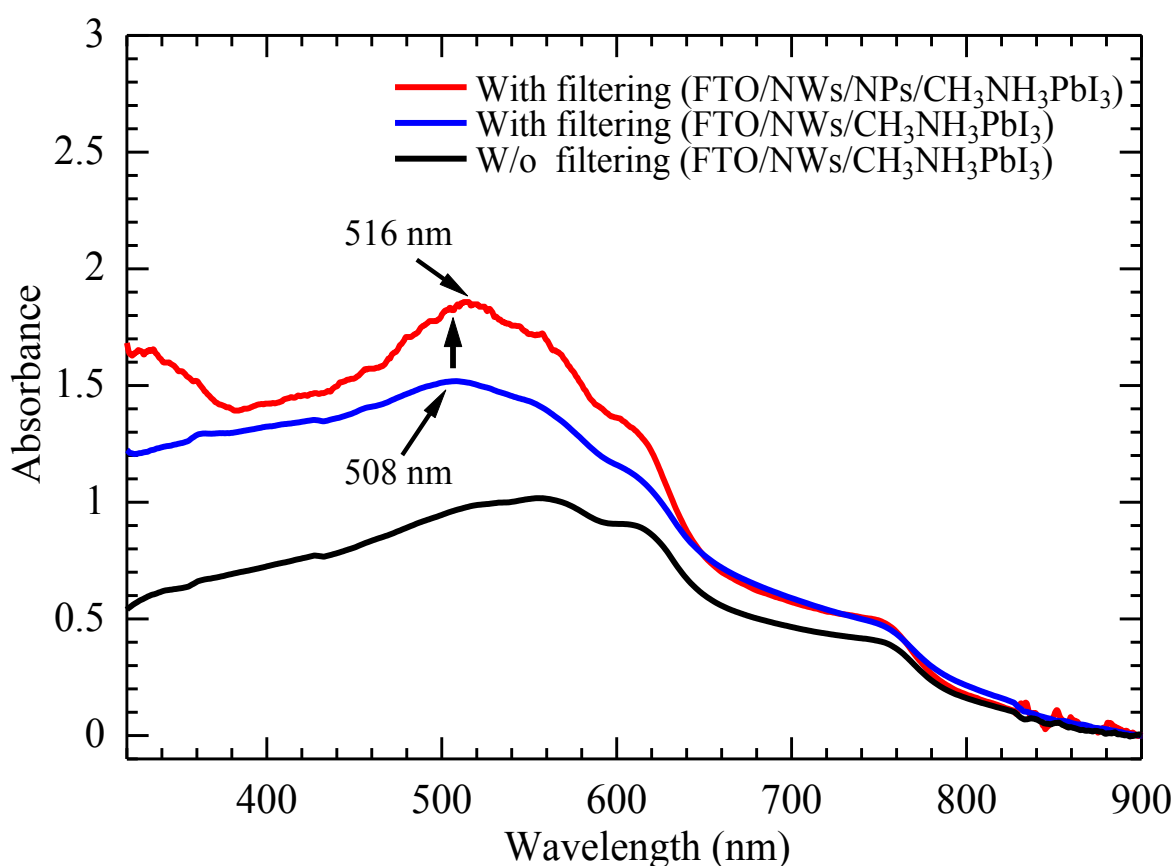
Figure 5.10: UV-vis absorption spectra of the $CH_3NH_3PbI_3$ perovskite material grown on FTO/ZnO NWs and FTO/ZnO NWs/Ag NPs samples by using filtered and non-filtered PbI_2-solutions. All measurements were carried out using an integrating sphere. Absorption of FTO/ ZnO NWs was subtracted for all samples and set the absorbance of 0 at 900 nm. The blue and black have been reprinted with permission from ref.[41] Copyright 2015, Japan Society of Applied Physics.

The absorption peak position shifts from 508 nm to a longer wavelength of 516 nm, due to the light trapping of LSPR mainly arises from Ag NPs. The increase of absorption could be attributed to the enhancement of electric field surrounding the NPs, together with the increase of light scattering also induced by LSPR, which increased the optical path length. It also agrees with the earlier reported investigations on plasmon-enhanced perovskite absorption.[25] This result persuades the plasmonic effects of the Ag NPs, and their effectiveness of boosting light harvesting in perovskite solar cells.

5.4.5.2 Photovoltaic performance measurement

To investigate the effect of Ag NPs on solar cell performance, I compare the PCE of plasmon-enhanced perovskite solar cell with Ag NPs and the perovskite solar cells with only ZnO NWs as photoanodes. Again, the perovskite solar cell prepared by using non-filtered PbI_2-solution is presented due to realize the overall performances of these devices. Figure 5.11 shows the *J-V* characteristics of the best-performance three types of perovskite solar cells. The *J-V* curves were obtained under AM1.5G (100 mW cm^{-2}) illumination, and figured out the V_{OC}, J_{SC}, *FF*, and PCE for these solar cells. From the Fig. 5.11, one can clearly observe the V_{OC} and J_{SC} of the plasmon-enhanced perovskite solar cell with Ag NPs are increased significantly, compared with the other two kinds of solar cells in this study. The increase of J_{SC} can be attributed to the enhancement of optical absorption which is resulted from the LSP effect. Therefore, it can be concluded that incorporation of Ag NPs has improved the device performance by increasing the photocurrent. Zhang *et al.*[42] reported that the origin of the improved J_{SC} would be the enhancement of generation of free charge carriers with the incorporation of metal NPs in the perovskite solar cell. The improvement of V_{OC} can be due to the elimination of charge recombination in the existence

of Ag NPs. For an ideal p-n junction, V_{OC} can be given by $V_{OC} = \dfrac{kT}{q} \ln \left(\dfrac{I_{ph}}{I_s} \right) + 1$, where k

is the Boltzmann constant, T is the temperature, q is the electronic charge, I_{ph} is the

photocurrent, and I_s the diode saturation current. The V_{OC} depend on I_{ph} and I_s, while the I_s

depend on recombination. Thus, V_{OC} then measure the amount of recombination. Lu *et*

al.[25] reported also the enhancement of V_{OC} should be due to the suppression of charge

recombination because the faster charge transfer to the presence of Ag NPs in the

perovskite solar cell was observed through the steady-state and transient PL

measurements.
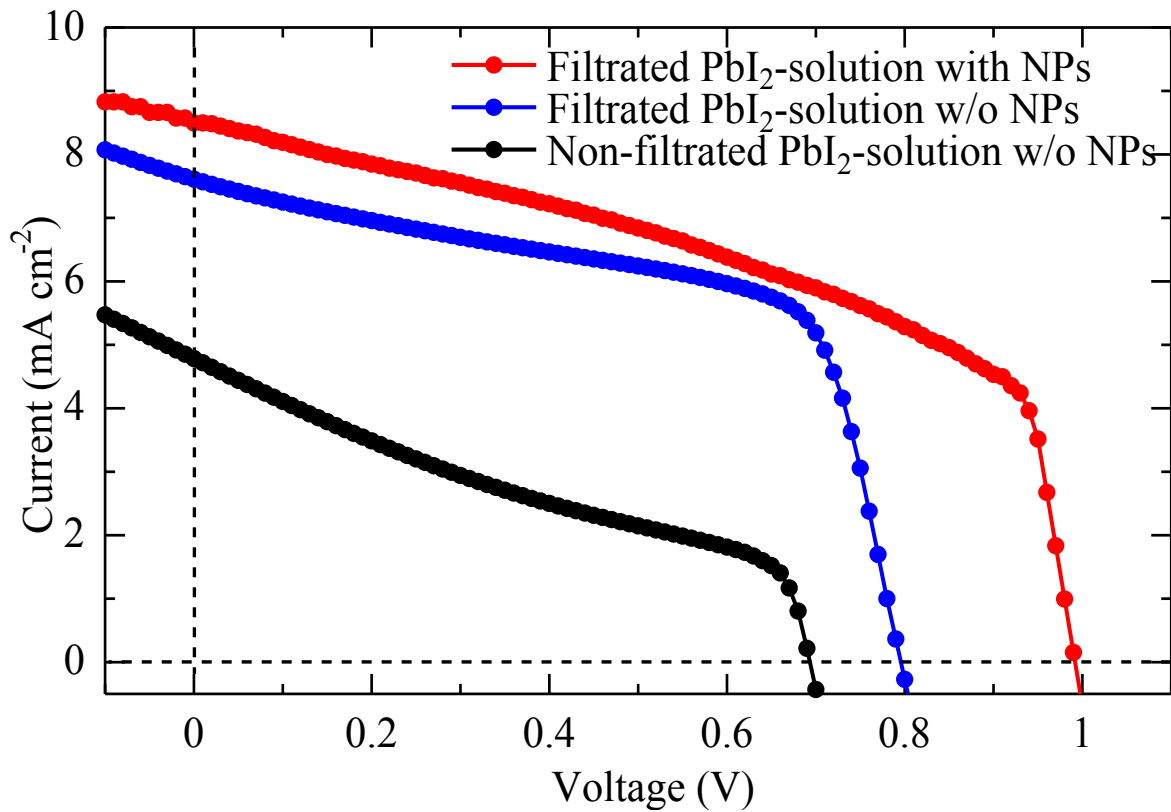
Figure 5.11: Representative *J-V* characteristics of the best-performance perovskite solar

cell with and without Ag NPs as well as without filtered PbI$_2$-solution. The blue and black

curves have been reprinted with permission from ref.[41] Copyright 2015, Japan Society of

Applied Physics.

Figure 5.12 displays the performance parameters of the solar cells obtained from above mentioned *J-V* curves. It is clearly observed that both of V_{OC} and J_{SC} are increased after the Ag NPs were incorporated into the solar cell, and thereby leading to an enhanced PCE. For the NPs-free with filtered PbI$_2$-solution case, the value of V_{OC} and J_{SC} are 0.79V and 7.6 mA cm^{-2}, and for the NPs-incorporated case (plasmon-enhanced perovskite solar cell), the value increases to 1.02 V and 8.5 mA cm^{-2}, respectively. However, the value of *FF* for the NPs-incorporated case is lower than the NPs-free cases that are 0.49 and 0.63, respectively. The low *FF* could be attributed to the high series resistance, or low shunt resistance.[43,44] The solar cell prepared by using non-filtered PbI$_2$-solution showed a maximum PCE of 1.4%, whereas the filtered PbI$_2$-solution without NPs and NPs-incorporated devices exhibited the maximum PCE of 4.8% and 5.4%, respectively.
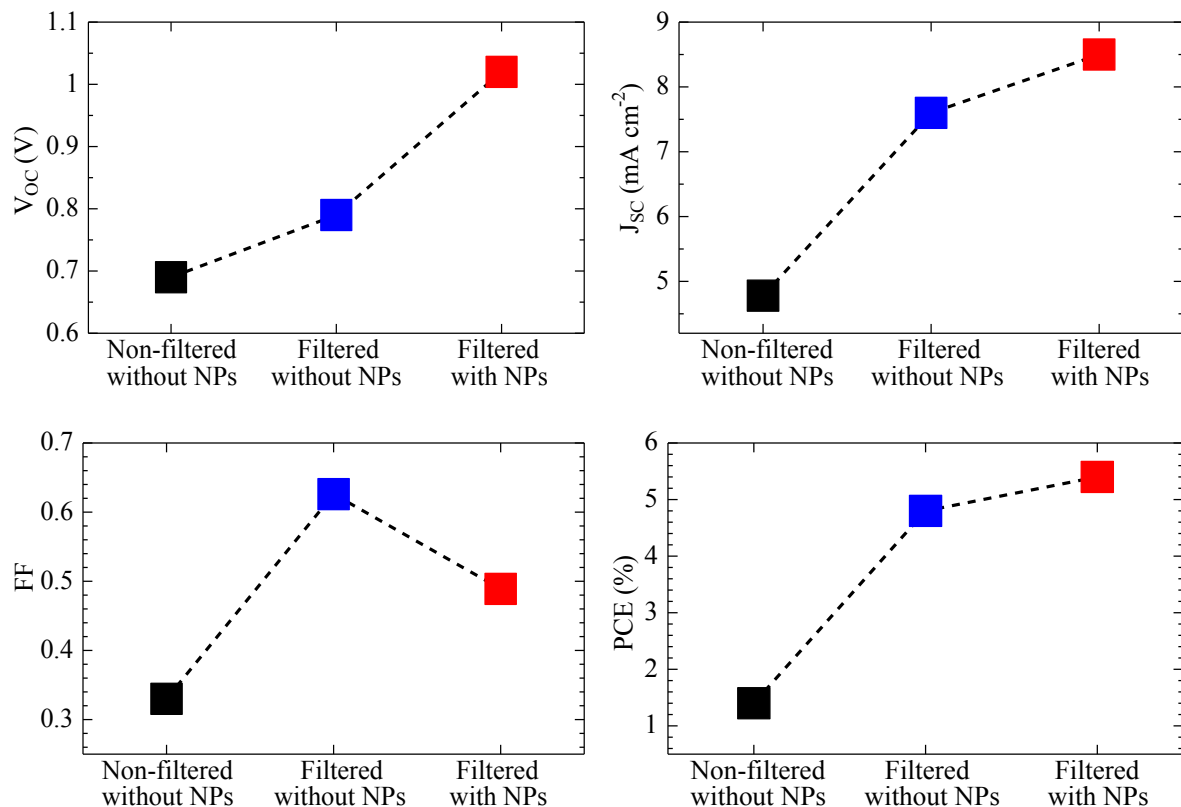
Figure 5.12: Effect of Ag NPs on the performance of perovskite solar cells (red: device with filtered PbI$_2$-solution and with Ag NPs; Blue: with filtered PbI$_2$-solution and without Ag NPs; black: without filtered PbI$_2$-solution and without Ag NPs).

5.5 CHAPTER SUMMARY

In summary, the Ag NPs have been fabricated by using the PVD method followed by thermal annealing that is very simple and controllable. The size, shape and density of the Ag NPs can be regulated through the different annealing times and thickness of Ag films. The optimum thickness was observed at ~10 nm, which displayed the most uniform distributions of NPs and the enhanced resonance peaks in the absorption spectra shifted to the red were confirmed by the FE-SEM and the UV-vis absorption spectroscopy, respectively. All these facts suggest that the absorption peaks may arise from the LSPR of Ag NPs. These unique properties of Ag NPs generate them exceptional candidates for further applications in LSP enhanced solar cells. I therefore expect that the application of Ag NPs would help to improve the PCE of plasmon enhanced solar cells through the enhancement of light harvesting efficiency.

I demonstrated a general approach to employing Ag NPs to improve the PCE of ZnO NWs based perovskite solar cells. As initially designed, I would anticipate to be able to ascribe the improvement in enhanced J_{SC} to enhanced light harvesting through the plasmonic light interactions in the Ag NPs. I carefully measured the light absorption in perovskite layer, however, no significant broadband enhancement of light absorption was observed. By incorporating Ag NPs into the ZnO NWs photoanodes, the perovskite solar cell exhibited a significantly enhanced J_{SC} and PCE of 5.4% by 1.125 times, as compared to the NPs-free device fabricated by using filtered PbI_2-solution which showed a maximum PCE of 4.8%. The improvement of J_{SC} can be ascribed to the plasmonic enhancement of light absorbance and possible facilitation of exciton dissociation,[45] and or the enhancement of free charge-carriers generated in the perovskite solar cell.[42] This method has the advantages of suppressing charge recombination, which lead to higher V_{OC}, and

enhanced optical path length because of light-scattering centers effect of NPs giving higher J_{SC} in the perovskite solar cell.

I believe that the significances of this study will guide the research in utilizing LSPs to improve solar cell performance by optimizing the absorption, hence improving electron collection and PCE. This approach also enables the application of LSPs in other photovoltaics such as quantum dot-sensitized solar cells, organic solar cells, and organic hybrid solar cells that require efficient light harvesting and suppressed recombination. I do note, however, that further research is required to fully realize the mechanism which is leading the enhanced solar cell performance.

References

[1]   C. L. Haynes and R. P. Van Duyne, J. Phys. Chem. B **105**, 5599-5611 (2001).

[2]   U. Kreibig, Optics of nanosized metals. In: *Handbook of Optical Properties*. RE Hummel, P Wissmann (Eds), CRC Press, FL, USA, 145-190 (1997).

[3]   P. Mulvaney, Langmuir, 12, 788-800 (1996).

[4]   S. Link and M. A. El-Sayed, J. Phys. Chem. B **103**, 8410-8426 (1999).

[5]   C. F. Bohren and D. R. Huffman (Eds), *Absorption and Scattering of Light by Small Particles*. John Wiley and Sons, NY, USA (1983).

[6]   S. Eustis and M. A. El-Sayed, Chem. Soc. Rev. **35**, 209-217 (2006).

[7]   A. J. Haes, W. P. Hall, L. Chang, W. L. Klein and R. P. Van Duyne, Nano Lett. **4**, 1029-1034 (2004).

[8]   E. Hutter and J. H. Fendler, Adv. Mater. **16**, 1685 (2004).

[9]   D. M. Schaadt, B. Feng and E. T. Yu, Appl. Phys. Lett. **86**, 063106 (2005).

[10] K. L. Kelly, E. Coronado, L. L. Zhao and G. C. Schatz, J. Phys. Chem. B **107**, 668-677 (2003).

[11] D. D. Evanoff and G. Chumanov, J. Phys. Chem. B **108**, 13957-13962 (2004).

[12] M. M. Rahman, N. Hattori, Y. Nakagawa, X. Lin, S. Yagai, M. Sakai, K. Kudo and K. Yamamoto, Jpn. J. Appl. Phys. **53**, 11RE01 (2014).

[13] A. J. Haes and R. P. Van Duyne, J. Am. Chem. Soc. **124**, 10596 (2002).

[14] A. D. McFarland and R. P. Van Duyne, Nano Lett. **3**, 1057 (2003).

[15] K. G. Stamplecoskie, J. C. Scaiano, V. S. Tiwari and H. Ananoislands, J. Phys. Chem. C **115**, 1403 (2011).

[16] C. Wen, K. Ishikawa, M. Kishima and K. Yamada, Sol. Energy Mater. Sol. Cells **61**, 339-351 (2000).

[17] W. J. Yoon, K. Y. Jung, J. Liu, T. Duraisamy, R. Revur, F. L. Teixeira, S. Sengupta and P. R. Berger, Sol. Energy Mater. Sol. Cells **94**, 128-132 (2010).

[18] M. K. Gangishetty, K. E. Lee, R. W. J. Scott and T. L. Kelly, ACS Appl. Mater. Interfaces **5**, 11044 (2013).

[19] Q. Xu, F. Liu, Y. Liu, K. Cui, X. Feng, W. Zhang and Y. Huang, Scientific Report **3**, 2112 (2013).

[20] M. Enomoto, K. Taniguchi and M. Ihara, ECS Trans. **25**, 37-48 (2010).

[21] H. A. Atwater and A. Polman, Nature Mater. **9**, 205 (2010).

[22] S. Sun, T. Salim, N. Mathews, M. Duchamp, C. Boothroyd, G. Xing, T. C. Sum and Y. M. Lam, Energy Environ. Sci. **7**, 399-407 (2014).

[23] T. Miyasaka, Chem. Lett. 44, 720-729 (2015).

[24] S. Kazim, M. K. Nazeeruddin, M. Grätzel and S. Ahmad, Angew. Chem. Int. Ed. **53**, 2812-2824 (2014).

[25] Z. Lu, X. Pan, Y. Ma, Y. Li, L. Zheng, D. Zhang, Q. Xu, Z. Chen, S. Wang, B. Qu, F. Liu, Y. Huang, L. Xiao and Q. Gong, RSC Adv. **5**, 11175-11179 (2015).

[26] G. Q. Yu, B. K. Tay, Z. W. Zhao, X. W. Sun and Y. Q. Fu, Physica E **27**, 362 (2005).

[27] G. Sandmann, H. Dietz and W. Plieth, J. Electroanal. Chem. **491**, 78 (2000).

[28] L. Miao, Y. Ina, S. Tanemura, T. Jiang, M. Tanemura, K. Kaneko, S. Toh and Y. Mori, Surf. Sci. **601**, 2792 (2007).

[29] N. Félidj, J. Aubard, G. Lévi, J. R. Krenn, M. Salerno, G. Schider, B. Lamprecht, A. Leitner and F. R. Aussenegg, Phys. Rev. B **65**, 075419 (2002).

[30] W. A. Weimer and M. J. Dyer, Appl. Phys. Lett. **79**, 3164 (2001).

[31] A. Hebeish, M. H. El-Rafie, M. A. El-Sheikh and M. E. El-Naggar, J. Nanotechnol. **2013**, 201057 (2013).

[32] M. J. Hammersley. In: *Handbook of Near-Infrared Analysis*. Practical Spectroscopy Series, D. A. Burns and E. W. Ciurczak (Eds), Marcel Dekker, New York, USA, 13, 475-494 (1992).

[33] Y. J. Lee, D. S. Ruby, D. W. Peters, B. B. McKenzie and J. W. P. Hsu, Nano Lett. **8**, 1501-1505 (2008).

[34] M. F. Cansizoglu, R. Engelken, H. W. Seo and T. Karabacak, ACS Nano **4**, 733 (2010).

[35] Y. H. Ko and J. S. Yu, Phys. Status Solidi A **208**, 2778 (2011).

[36] K. C. Lee, S. J. Lin, C. H. Lin, C. S. Tsai and Y. J. Lu, Surf. Coat. Technol. **202**, 5339-5342 (2008).

[37] H. Lu, X. Xu, L. Lu, M. Gong and Y. Liu, J. Phys.: Condens. Matter. **20**, 472202 (2008).

[38] Y. Lin, X. Q. Liu , T. Wang, C. Chen, H. Wu, L. Liao and C. Liu, Nanotechnology **24**, 125705 (2013).

[39] F. Mafuné, J.-y. Kohno, Y. Takeda and T. Kondow, J. Phys. Chem. B **104**, 9111-9117 (2000).

[40] B. H. Choi, H. H. Lee, S. M. Jin, S. K. Chung and S. H. Kim, Nanotechnology **18**, 075706 (2007).

[41] M. M. Rahman, N. Uekawa, F. Shiba, Y. Okawa, M. Sakai, K. Yamamoto, K. Kudo and T. Konanoislandshi, Jpn. J. Appl. Phys. **55**, 01AE09 (2015).

[42] W. Zhang, M. Saliba, S. D. Stranks, Y. Sun, X. Shi, U. Wiesner and H. J. Snaith, Nano Lett. **13**, 4505-4510 (2013).

[43] A. Kumar, S. Sista and Y. Yanga, J. Appl. Phys. **105**, 094512 (2009).

[44] B. Tremolet de Villers, C. J. Tassone, S. H. Tolbert and B. J. Schwartz, J. Phys. Chem. C **113**, 18978-18982 (2009).

[45] T. Kawawaki, H. Wang, T. Kubo, K. Saito, J. Nakazaki, H. Segawa and T. Tatsuma, ACS Nano **9**, 4165-4172 (2015).

CHAPTER SIX

Conclusions and Future Work

6.1 CONCLUSIONS

The studies discussed in this dissertation aimed to synthesize, characterize and optimize the ZnO NWs, $CH_3NH_3PbI_3$ perovskite and metallic Ag NPs for organic-inorganic perovskite solar cells applications. For achieving these targets and appropriately development of perovskite solar cells as well as their possible further improvement in PCE, I pursued three different strategies: the use of high crystalline ZnO NWs due to high charge-collection efficiency, the filtration of PbI_2-solution due to achieve a homogeneous and uniform perovskite light-absorber, and the application of plasmonic Ag NPs for optical absorption enhancement yielding a higher performance of the device.

From this point of view, primary emphasis was given to achieve high crystalline ZnO NWs by catalyst-free. In chapter 3, the growth and characterizations of ZnO NWs have been presented in detail. ZnO NWs were grown on FTO substrate without the presence of any catalysts through the RE method which has several controllable parameters including T_{cru} of the Zn source, T_{sub}, t_{gro} and P_{oxy} in the vacuum chamber. By adjusting the T_{sub} and t_{gro} parameters while have the other parameters remained constant during the growth process, parametric investigations of the effects of controllable factors on morphology of the ZnO NWs have been conducted. Furthermore, morphological effects of ZnO NWs were investigated on various samples prepared through different thickness of Ag films and P_{oxy}, while the T_{sub} and t_{gro} were kept at 500 °C and 30 min, respectively. In order to characterize the morphology, structures and phase of ZnO NWs, the FE-SEM, EDX, TEM, XRD and PL measurements have been carried out. In this study, optimal growth of ZnO NWs were observed at T_{sub} of 500 °C and with a t_{gro} of 30 min by keeping T_{cru} to 400 °C and P_{oxy} to 3.9×10^{-2} Pa. Under this condition, the obtained length and diameter of the NWs are around 310 nm and 46 nm, respectively. The ZnO NWs possess high-crystalline nature, singly oriented without NW-NW junctions or network-like morphology.

Conversely, Ag-assisted growth exhibits higher length and diameter of ZnO NWs which are interconnected to each other and form NW-NW junctions, resulting in a different morphology compared with bare substrate or catalyst-free growth. ZnO NWs with NW-NW junction or network-like morphology cause junction resistance which is the dominating factor affecting charge transport. Thus, it is expected that the highly-crystalline, catalyst-free ZnO NWs would be favorable for efficient charge transport in the perovskite solar cells.

In chapter 4, growth and characterization of organic-inorganic perovskite materials and their application in ZnO NWs based solar cells have been presented. Formation of CH_3NH_3I, $CH_3NH_3PbI_3$ and P3HT layers were performed under ambient conditions because of simplicity and low-cost processing technique. The perovskite formation was occurred within seconds after dipping the PbI_2 samples into CH_3NH_3I solution and their color was changed immediately from yellow to black due to the size effect and or an increased density of perovskite crystal. FE-SEM was employed to observe the $CH_3NH_3PbI_3$ morphology. From the FE-SEM results, I conclude that the filtration of PbI_2-solution has an enormous influence on morphology of perovskite. In the case of filtered PbI_2-solution, $CH_3NH_3PbI_3$ film displayed relatively homogeneous and uniform surface, while it was non-uniform and fiber-like structure with voids results in a poor surface coverage for the non-filtered PbI_2-solution cases. Using XRD spectroscopy it was determined that the conversion of PbI_2 into $CH_3NH_3PbI_3$ layer is partial: a large portion of unreacted PbI_2 remained in both cases. An important finding was that only filtered PbI_2-solution changes the morphology and structure of $CH_3NH_3PbI_3$ film can have an immense effect on PCE of the solar cells. The studies displayed herein revealed the importance of filtration of PbI_2 solution on their performance in organic-inorganic perovskite solar cells. To sum up, a two-step deposition method was used for fabrication of ZnO NWs based

perovskite solar cells. I obtained a PCE of 4.8% for a best performing device. Despite the significant effect of filtration of PbI_2-solution, the obtained PCE of solar cell remains low compare to presently reported value. Future studies should emphasis on absorption enhancement induced by plasmonic NPs and their physics in the plasmonic-enhanced solar cells, which will expand the way to generate high-performance perovskite solar cells.

Further boosting the PCE of the solar cells, plasmonic NPs were incorporated into the ZnO NWs based perovskite solar cells presented in detail, in chapter 5. For plasmonic NPs fabrication, Ag films of several nm thick layers were deposited by using PVD method followed by thermal annealing. The size, shape and density of the Ag NPs were controlled by setting different annealing times and the thickness of Ag films. The FE-SEM data revealed that the film thickness of ~ 10 nm formed the most uniform size and distributions of NPs. Using UV-vis absorption spectroscopy it was evidenced that the LSPR peaks in the absorption spectra were highly enhanced and redshifted by using these NPs. The same NPs were applied into solar cells. I carefully measured the light absorption in perovskite layer, however, no significant broadband enhancement was observed. By incorporating Ag NPs into the ZnO NWs photoanodes, the perovskite solar cell exhibited a significantly enhanced J_{SC} and PCE of 5.4% by 1.125 times, as compared to the NPs-free device fabricated by using filtered PbI_2-solution. The improvement of J_{SC} can be ascribed to the plasmonic enhancement of light absorbance and possible facilitation of exciton dissociation and or the enhancement of free charge-carriers generated in the perovskite solar cell. This method has advantages of suppressing charge recombination, which lead to higher V_{OC}, and enhanced optical path length because of light-scattering centers effect of NPs giving higher J_{SC} in the perovskite solar cell. I do note, however, that further research is required to fully realize the mechanism and optimization of different layers in the cell which is leading the enhanced solar cell performance.

6.2 FUTURE WORK

I have studied ZnO NWs, Ag NPs, filtration effect of PbI_2 solution and their application in perovskite solar cells. Although an increased PCE was achieved, filtration of PbI_2-solution could results in much higher performance increase since the morphology and structure of $CH_3NH_3PbI_3$ film from filtered PbI_2-solution is more uniform than that from non-filtered PbI_2-solution ones. Since the morphology is a crucial issue in $CH_3NH_3PbI_3$ perovskite solar cells. In addition to filtration approach, it would be crucially important to optimize the morphology of perovskite layer by varying processing conditions, concentrations of perovskite solution, the rate of spin-coating, annealing temperature and time as reported recently.

As I demonstrated the successful application of Ag NPs in perovskite solar cells, this approach could also be implemented in other photovoltaics such as quantum dot-sensitized solar cells, organic solar cells, and organic hybrid solar cells that require efficient light harvesting and suppressed recombination. Although many of the issues achieved in this dissertation are proof of plasmonic enhancement, significant broadband enhancement of light absorption was not observed. Based on this, future work would be involved in an investigation of the optimum NPs size, shape and surface coverage of plasmonic NPs.

Environmental safety and commercialization are the top issues of perovskite solar cells. The use of Pb will generate heavy metal pollution and therefore, it should be avoided by any means. The high efficient perovskite solar cell without Pb is a hot topic for research. For real application, stability of perovskite is another key issue and is easily affected by its surrounding atmosphere. High stability would be obtained by optimizing the materials and structures of cells. There are limited researches on this issue. Highly stable and high-performance perovskite solar cells are just at near future.

CURRICULUM VITAE

CURRICULUM VITAE

Md. Mijanur Rahman

Date of birth: December 10, 1979

Place of Birth: Barisal, Bangladesh

Nationality: Bengali

Languages: Bengali (native), English and Japanese (fluent)

Education

10/2012	Doctor of Philosophy (Ph.D)
-	Department of Nanomaterial Science,
03/2016:	Graduate School of Advanced Integration Science, Chiba University, Japan
	Thesis Title: Synthesis and characterization of zinc oxide nanowires and silver nanoparticles for perovskite solar cells application.
	Supervisor and co-supervisor: Prof. Dr. Takehisa KONISHI and
	Prof. Dr. Kazuhiro KUDO
10/2010	Master of Engineering
-	Department of Nanomaterial Science,
09/2012:	Graduate School of Advanced Integration Science, Chiba University, Japan
	Thesis: Carrier blocking nature of an operating organic light-emitting diode.
04/2007	Master of Science
-	Department of Earth Science (Specialized in Remote Sensing)
03/2009:	Graduate School of Science, Chiba University, Japan
	Thesis: Extraction of mangrove forest in Bangladesh using Landsat data.

07/1998	Bachelor of Urban and Rural Planning (BURP)
-	School of Science, Engineering and Technology,
10/2003:	Khulna University, Bangladesh

Teaching and research experience

| 09/2013 - 03/2014: | Research assistant |
| | Global Center-of-Excellence, Chiba University, Japan. |

| 04/2011 - 03/2012: | Teaching assistant |
| | Center for Frontier Science, Chiba University, Japan. |

| 10/2010 - 03/2011: | Research assistant |
| | Center for Frontier Science, Chiba University, Japan. |

Awards & Scholarships

| 10/2012 - 09/2015: | Japanese Government (Monbukagakusho: MEXT) Scholarship awarded for Ph.D course study |

| 03/2011 - 09/2012: | Japanese Government (Monbukagakusho: MEXT) Scholarship awarded for Master course study |

| 09/2011: | Japan Student Service Organization (JASSO) Student Exchange Support Program, scholarship awarded for attending the KOSMOS Summer University 2011, Frontiers of Organic/ Inorganic Hybrid Materials for Electronics and Optoelectronics, Humboldt-Universität zu Berlin-IRIS Adlershof, Germany, 2011. |

04/2008 - 03/2010: Mitsubishi Corporation Scholarship for International Students, Japan, awarded for Master course study

1994 - 1996: Merit Scholarship (Board of Intermediate and Secondary Education, Jessore) awarded by the Government of the People's Republic of Bangladesh due to excellent result in Secondary School Certificate (SSC) Examination.

Research funding

2013 - 2014: Outstanding Graduate COE Support Subsidy program of MEXT (Advanced School for Organic Electronics), Chiba University.

0.55 Million Yen.

2012 - 2013: Global Center-of-Excellence (G-COE) Grant for Doctoral Students. Advanced School of Organic Electronics, Chiba University.

0.45 Million Yen.

Membership of professional organizations

[1]   The Japan Society of Applied Physics (JSAP)

[2]   The Institute Electronics, Information and Communication Engineers (IEICE)

List of scientific publications

Peer-reviewed Journals and Proceedings

[1] **Md. Mijanur Rahman** *et al*., Investigations on nanoscale morphological changes and characterization of zinc oxide nanostructures prepared through reactive evaporation method (in preparation).

[2] **Md. Mijanur Rahman**, Naofumi Uekawa, Fumiyuki Shiba, Yusuke Okawa, Masatoshi Sakai, Kazunuki Yamamoto, Kazuhiro Kudo and Takehisa Konishi, Effect of the filtration of PbI_2 solution for zinc oxide nanowire based perovskite solar cells, Japanese Journal of Applied Physics, **55**, 01AE09 (2015).

[3] **Md. Mijanur Rahman**, Nampei Hattori, Yuta Nakagawa, Xu Lin, Shiki Yagai, Masatoshi Sakai, Kazuhiro Kudo and Kazunuki Yamamoto, Preparation and characterization of silver nanoparticles on localized surface plasmon-enhanced optical absorption, Japanese Journal of Applied Physics, **53**, 11RE01 (2014).

[4] **Md. Mijanur Rahman**, Naoki Ogawa and Yukimasa Miyazaki, Yasuo Nakayama, Yutaka Noguchi and Hisao Ishii, Time-Of-Flight Technique to Examine Carrier Blocking Nature in Organic Light Emitting Diode, e-Journal of Surface Science and Nanotechnology, **10**, 315 - 320 (2012).

[5] **Md. Mijanur Rahman,** Naoki Ogawa, Yasuo Nakayama, Yutaka Noguchi and Hisao Ishii, Time-Of-Flight Measurement as a Tool to Investigate the Hole Blocking Nature of an Operating Organic Light-Emitting Diode, IEEE/OSA/IAPR International Conference on Informatics, Electronics & Vision (ICIEV), 978-1-4673-1154-0/12 IEEE (2012).

International conference presentations

[1] **Md. Mijanur Rahman**, Yuta Nakagawa, Fumiyuki Shiba, Yusuke Okawa, Naofumi Uekawa, Masatoshi Sakai, Kazuhiro Kudo and Kazunuki Yamamoto, Plasmonic effect of ZnO nanowires based solid-state sensitized hybrid perovskite $CH_3NH_3PbI_3$ solar cell, *The 7th International Symposium on Advanced Plasma Science and its Applications for Nitrides and Nanomaterials /8th International Conference on Plasma-Nano Technology & Science,* Nagoya, Japan, March 26th - 31th, 2015.

[2] **Md. Mijanur Rahman**, Yuta Nakagawa, Naofumi Uekawa, Fumiyuki Shiba, Yusuke Okawa, Masatoshi Sakai, Kazuhiro Kudo and Kazunuki Yamamoto, Organic-inorganic hybrid perovskite $CH_3NH_3PbI_3$ processed in air for ZnO nanowires based solid-state sensitized solar cell applications, *The 10th International Conference on Nano-Molecular Electronics (ICNME 2014)*, Kobe, Japan, December 17th - 19th, 2014.

[3] **Md. Mijanur Rahman**, Ryudai Tanaka, Xu Lin, Masatoshi Sakai, Shiki Yagai, Kazuhiro Kudo and Kazunuki Yamamoto, Fabrication of silver nano-islands with zinc oxide nanowires based photoanode suitable for photoabsorption-enhancement of dye-sensitized solar cells, *The 6th International Symposium on Advanced Plasma Science and its Applications for Nitrides and Nanomaterials /7th International Conference on Plasma-Nano Technology & Science,* Nagoya, Japan, March 2th - 6th, 2014.

[4] **Md. Mijanur Rahman**, Ryudai Tanaka, Kota Machida, Shiki Yagai, Kazuhiro Kudo and Kazunuki Yamamoto, Effect of Silver Nanoparticles on Optical Absorption Enhancement Suitable for ZnO Nanowires based Dye-Sensitized Solar Cells, *The 12th International Conference on Atomically Controlled Surfaces, Interfaces and Nanostructures in conjunction with 21st International Colloquium on Scanning Probe Microscopy*, Tsukuba, Japan, November 4th - 8th, 2013.

[5] **Md. Mijanur Rahman**, Shinji Kouya, Jun Osawa, Masatoshi Sakai, Kazunuki Yamamoto and Kazuhiro Kudo, Fabrication of ZnO nanorod structures for high-efficiency solid-sate dye-sensitized solar cells, *The 10th International Conference on Nano-Molecular Electronics (ICNME 2012)*, Hyogo, Japan, December 12th - 14th, 2012.

[6] **Md. Mijanur Rahman**, Naoki Ogawa, Yukimasa Miyazaki, Yasuo Nakayama, Yutaka Noguchi and Hisao Ishii, Carrier Blocking Nature in Organic Light Emitting Diode Studied by Displacement Current Measurement and Time-Of-Flight Method, *The 6th International Symposium on Surface Science and Nanotechnology (ISSS-6)*, Tokyo, Japan, December 11th - 15th, 2011.

Domestic conference presentations

[1] Shinji Kouya, Jun Osawa, **Md. Mijanur Rahman**, Hiroshi Yamauchi, Shigekazu Kuniyoshi, Masatoshi Sakai, Masaaki Iizuka, Yasuyuki Watanabe and Kazuhiro Kudo, Fabrication of dye-sensitized solar cell photoanode by low temperature process, *The 60th spring meeting 2013, Japan Society of Applied Physics (JSAP)*, Kanagawa, Japan, March 27th - 30th , 2013.

[2] **Md. Mijanur Rahman**, Yukimasa Miyazaki, Yasuo Nakayama, Yutaka Noguchi and Hisao Ishii, Time-Of-Flight Measurement of an Operating Organic Light-Emitting Diode as a Tool to Investigate Carrier Behavior, *The 59th spring meeting 2012, Japan Society of Applied Physics (JSAP)*, Tokyo, March 15th - 18th , 2012.

Other publications of previous study (Remote Sensing)

<u>**Peer-reviewed Journal**</u>

[1] **Md. Mijanur Rahman**, Md. Rahmat Ullah, Mi Lan, Josaphat Tetuko Sri Sumantyo, Hiroaki Kuze and Ryutaro Tateishi, Comparison of Landsat image classification methods for detecting mangrove forests in Sundarbans, International Journal of Remote sensing, **34**, 4, 1041 - 1056 (2012).

<u>**International conference presentations**</u>

[1] **Md. Mijanur Rahman**, Josaphat Tetuko Sri Sumantyo and Hiroaki Kuze, Application of Remote sensing for major urban area change analysis in Bangladesh, *The 15th CEReS International Symposium on Remote Sensing*, Chiba, Japan, December 15th - 16th, 2009.

[2] **Md. Mijanur Rahman**, Takeuchi Tatsuki, Ryutaro Tateishi and Josaphat Tetuko Sri Sumantyo, Application of Remote Sensing for land cover analysis of southern part in Bangladesh, *International workshop on Synthetic Aperture Radar (IWSAR 2009)*, Chiba, Japan, February 16th, 2009.

[3] **Md. Mijanur Rahman**, B. Erdenee and Ryutaro Tateishi, Extraction of Mangrove forest in Bangladesh using Landsat data, *In Proceedings of the 14th CEReS International Symposium and SKYNET Workshop on "Remote Sensing of the Atmosphere for better Understanding of Climate change"*, Chiba, Japan, pp**.**111-114, November 13th - 14th , 2008.

[4] B. Erdenee, **Md. Mijanur Rahman**, C.Sujatahamma and Ryutaro Tateishi, Crop area classification using satellite data; Case study: Selenge region, Mongolia, *In Proceedings of the 14th CEReS International Symposium and SKYNET Workshop on "Remote Sensing of the Atmosphere for better Understanding of climate change"*, Chiba, Japan, pp.177-180**,** November 13th -14th , 2008.

Domestic conference presentations

[1] **Md. Mijanur Rahman**, Md. Rahmat Ullah, Mi Lan, J.T. Sri Sumantyo, and Hiroaki Kuze, Urban land use and land cover change analysis of Chittagong city in Bangladesh using multi sensor satellite data, *In Proceeding of the 17th Remote Sensing Forum, The Society of Instrument and Control Engineers (SICE)*, Tokyo, IEEE GRS **10PG0001**, pp. 33-36, March 1st , 2010.

[2] **Md. Mijanur Rahman**, B. Erdenee, Takeuchi Tatsuki and Ryutaro Tateishi, Comparison of classification methods for Mangrove forest mapping in Bangladesh, *In Proceeding of the 16th SICE Remote Sensing Forum, The Society of Instrument and Control Engineers (SICE),* Tokyo, IEEE GRS **09PG0001**, pp. 39-42, March 2nd, 2009.

[3] B. Erdenee, **Md. Mijanur Rahman** and Ryutaro Tateishi, Mapping and monitoring particular cropland use changes in the Northern part of Mongolia, *In Proceeding of the 16th SICE Remote Sensing Forum, The Society of Instrument and Control Engineers (SICE).* Tokyo, IEEE GRS **09PG0001**, pp. 43-45, March 2nd, 2009.